**School of Physics and Astronomy**
**The Raymond and Beverly Sackler**
**Faculty of Exact Sciences**
**Tel Aviv University**

# Eigenstates of Maxwell's equations and their applications

## Dissertation submitted for the degree Doctor of Philosophy

by

Asaf Farhi

This work has been carried out
under the supervision of

Prof. David J. Bergman
and
Prof. Yacov Kantor

Submitted to the Tel Aviv University Senate

School of Physics and Astronomy,
Tel Aviv University

February 2018

## Acknowledgement

First, I would like to thank my supervisor Prof. David Bergman for mentoring me during the PhD period. Prof. Bergman introduced me into the field of scattering eigenstates of Maxwell's equations, which has led us to explore interesting physical phenomena, both fundamental and related to applications. Prof. Bergman was very didactic and guided me closely in my first steps in the field. Together with that, he allowed me considerable freedom in the research and at work. This made my PhD experience very pleasant and I am very thankful to him for that. In addition, we have had many interesting discussions where he shared his mathematical and physical intuitions with me, from which I have learned a lot. These discussions also included stories of Prof. Bergman about his academic career and early life, which were particularly interesting as his family background is entwined with the history of the state of Israel. In working with him, I discovered new and very high standards of writing and presenting results, which really contributed to me. Prof. Bergman also encouraged me to go to conferences in Israel and abroad that made my PhD experience more interesting and versatile.

Second, I would like to thank PIs at the condensed matter department who helped me along the way. Dr. Haim Suchowski was always there to help me when needed. Prof. Yacov Kantor was very helpful for advice.

I would also like to acknowledge Dr. Yonatan Sivan and Dr. Parry Chen for applying some of my PhD results in their research and continuing the development. This made the research accessible to a wider audience and useful for investigating light-matter interactions in more systems.

Finally, I would like to thank the staff at the School of Physics for their responsiveness in interacting with me and the dedication in their work. More specifically, I would like to thank Yakira, Galia, Lily, Etti, and Gila.

# Abstract

Eigenstates of Maxwell's equations are fields which can exist in a medium spontaneously. Such eigenstates can be defined for a homogeneous medium and for a two-constituent medium, where a physical parameter that enables their existence is the eigenvalue. Their importance is two-fold: when their eigenvalues are approached with a physical parameter there is a strong response of the system and they can be used to expand the field generated as a response to an applied field. They can be used both in classical physics and in quantum physics, where the sources and the interactions are treated quantum mechanically.

It was suggested long ago to expand the electric field of a two-constituent setup as a response to an external field using eigenpermittivity eigenstates. The goals of the PhD were to introduce external sources such as charges and currents into the eigenpermittivity formalism and to exploit properties of the eigenstates to investigate physical phenomena such as imaging and Purcell effect.

During the PhD, the electric field of a source in a setup of a slab in a host medium was expanded using the eigenpermittivity eigenstates in the quasistatic and electrodynamic regimes. This setup was used to investigate Veselago lens imaging in which a flat lens with a refractive index with the opposite sign of this of the medium is used for imaging, resulting in enhanced resolution. It was shown that the optimal imaging location is at the interface between the slab and the host medium. In addition, the eigenpermittivity formalism was generalized to treat volume current sources. Then, the quasistatic field of a point charge in a setup of a sphere in a host medium was expanded using the sphere eigenstates. This setup was used to analyze phenomena such as enhancement of spontaneous emission of a molecule in proximity to an antenna, near-field imaging, and field behavior inside a conductor. It was shown that the field of a point source can be greatly enhanced throughout the whole nano conducting sphere for realistic physical permittivities even though it is in the quasistatic regime. Finally, the spherical analog of a phased array was introduced by observing properties of homogeneous medium eigenstates. Such a spherical layer of sources can be used to generate a focal spot eight times smaller compared to the one generated by a conventional lens and a combination of such sources can generate isotropic radiation.

# Contents

# 1 Introduction

Eigenstates of Maxwell's equations are electromagnetic fields which can exist in the system without a source. For a homogeneous medium, the eigenstates can be expressed in cartesian, cylindrical, and spherical coordinates as plane waves, vector cylindrical harmonics, and vector spherical harmonics, respectively [1]. When the medium has more than one constituent, eigenstates can exist for a given eigenvalue which is usually a permittivity value of one of the constituents [2, 3, 4] or a frequency [5]. Such eigenvalues usually necessitate gain and complex frequencies, respectively, to support the existence of the eigenstate. These eigenstates are also used in quantum mechanics calculations, where the field is treated classically and the sources are treated quantum mechanically.

Calculating an electric field in a two-constituent setup is fundamental and can be used to analyze many physical phenomena. These include nanoparticle resonance, which can be used in biomedical imaging and nano devices, enhancement of Raman scattering [6, 7], Purcell effect [8], near field imaging [9], van der Waals interactions, Forester resonance [10], and nonlinear optics.

The electric field of a plane wave impinging on an inclusion can be calculated by multiple scattering using Fresnel's equations [1]. While this is simple for planar geometries, it is rather complicated for other geometries and when localized sources generate the field, which is usually complex. Another possibility to calculate the electric field in such a medium is to calculate Green's function or Green's tensor for the setup [11]. However, this can involve lengthy analytic calculations, especially in electrodynamics. Alternatively, the electric field can be written as a sum of solutions of homogeneous and inhomogeneous Maxwell's equations, where the first can be expanded using the homogeneous-medium eigenstates in each constituent. Then, boundary conditions are imposed and a solution can be obtained [12, 13]. This calculation can be simple in some cases but when varying the source location, boundary conditions need to be reimposed and the expansion coefficients are redetermined.

Two-constituent eigenstates can be used to expand the electric field of such a medium with an external field. The physical field is comprised of the external field in a homogeneous medium and the scattered field resulting from the existence of the scatterer, which can be expanded using the two-constituent eigenstates. The poles of this expansion are the eigenvalues and when the physical parameters approach them there is a large contribution of the associated eigenmode, which can correspond to field enhancement. This expansion circumvents multiple scattering calculations and is especially advantageous for nonplanar geometries [2, 3, 4, 14].

Two-constituent eigenstates have been defined using eigenpermittivities of one of the constituents by considering a monochromatic external field [2, 3, 4]. Such permittivity eigenvalues are real in statics and have gain in electrodynamics since field is radiated. The physical meaning of such eigenvalues are permittivity values, which when approached with the physical permittivity, result in field enhancement. Later on, eigenstates have been defined by using eigenfrequencies in electrodynamics, which usually have an imaginary part. Under this defini-

tion, the constituent materials are fixed and the expression for the electric field depends on the frequency [5]. In this case, the electric field is enhanced when the external field frequency is close to an eigenfrequency.

While from the physics point of view each of the approaches to expand the field in the basis of the eigenstates scan a different physical parameter and can lead to better understanding from its perspective, the calculations differ considerably. In the eigenfrequency formalism several implementation and calculation issues arise. First, in order to calculate the eigenfunction equations a nonlinear eigenvalue equation needs to be solved. Second, the eigenstates diverge at infinity and require ad-hoc normalization procedures. Third, the electric field is calculated only inside the inclusion and for a source inside the inclusion volume [5, 15].

In the eigenpermittivity formalism on the contrary, a linear differential eigenvalue equation needs to be solved. In addition, the eigenstates do not diverge at infinity and they are normalized over the inclusion volume, which can greatly facilitate calculations. Moreover, the electric field is calculated everywhere in the system. Fourth, the formalism can be applied both in statics and electrodynamics and treats simple geometries such as a sphere, slab, and cylinder analytically [2, 3, 4, 16, 17, 18, 19].

The goal of the PhD projects is two-fold: to introduce localized sources into the eigenpermittivity formalism and to investigate physical phenomena using homogeneous medium and two-constituent medium eigenfunctions. The eigenpermittivity formalism is an appealing alternative to the successful eigenfrequency formalism due to its aforementioned advantages. The generalization of the formalism to treat localized and volume sources developed during the PhD holds promise also to treat complex phenomena associated with volume currents and polarization analytically. Throughout the projects we also investigated physical phenomena such as imaging, electric field enhancement inside nanoconductors in the quasistatic (QS) regime, enhancement of spontaneous emission of a molecule by an antenna, and effects of very small permittivity values [20]. Imaging was analyzed in several contexts: high-resolution imaging using a Veselago lens [21, 22], near-field imaging [9], and focusing of far-field light into a small focal spot [23], which can be used as the illumination source in imaging. In addition, the eigenstate formalism enabled us to gain insights in selective light-matter interaction associated with both permittivity values and external field distributions [16, 17, 24, 18]. Finally, we generalized the eigenpermittivity formalism to sources, which can be located anywhere in the system, i.e., inside any of the constituents [25].

The PhD projects included the analysis of setups of an inclusion in a host medium and a source both in the quasiststic and electrodynamic regimes. In addition, it has been shown that oscillating currents can generate homogeneous medium eigenstates in spherical coordinates. In the first project, we expanded the quasistatic electric field of a point charge in a setup of a slab in a host medium using the slab eigenfunctions. We used this setup to analyze Veselago lens imaging in the QS regime [26, 16]. The second project was a generalization of the Veselago lens analysis to the electrodynamic regime with an oscillating

dipole source. In this project volume current sources were introduced to the eigenpermittivity formalism [17]. In the third project the spherical analog of a planar phased array was presented, with implications in imaging and light-matter interaction [24]. In the fourth project we expanded the quasistatic field of a point charge in proximity to a spherical inclusion and the eigenpermittivity formalism was generalized to treat a charge distribution [18].

In the first PhD project, we considered a setup of an $\epsilon_1$ slab in an $\epsilon_2$ host medium and a point charge source. The electric potential of a point charge in such a setup had been expanded in the structure eigenstates in Ref. [26]. That work also considered the $\epsilon_1 = -\epsilon_2$ limit, which corresponds to the condition for a Veselago lens in the QS regime. The goals of the first PhD project were to calculate the electric field for realistic physical permittivity values that have a positive imaginary part and are close to the $\epsilon_1 = -\epsilon_2$ condition and to analyze Veselago lens imaging in the QS regime [16]. We calculated the electric field for permittivity values according to a PMMA-silver-photoresist setup [27] and a point charge. The host medium permittivity in our analysis was the average of the PMMA and photoresist permittivities, which are close, and the slab permittivity was of silver. The thickness of the slab was 35nm and the permittivity values were for a vacuum wavelength of 365nm [27]. We varied the point charge location between $3/8$ to $8/7$ of the slab thickness away from the slab interface, so that the typical lengths will be much smaller than the wavelength and the QS regime will be valid [16]. We revealed that the optimal imaging of a point charge is at the interface between the slab and the medium both in terms of resolution and intensity. The resolution was enhanced for these permittivity values and varied between 63nm and 72nm for a charge distanced $3/8$ and $3/4$ of the slab thickness from the slab surface, respectively. We also provided guidelines for achieving enhanced resolution and showed that gain of one of the constituents can compensate for the loss of the other and result in enhanced resolution [16].

In the second PhD project, we considered the same setup of a slab in a host medium in the full electrodynamic analysis and an oscillating dipole source. We calculated the eigenfunctions, which satisfy Maxwell's equations without a source. Then, in order to expand the electric field we had to calculate the volume integral of products of the eigenstates and the external field over the inclusion volume. This calculation is very complex due to the oscillating dipole field distribution. Therefore, a procedure to circumvent this calculation was developed. In this procedure the external field is expressed in terms of Green's tensor, the order of integration is interchanged, and Green's tensor operating on an eigenstate is replaced by an eigenvalue multiplying the eigenstate, according to the definition of the eigenvalue equation. We thus obtained a volume integral of the scalar product of the current distribution and the eigenstates, which can also be performed for volume current sources [17]. In addition, we showed that for a dipole situated close to the slab the optimal image is formed at the interface between the slab and the medium [17] in agreement with the QS analysis [16].

In the third PhD project the spherical analog of a phased array was introduced. A planar phased array consists of antennas modulated according to a plane wave variation in that plane and generate the same plane wave according

to the refraction index of the medium. A plane wave is a homogeneous-medium eigenstate in cartesian coordinates. In analogy it has been suggested, that oscillating currents occupying a spherical layer volume and modulated according to a vector spherical harmonic (VSH), which is a homogeneous medium eigenstate in spherical coordinates, will generate the corresponding VSH in all space [24]. This was derived analytically for all TE and TM vector spherical harmonics [24]. Interestingly, a generated TM $l = 1$ VSH field is concentrated at the origin with a full width at half maximum of $\sim 0.5\lambda$, which occupies a volume eight times smaller than the one generated by conventional lenses. Similarly, a current distribution occupying a spherical volume at the origin modulated by a VSH distribution also generates the corresponding VSH field in all space. A spherical layer can couple to a multipole source since the oscillation of the electrons in the layer due to the multipole field generates the same multipole field in all space, which can drive the multipole source currents. A sphere or a spherical layer couples to another concentric sphere or spherical layer since polarizing them according to a VSH distribution will result in the generation of the corresponding VSH field in space, which in turn will polarize the other sphere or spherical layer according to the same VSH distribution etc. [24].

In the fourth PhD project the quasistatic field of a point charge in proximity to a sphere was expanded using the sphere eigenstates. Such a setup has relevance for enhancing spontaneous emission of a molecule by an antenna, near-field imaging, sensing, and Raman spectroscopy. In this project the treatment of a charge density was introduced into the eigenpermittivity formalism. The electric field was shown to be significantly enhanced inside a sphere with a realistic metal in the QS regime close to a resonance. One could expect that the electric field produced by the surface charges would totally screen the applied field, similarly to the situation in statics. However, the inclusion permittivity value had the same order of magnitude as that of the host medium (but with a different sign) and the electric field could penetrate into the inclusion volume since the normal electric displacement field is continuous at the interface. This is not the case at low frequencies since $\mathrm{Im}\,(\epsilon) = \frac{\sigma}{\omega}$ and $\mathrm{Im}\,(\epsilon)$ becomes very large and as a result the electric field is screened. Moreover, the permittivity values were very close to a resonance, which resulted in a large field enhancement. Such permittivity values can enhance fields from distant objects, whose near field components usually do not reach the detector that can be defined as the sphere surface in our setup. In addition, it was shown that when the permittivity ratio is below or above all the eigenvalues, the modes interfere constructively and generate a strong signal at an angular direction equal to that of the source. When the permittivity ratio is between two eigenvalues, the modes interfere constructively at the reflected direction with respect to the spherical surface. To allow three dimensional near field imaging of a point source, a procedure to retrieve the point charge location based on the spectral content of the electric field was developed [18].

The procedure to treat current sources analytically in a two-constituent medium developed during the PhD has been applied in two projects by a group at Ben Gurion University. Their first project is an implementation for a cylin-

der inclusion in a host medium and a current source [28]. Their second project is a COMSOL implementation for a current source in a setup with a general inclusion geometry [15]. This project is of particular importance for better understanding design principles of nanostructures and is an appealing alternative to the existing tools. The set of articles [2, 3, 4, 17, 18, 15] represents the developments in the eigenpermittivity formalism throughout the years.

The articles are arranged as follows. First, we append the article on the analysis of a Veselago Lens in the quasistatic regime. Second, we proceed with the article on the analysis of a Veselago lens in the electrodynamic regime, which includes a procedure to treat current sources. Third, we present the article on generating a VSH field by oscillating currents. Fourth, we present the article on the eigenstate expansion of the quasistatic electric field of a point charge in a spherical inclusion structure. We then discuss the future directions for generalizing the formalism and applying it to analyze interesting physical phenomena.

PHYSICAL REVIEW A **90**, 013806 (2014)

# Analysis of a Veselago lens in the quasistatic regime

Asaf Farhi* and David J. Bergman†

*Raymond and Beverly Sackler School of Physics and Astronomy, Faculty of Exact Sciences, Tel Aviv University, IL-6997801, Tel Aviv, Israel*

(Received 26 April 2014; published 8 July 2014)

The resolution of conventional optical lenses is limited by the wavelength. Materials with a negative refractive index have been shown to enable the generation of an enhanced resolution image where both propagating and nonpropagating waves are employed. We analyze such a Veselago lens by exploiting some exact one-dimensional integral expressions for the quasistatic electric potential of a point charge in that system. These were recently obtained by expanding that potential in the quasistatic eigenfunctions of a three-flat-slabs composite structure. Numerical evaluations of those integrals, using realistic values for physical parameters like the electric permittivities of the constituent slabs and their thickness, reveal some surprising effects: For example, the maximum concentration of the electric field occurs not at the geometric optics foci but at the interfaces between the negative permittivity slab and the positive permittivity slabs. The analysis provides simple computational guides for designing such structures to achieve enhanced resolution of an optical image.

DOI: 10.1103/PhysRevA.90.013806 PACS number(s): 42.79.−e, 78.20.Bh, 42.70.−a

## I. INTRODUCTION

The resolution limit in conventional optical imaging is known to be inversely proportional to the wavelength of the light. In 1967, a theoretical analysis by Veselago, based upon geometric optics, suggested that a flat slab with a negative refractive index can focus at a point the radiation from a point source [1]. At that time, materials possessing a negative refractive index did not exist, but recent developments in metamaterials have made the production of such materials possible [2–4]. In 2000, another important analysis by Pendry showed that materials with a negative refractive index can amplify evanescent waves, and thus enable the generation of an image by both propagating and nonpropagating waves, theoretically leading to unlimited resolution [5].

In the quasistatic regime, when the typical length scales are much smaller than the wavelength, Maxwell's equations reduce to static equations in which the electric and the magnetic fields are decoupled. Hence, the optical constant of relevance in this regime is the electric permittivity rather than the refractive index. The imaging of an electric point charge was recently analyzed by expanding the local electric potential in a series of the quasistatic eigenfunctions of a three-flat-slabs composite structure. This analysis yielded exact one-dimensional integral expressions for the quasistatic electric potential of a point charge in that system [6,7].

In this paper we first derive exact expressions for the electric field in a two-constituent three-flat-slabs composite structure in the form of one-dimensional integrals. These are obtained from the classical Maxwell equations in a continuous medium. The electromagnetic properties of that medium are characterized by a position and frequency-dependent but **k**-vector-independent electric permittivity. We further assume that this permittivity has a constant value in each constituent and changes discontinuously at any interface.

We then perform numerical computations for such a setup using realistic values for the physical parameters like the electric permittivities and the thickness of the intermediate slab. In these computations we vary both the location of the point charge and the constituent permittivities of the medium. These computations reveal surprising results among which is that the best imaging is obtained at the interfaces between the intermediate slab and the surrounding medium rather than at the geometric optics foci.

The structure of the paper is as follows. In Sec. II we present a summary of the basic theory for the analysis of such a setup. In Sec. III we derive exact expressions for the local electric field and validate our results. In Sec. IV we present results of the numerical computations for various charge locations and for various permittivity values. In Sec. V we discuss our results.

## II. SUMMARY OF THE BASIC THEORY

In this section we describe the derivation of the exact results for the local electric potential field $\psi(\mathbf{r})$ in the quasistatic limit for the case of a point electric charge $q$ in a two-constituent composite medium [6,7]. In these references a two-constituent composite structure, composed of three infinitely wide parallel slabs, is considered. The intermediate slab, with an electric permittivity $\epsilon_1$, is placed between two slabs with an electric permittivity $\epsilon_2$ (see Fig. 1).

In the static limit Maxwell's equations reduce to Poisson's equation for $\psi(\mathbf{r})$:

$$-4\pi\rho(\mathbf{r}) = \nabla\cdot(\epsilon_1\theta_1 + \epsilon_2\theta_2)\nabla\psi, \tag{1}$$

which can be rewritten as

$$\nabla^2\psi = -4\pi\rho(\mathbf{r})/\epsilon_2 + u\nabla\cdot(\theta_1\nabla\psi), \tag{2}$$

$$\theta_1(\mathbf{r}) \equiv 1-\theta_2(\mathbf{r}) = \begin{Bmatrix} 1 & \text{if} & \epsilon(\mathbf{r})=\epsilon_1, \\ 0 & \text{if} & \epsilon(\mathbf{r})=\epsilon_2, \end{Bmatrix}, \quad u \equiv 1-\frac{\epsilon_1}{\epsilon_2},$$

where $\theta_1$ and $\theta_2 \equiv 1-\theta_1$ are step functions that characterize the microstructure of the composite medium. The function $\rho(\mathbf{r})$ which appears in these equations represents a charge density distribution, including the possibility that $\rho(\mathbf{r}) = q\delta^3(\mathbf{r}-\mathbf{r}_0)$, i.e., a point charge at $\mathbf{r}_0$. The capacitor plates at $z=-L_2$ and $z=L_2'$ are included in order that the appropriate boundary

*asaffarhi@post.tau.ac.il
†bergman@post.tau.ac.il

 

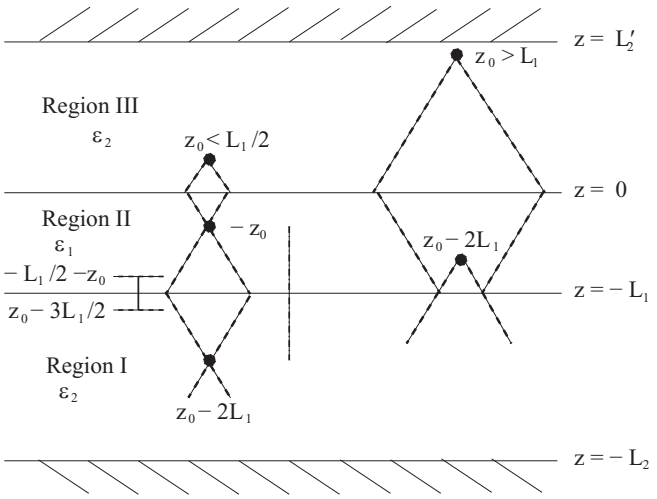


FIG. 1. A three-parallel-slabs microstructure that fills the entire volume of a large parallel-plate capacitor. The upper layer (Region III), where $\epsilon = \epsilon_2$, includes a point charge $q$ located at $\mathbf{r}_0 = (0,0,z_0)$. In the left part $z_0 < L_1/2$ while in the right part $z_0 > L_1$, where $L_1$ is the thickness of the intermediate $\epsilon_1$ layer (Region II). Even when all the other linear sizes of this structure tend to $\infty$, this configuration is still unsolvable in any simple fashion. The diagonal dashed lines show how a geometric optics or light rays description would lead to a focusing of the original point charge in Region III at new points in Regions I and II when $\epsilon_2 = -\epsilon_1$. The vertical dot-dashed line indicates the regions where $\psi(\mathbf{r})$ then diverges in the case shown on the left side, while the vertical solid line shows where the dissipation rate diverges (after Ref. [6]).

conditions may be imposed there so as to result in a unique solution for $\psi(\mathbf{r})$. At the end of the calculation we will take the limits $L_2 \to \infty$ and $L_2' \to \infty$.

We reformulate Eq. (2) as an integrodifferential equation for $\psi(\mathbf{r})$ [8]

$$\begin{aligned} \psi(\mathbf{r}) &= \psi_0(\mathbf{r}) + u\hat{\Gamma}\psi, \\ \hat{\Gamma}\psi &\equiv \int dV' \theta_1(\mathbf{r}') \nabla' G_0(\mathbf{r},\mathbf{r}') \cdot \nabla' \psi(\mathbf{r}'), \end{aligned} \tag{3}$$

where $G_0(\mathbf{r},\mathbf{r}')$ is Green's function for Laplace's equation with zero boundary conditions defined as follows:

$$\begin{aligned} \nabla^2 G_0(\mathbf{r},\mathbf{r}') &= -\delta^3(\mathbf{r}-\mathbf{r}'), \\ G_0(\mathbf{r},\mathbf{r}') &= 0 \quad \text{for} \quad z = -L_2 \quad \text{and} \quad z = L_2', \end{aligned}$$

and $\psi_0(\mathbf{r})$ is the solution of Poisson's equation in a uniform medium with a permittivity $\epsilon_2$.

In the case of no charges and vanishing boundary conditions, Eq. (3) reduces to

$$s\psi(\mathbf{r}) = \hat{\Gamma}\psi, \quad s \equiv \frac{1}{u}.$$

Defining the scalar product of two scalar functions $\psi(\mathbf{r}), \phi(\mathbf{r})$ by

$$\langle \psi | \phi \rangle \equiv \int d^3 r \theta_1 \nabla \psi^* \cdot \nabla \phi$$

makes $\hat{\Gamma}$ a Hermitian operator [8]. Therefore it has a complete set of eigenfunctions $\phi_n$ and eigenvalues $s_n$

$$s_n \phi_n(\mathbf{r}) = \hat{\Gamma}\phi_n.$$

By using the expansion of the unity operator $\hat{I}$ in Eq. (3), we can expand the potential in a series of the eigenfunctions $\phi_n$

$$\begin{aligned} \hat{I} &= \sum_n |\phi_n\rangle\langle\phi_n| \\ \Longrightarrow \psi(\mathbf{r}) &= \psi_0(\mathbf{r}) + \sum_n \frac{s_n}{s - s_n} \langle\phi_n|\psi_0\rangle \phi_n(\mathbf{r}). \end{aligned} \tag{4}$$

We now set the charge distribution to be that of a point charge located at $\mathbf{r}_0 = (0,0,z_0)$. This means that

$$\psi_0(\mathbf{r}) = \frac{q/\epsilon_2}{|\mathbf{r} - \mathbf{r}_0|}. \tag{5}$$

The eigenfunctions that satisfy Laplace's equation with vanishing boundary conditions are

$$\begin{aligned} &\phi_{\mathbf{k}}^{\pm}(\mathbf{r}) \\ &= e^{i\mathbf{k}\cdot\rho} \cdot \begin{cases} A_{\mathbf{k}}^{\pm} \sinh[k(z + L_2)], & z \in \text{I}, \\ B_{\mathbf{k}}^{\pm} \sinh(kz) + B_{\mathbf{k}}'^{\pm} \sinh[k(z + L_1)], & z \in \text{II}, \\ C_{\mathbf{k}}^{\pm} \sinh[k(z - L_2')], & z \in \text{III}. \end{cases} \end{aligned} \tag{6}$$

One might think that these eigenfunctions cease to be valid when $|\mathbf{k}|L_1$, $|\mathbf{k}|L_2$, $|\mathbf{k}|L_2'$ are not very small. That is not so: In fact, it is only necessary that Maxwell's equations for the local physical field $\mathbf{E}(\mathbf{r})$ be reducible, approximately, to Poisson's equation for the local electric potential field $\psi(\mathbf{r})$ [Eq. (1)]. The subsequent calculation of the eigenstates of the homogeneous version of that equation is a purely mathematical exercise and the resulting expansion of Eq. (4) for that approximate quasistatic physical potential field is exact. By imposing continuity of the potential and the perpendicular component of $\mathbf{D}$, we get the eigenvalues and the coefficients in these expressions

$$\begin{aligned} s_{\mathbf{k}}^{\pm} &= \frac{1 \mp e^{-kL_1}}{2}, \quad A_{\mathbf{k}}^{\pm} = -B_{\mathbf{k}}^{\pm} \frac{\sinh(kL_1)}{\sinh[k(L_2 - L_1)]}, \\ B_{\mathbf{k}}'^{\pm} &= \mp B_{\mathbf{k}}^{\pm}, \quad C_{\mathbf{k}}^{\pm} = \pm B_{\mathbf{k}}^{\pm} \frac{\sinh(kL_1)}{\sinh(kL_2')}. \end{aligned}$$

Note that in the above expression for $s_{\mathbf{k}}^{\pm}$ we already took the limits $L_2', L_2 \to \infty$. The normalization condition $\langle\phi_{\mathbf{k}}^{\pm}|\phi_{\mathbf{k}}^{\pm}\rangle = 1$ leads to

$$1 = 2kL_x L_y |B_{\mathbf{k}}^{\pm}|^2 \sinh(kL_1)[\cosh(kL_1) \mp 1].$$

The eigenvalues have a single accumulation point at $s = 1/2$ which is therefore a very singular point of Eq. (4). That equation leads to the following expressions for the electric potential in the three regions in the form of one-dimensional integrals [6]

$$\begin{aligned} \psi &= \frac{4s(1-s)q}{\epsilon_2} \int_0^{\infty} dk\, J_0(k\rho) \frac{e^{-k(z_0 - z)}}{e^{-2kL_1} - (2s-1)^2} \\ &= 4q\epsilon_1 \int_0^{\infty} dk\, J_0(k\rho) \frac{e^{-k(z_0 - z)}}{(\epsilon_2 - \epsilon_1)^2 e^{-2kL_1} - (\epsilon_2 + \epsilon_1)^2} \text{ in I}, \end{aligned} \tag{7}$$

$$\psi = \frac{2sq}{\epsilon_2}\int_0^\infty dk\, J_0(k\rho)\, e^{-k(z_0-z)}\frac{e^{-2k(z+L_1)}-2s+1}{e^{-2kL_1}-(2s-1)^2}$$
$$= 2q\int_0^\infty dk\, J_0(k\rho)\, e^{-k(z_0-z)} \times \frac{(\epsilon_2-\epsilon_1)e^{-2k(z+L_1)}-(\epsilon_2+\epsilon_1)}{(\epsilon_2-\epsilon_1)^2e^{-2kL_1}-(\epsilon_2+\epsilon_1)^2} \text{ in II,} \quad (8)$$

$$\psi = \psi_0 + \frac{q(2s-1)/\epsilon_2}{\sqrt{\rho^2+(z+z_0)^2}} - \frac{4s(1-s)(2s-1)q}{\epsilon_2} \times \int_0^\infty dk\, J_0(k\rho)\,\frac{e^{-k(z_0+z)}}{e^{-2kL_1}-(2s-1)^2}$$
$$= \frac{q/\epsilon_2}{\sqrt{\rho^2+(z-z_0)^2}} + \frac{\epsilon_2+\epsilon_1}{\epsilon_2-\epsilon_1}\frac{q/\epsilon_2}{\sqrt{\rho^2+(z+z_0)^2}} + 4q\epsilon_1\frac{\epsilon_2+\epsilon_1}{\epsilon_2-\epsilon_1} \times \int_0^\infty dk\, J_0(k\rho)\,\frac{e^{-k(z_0+z)}}{(\epsilon_2-\epsilon_1)^2e^{-2kL_1}-(\epsilon_2+\epsilon_1)^2} \text{ in III.} \quad (9)$$

These expressions for the potential, as well as the local dissipation rate, defined by $\mathrm{Im}(\epsilon)\,|\mathbf{E}|^2/8\pi$, were analyzed for the case of $s = 1/2$ (i.e., $\epsilon_1 = -\epsilon_2$) [6]. This analysis showed that the potential diverges in the range of positions $z_0 - 2L_1 < z < -z_0$. Moreover, when the location of the point charge satisfies $z_0 < L_1/2$, the local dissipation rate diverges for $z$ in the range $[z_0 - 3L_1/2, -z_0 - L_1/2]$ (see Fig. 1).

When $s = 1/2$ these expressions for the potential take the following exact closed forms in those regions of $z$ where it is nondiverging

$$\psi(\mathbf{r}) = \begin{cases} \frac{q/\epsilon_2}{\sqrt{\rho^2+(z-z_0+2L_1)^2}}, & \mathbf{r}\in \text{I}, \\ \frac{q/\epsilon_2}{\sqrt{\rho^2+(z+z_0)^2}}, & \mathbf{r}\in \text{II}, \\ \frac{q/\epsilon_2}{\sqrt{\rho^2+(z-z_0)^2}}, & \mathbf{r}\in \text{III}. \end{cases}$$

This means that the potential above the top geometric optics image at $\mathbf{r} = (0,0,-z_0)$ and below the bottom geometric optics image at $\mathbf{r} = (0,0,z_0 - 2L_1)$, is that of a point charge located at these points. In the intermediate $z$ values between these expected images, the potential diverges (see Fig. 1). Since there are no point charges located at these points, the surface integration over the electric field perpendicular to an arbitrary envelope surrounding one of these points gives zero according to Gauss' law. This is fulfilled since the contribution to the surface integral from where the potential diverges cancels out with the contribution from where the potential is finite (for a spherical surface centered around one of these points, the first and second contributions give $-q/2$ and $q/2$, respectively).

## III. EXACT EXPRESSIONS FOR THE ELECTRIC FIELD AND VERIFICATION OF THE RESULTS

We calculated exact expressions for the electric fields by differentiating the expressions for the potentials derived in Ref. [6] and reproduced in Eqs. (7) to (9) with respect to $\rho$ and $z$. The expressions for the $z$ and $\rho$ components of $\mathbf{E}$ are as follows, where we substituted $s \equiv 1/2 + \Delta s$:

### Region I

$$E_{\mathrm{I}\rho} = C_1\int_0^\infty dk k J_1(k\rho)\frac{e^{-k(z_0-z)}}{e^{-2kL_1}-4(\Delta s)^2}, \quad (10)$$

$$E_{\mathrm{I}z} = -C_1\int_0^\infty dk k J_0(k\rho)\frac{e^{-k(z_0-z)}}{e^{-2kL_1}-4(\Delta s)^2}, \quad (11)$$

where

$$C_1 \equiv \frac{q[1-4(\Delta s)^2]}{\epsilon_2}.$$

### Region II

$$E_{\mathrm{II}\rho} = C_2\int_0^\infty dk k J_1(k\rho)e^{k(z-z_0)}\frac{e^{-2k(z+L_1)}-2\Delta s}{e^{-2kL_1}-4(\Delta s)^2}, \quad (12)$$

$$E_{\mathrm{II}z} = C_2\int_0^\infty dk k J_0(k\rho)e^{k(z-z_0)}\frac{e^{-2k(z+L_1)}+2\Delta s}{e^{-2kL_1}-4(\Delta s)^2}, \quad (13)$$

where

$$C_2 \equiv \frac{(1+2\Delta s)\,q}{\epsilon_2}.$$

### Region III

$$E_{\mathrm{III}\rho} = \frac{q}{\epsilon_2}\frac{\rho}{[\rho^2+(z-z_0)^2]^{3/2}} + \frac{2q\Delta s}{\epsilon_2}\frac{\rho}{[\rho^2+(z+z_0)^2]^{3/2}} - 2C_1\Delta s\int_0^\infty dk k J_1(k\rho)\frac{e^{-k(z_0+z)}}{e^{-2kL_1}-4(\Delta s)^2}, \quad (14)$$

$$E_{\mathrm{III}z} = \frac{q}{\epsilon_2}\frac{(z-z_0)}{[\rho^2+(z-z_0)^2]^{3/2}} + \frac{2q\Delta s}{\epsilon_2}\frac{(z+z_0)}{[\rho^2+(z+z_0)^2]^{3/2}} - 2C_1\Delta s\int_0^\infty dk k J_0(k\rho)\frac{e^{-k(z_0+z)}}{e^{-2kL_1}-4(\Delta s)^2}. \quad (15)$$

To verify the expressions for the potential and the electric field we checked the continuity of the potential and the perpendicular component of $\mathbf{D}$ at the interfaces. This was done by substituting $z = -L_1$ in the expressions for Regions I and II and $z = 0$ in the expressions for Regions II and III, yielding the same expressions in both cases (see the Appendix for more details).

## IV. NUMERICAL COMPUTATIONS

We computed the one-dimensional integrals in the expressions for the potential and the electric field using MATLAB. We verified the computations of these integrals by checking the continuity of the potential and the perpendicular component of $\mathbf{D}$ at the interfaces for a set of $\rho$ values (numerical values were compared). In addition, we calculated the field intensity $I(\mathbf{r})$ as well as the dissipation rate $W(\mathbf{r})$ in the three regions

using the following definitions:

$$I(\mathbf{r}) \equiv |E_\rho(\mathbf{r})|^2 + |E_z(\mathbf{r})|^2, \tag{16}$$

$$W(\mathbf{r}) \equiv \mathrm{Im}[\epsilon(\mathbf{r})](|E_\rho(\mathbf{r})|^2 + |E_z(\mathbf{r})|^2). \tag{17}$$

These are in fact the expressions for the intensity and the dissipation in which $c/8\pi$ and $\omega/8\pi$ were not included, respectively, for simplicity.

We then placed another charge horizontally shifted from the original charge to find the charge separation that is needed for resolution of the images. We varied that separation until the field intensity at the midpoint between the two images was $1/e^{1/2}$ of the intensity at the images. We defined this distance as the separation distance needed to resolve the two images. To estimate the resolution in each horizontal layer we normalized the local intensity in Region I by dividing it by the intensity at the horizontal coordinates of the images in that layer (see Figs. 4, 7, 10, 13, 16).

Throughout the computations we used $q = e$, where $e$ is the electron charge. We present the results for $\psi$, $I$, and $W$ without specifying units. Thus, in order for those results to be in units of statV, erg/(s cm$^2$), and erg/(s cm$^3$), one has to multiply them by $q/e$, $q^2c/8\pi e^2$, and $q^2\omega/8\pi e^2$, respectively.

### A. Polymethyl methacrylate-silver-photoresist setup for different vertical charge locations

We modeled a polymethyl methacrylate (PMMA)-silver-photoresist setup that is similar to the one used by the authors of Ref. [9] by a two constituents setup in which the two external slabs have the average permittivity value of PMMA and the photoresist, and the permittivity of the intermediate slab is that of metallic silver. We used the values for the permittivities suitable for a free-space wavelength of 365 nm [9]

$$\epsilon_{\mathrm{silver}} = -2.55 + 0.24i,$$
$$\epsilon_{\mathrm{PMMA}} = 2.25 + 0.12i,$$
$$\epsilon_{\mathrm{PR}} = 2.886 + 0.059i,$$

which lead in the two constituents setup to the following permittivity values:

$$\epsilon_1 = -2.55 + 0.24i, \quad \epsilon_2 = 2.57 + 0.0896i.$$

The silver slab thickness was set to $L_1 = 35$ nm as in Ref. [9] and the external slabs in the calculation are assumed to have infinite thickness. We performed the computations for several locations of the point charge object on the vertical axis. The first location was $z_0 = 40\,\mathrm{nm} = 8L_1/7$ which agrees with the setup in Ref. [9]. We then placed the charge closer to the top interface at $z = 3L_1/4$ and $z = 3L_1/8$.

#### 1. *Charge located at* $z_0 = 40\,\mathrm{nm} = 8L_1/7$

We first placed the charge at $z_0 = 40\,\mathrm{nm} = 8L_1/7$ as in Ref. [9]. In Fig. 2 we present the real and imaginary parts of the potential in all the regions. The potential is of course time dependent according to

$$\mathrm{Re}(\psi e^{i\omega t}) = \mathrm{Re}(\psi)\cos(\omega t) - \mathrm{Im}(\psi)\sin(\omega t).$$

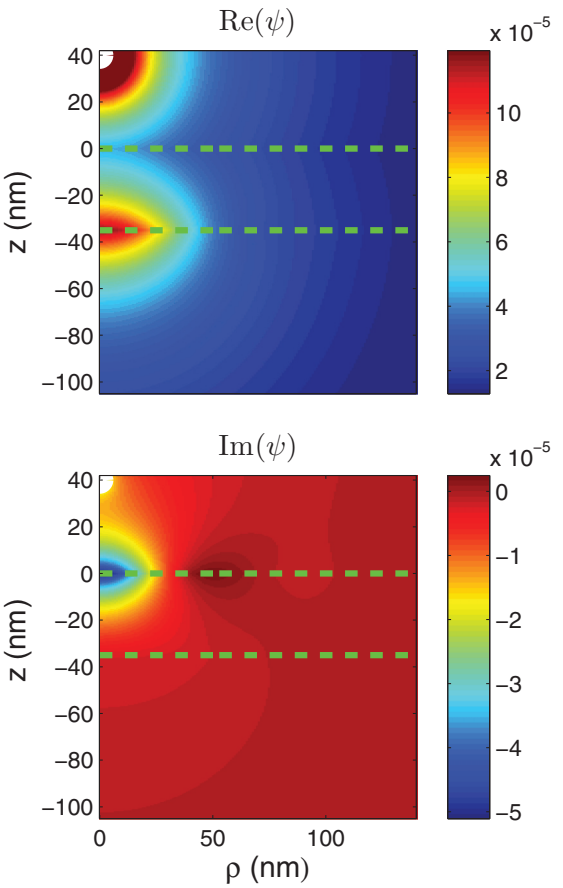


FIG. 2. (Color online) Real and imaginary parts of the potential for a charge located at $z_0 = 40\,\mathrm{nm} = 8L_1/7$.

The white circle denotes the object and, where applicable in the subsequent figures, the image expected according to geometrical optics. It can be seen that Re($\psi$) has high values at the $z = -L_1$ interface and that Im($\psi$) has high (absolute) values at the $z = 0$ interface. In this figure, as well as in subsequent figures that display all the regions, we used a linear color scale. To present an informative figure we mapped all the values higher than a certain value to this value. Thus, in all the locations which exhibit the highest value, the actual values are often much higher than the apparent value. In Fig. 3 we present the intensity and the dissipation in all the regions. It can be seen that the intensity is high at the interfaces and has a higher value at the bottom interface. The dissipation in Region II is higher than in Region I due to the fact that the imaginary part of the permittivity is higher in Region II. Note that the amplification of the electric field and the intensity starts even before the top interface. This adds to the picture described by the author of Ref. [5], where the amplification of the evanescent waves only in the silver slab was discussed.

In Fig. 4 we show the intensity and the horizontally normalized intensity in Region I for two horizontally displaced charges. It can be seen that the maximal resolution is at the interface $z = -L_1$. The distance between the charges that enables the images to be resolved as previously explained is 82.4 nm, which is in good agreement with the results found in Ref. [9] [see Fig. 4(d) there].

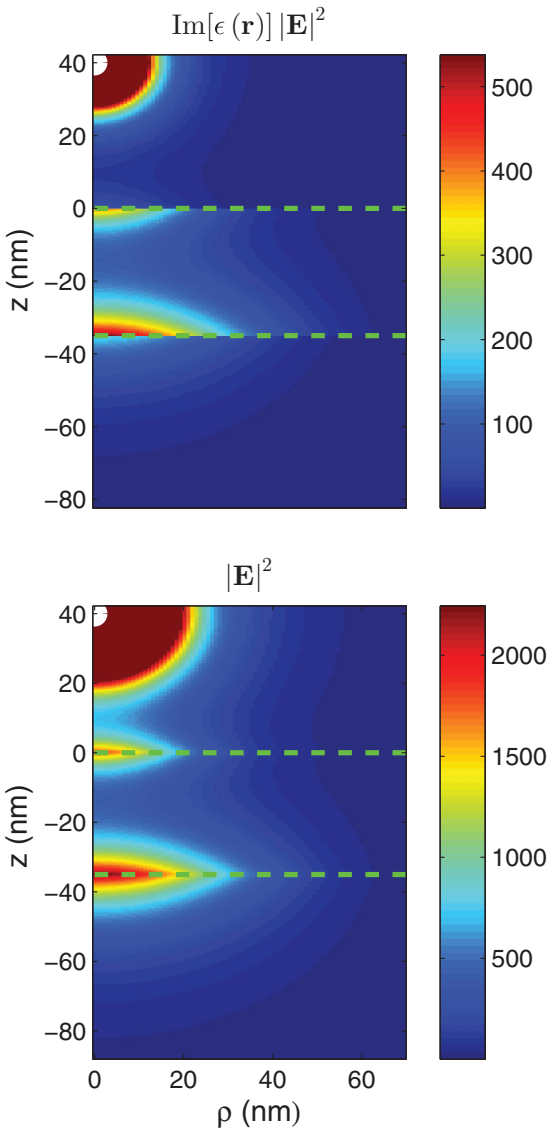


FIG. 3. (Color online) Intensity and dissipation for a charge located at $z_0 = 40\,\text{nm} = 8L_1/7$.

#### 2. *Charge located at* $z_0 = 26.25\,\text{nm} = 3L_1/4$

In Fig. 5 we present the real and imaginary parts of the potential in all regions for a charge located at $z_0 = 26.25\,\text{nm} = 3L_1/4$. Here also $\text{Re}(\psi)$ and $\text{Im}(\psi)$ (in absolute value) peak at the bottom and top interface, respectively.

In Fig. 6 we present the intensity and the dissipation in all regions. Here we originally expected that the intensity would have high values at the geometric optics foci $z = -3L_1/4$ and at $z = z_0 - 2L_1$. However, the intensity is actually concentrated at the $z = 0$ and $z = -L_1$ interfaces. In this case the peak intensity is higher at the top interface. The intensity in Region I is almost one order of magnitude higher than in the previous case.

In Fig. 7 the intensity and the horizontally normalized field intensity in Region I for two horizontally displaced charges are presented. The white circles denote the focal points. The separation exhibited is the smallest for which the images are still resolved as previously defined. Surprisingly,

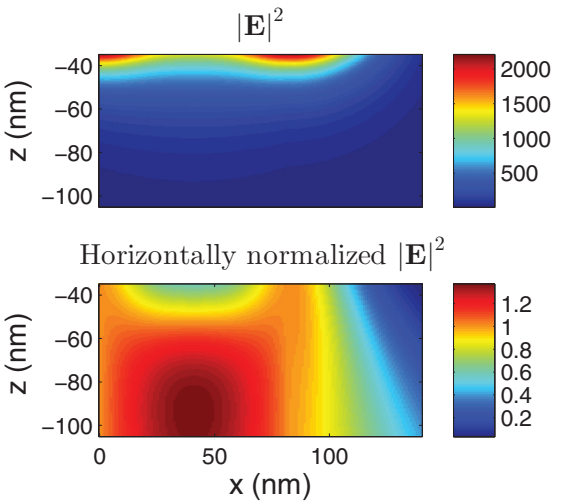


FIG. 4. (Color online) Intensity and horizontally normalized intensity in Region I for two charges located at $z_0 = 40\,\text{nm} = 8L_1/7$, $x_1 = 0$, $x_2 = 82.4$ nm.

the separation of the images is best not at the expected focal plane but at the interface. Thus, both in terms of intensity and resolution the image formed at the interface $z = -L_1$ is optimal. In addition it can be seen that the separation distance in this case is 72 nm, which is better than the previous one.

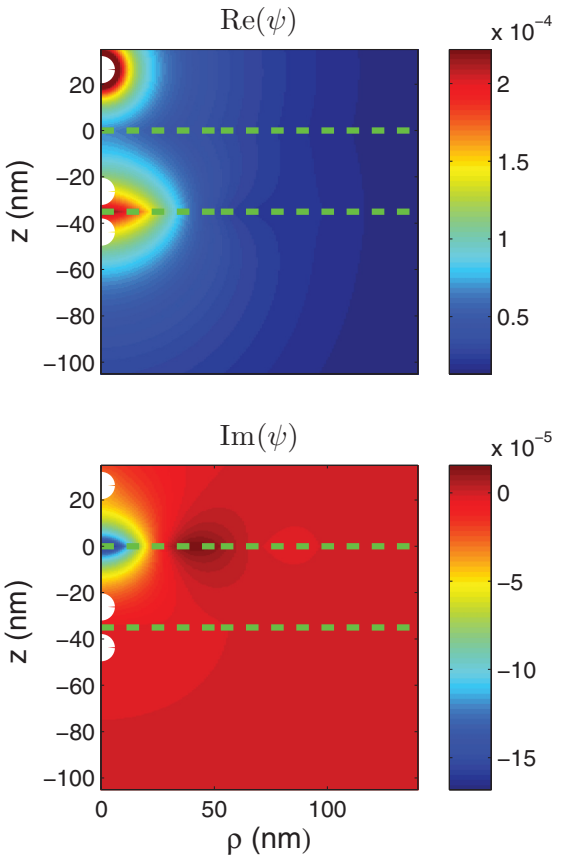


FIG. 5. (Color online) Real and imaginary parts of the potential for a charge located at $z_0 = 26.25\,\text{nm} = 3L_1/4$.

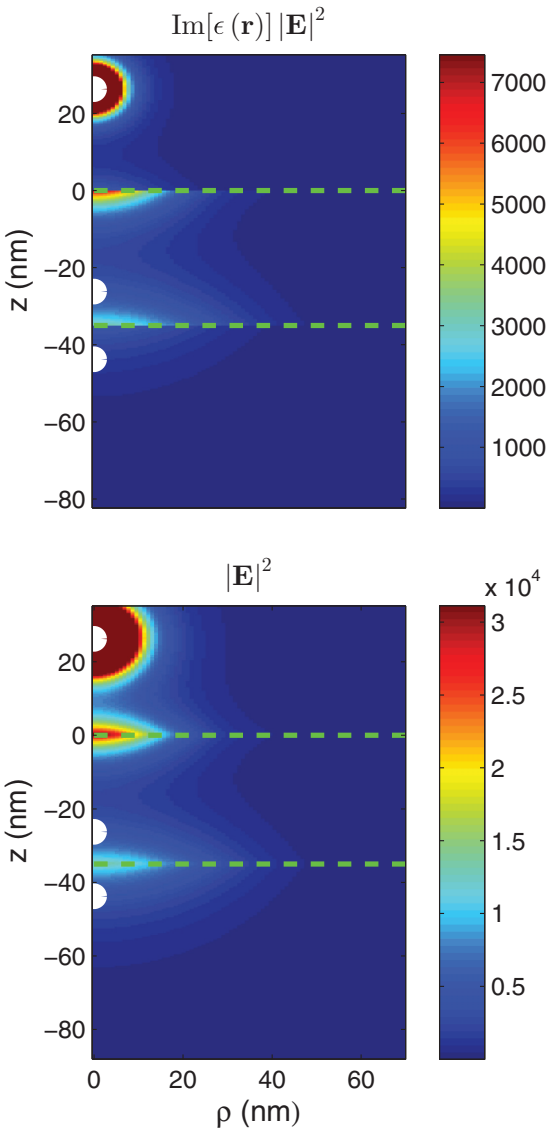


FIG. 6. (Color online) Intensity and dissipation for a charge located at $z_0 = 26.25\,\text{nm} = 3L_1/4$.

### 3. *Charge located at $z_0 = 13.125\,\text{nm} = 3L_1/8$*

Here we calculate the potential, intensity and dissipation for a setup with a charge located at $z_0 = 3L_1/8$. In this case if $s$ were equal to half the dissipation rate should have diverged in the range $z_0 - 3L_1/2 < z < -z_0 - L_1/2$. However, since $s \neq 1/2$ we expect that the dissipation rate will increase in that range compared to the previous case where $z_0 = 3L_1/4$.

In Fig. 8 we present the real and imaginary parts of the potential for a charge located at $z_0 = 13.125\,\text{nm} = 3L_1/8$. Here again $\text{Re}(\psi)$ and $\text{Im}(\psi)$ peak at the bottom and top interfaces, respectively.

In Fig. 9 we present the intensity and dissipation in the three regions. Here also the intensity is maximal at the interfaces rather than at the geometric optics foci. It can be clearly seen that the intensity is higher at the top interface. The intensity and the dissipation at the bottom interface in this case are almost one order of magnitude higher than in the previous case.

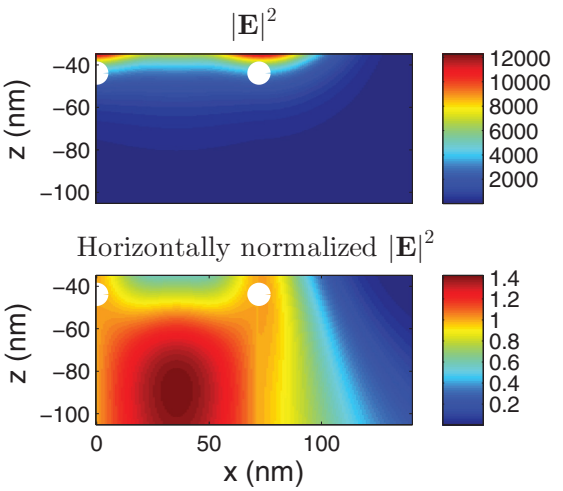


FIG. 7. (Color online) Intensity and horizontally normalized intensity in Region I for two charges located at $z_0 = 26.25\,\text{nm} = 3L_1/4$, $x_1 = 0, x_2 = 72$ nm.

In Fig. 10 we present the intensity and the horizontally normalized intensity in Region I for two horizontally separated charges. It can be seen that the separation distance in this case is 63.2 nm which is better than in the previous cases.

It can be concluded that for the three object locations, the best images are formed at the interfaces. As we moved the

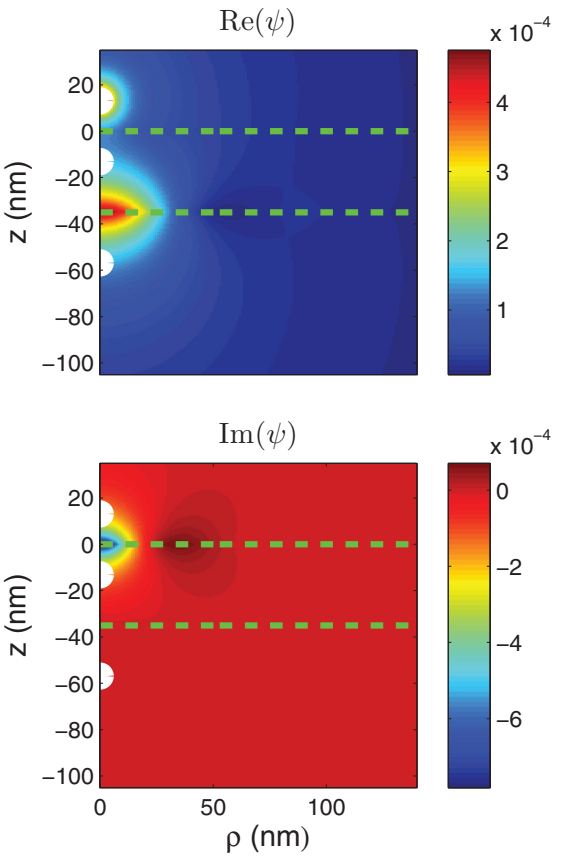


FIG. 8. (Color online) Real and imaginary parts of the potential for a charge located at $z_0 = 13.125\,\text{nm} = 3L_1/8$.

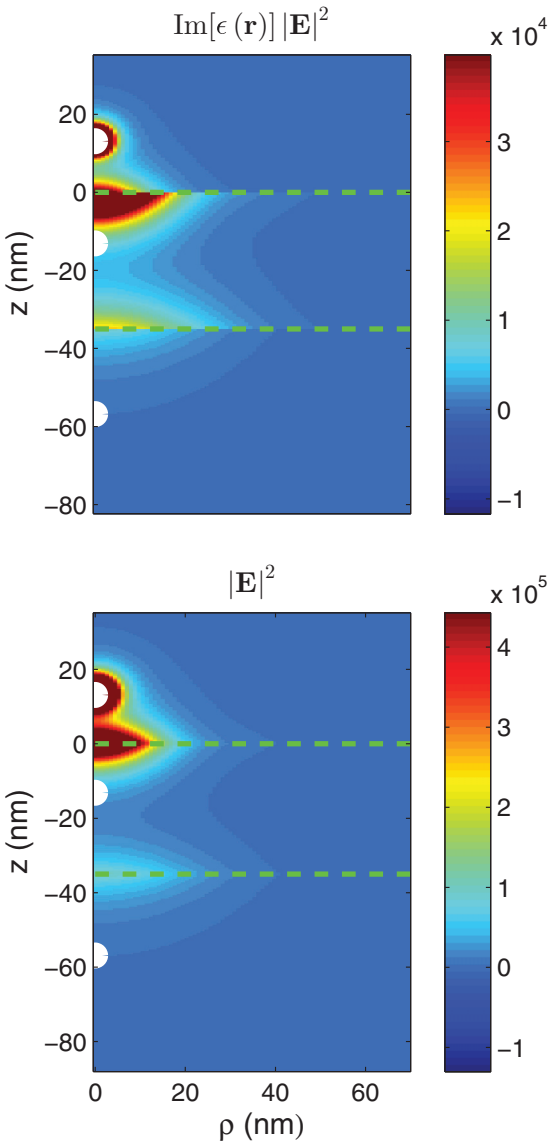


FIG. 9. (Color online) Intensity and dissipation for a charge located at $z_0 = 13.125\,\text{nm} = 3L_1/8$.

point charge closer to the $z = 0$ interface, the image formed at the $z = -L_1$ interface became better in terms of both intensity and resolution.

### B. Computations for other permittivities

We repeated our computations for other values of $s$ for a charge located at $z = 3L_1/4$. First, we performed computations with a setup in which the real part of $\Delta s$ remained the same as in Sec. IV A and the imaginary part was divided by 100. Then, we performed a computation in which both the real and imaginary parts of $\Delta s$ were divided by 100.

#### *1.* $\Delta s$ *with* $\text{Im}\,(\Delta s)$ *divided by* 100

In Fig. 11 $\text{Re}(\psi)$ and $\text{Im}(\psi)$ are presented. It can be seen that the potential now has an alternating sign as argued by the authors of Ref. [7]. In Fig. 12 the intensity and the dissipation are presented. The intensity at both interfaces is higher than in

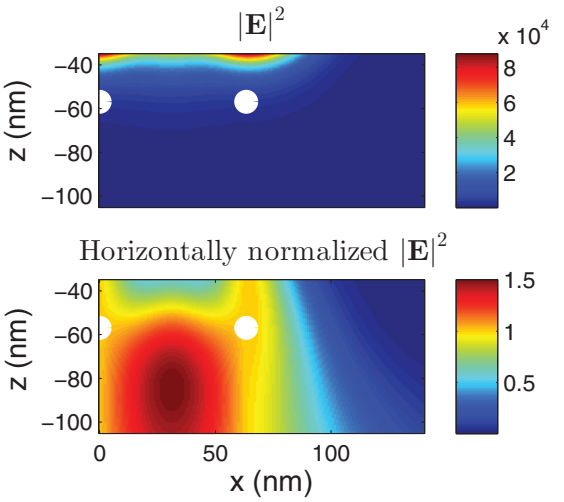


FIG. 10. (Color online) Intensity and horizontally normalized intensity in Region I for two charges located at $z_0 = 13.125\,\text{nm} = 3L_1/8$, $x_1 = 0$,$x_2 = 63.2$ nm.

the PMMA-silver-photoresist setup. In addition the intensity here is higher at the bottom interface as opposed to the previous setup with $z_0 = 3L_1/4$, where it was higher at the top interface. The same is true regarding the local dissipation rates, despite the fact that $\text{Im}(\Delta s)$ is smaller (which can be satisfied when

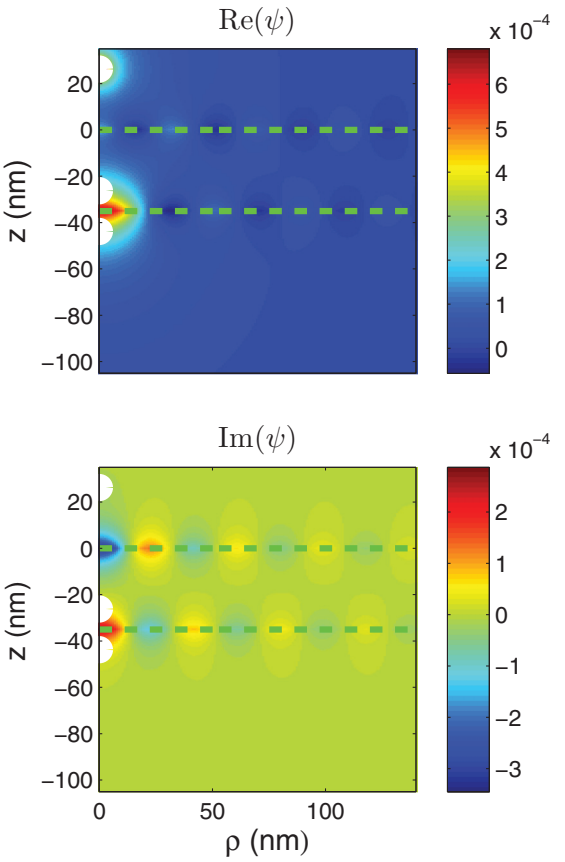


FIG. 11. (Color online) Real and imaginary part of the potential $z_0 = 3L_1/4$, $\Delta s = 0.0014 + 0.00032i$.

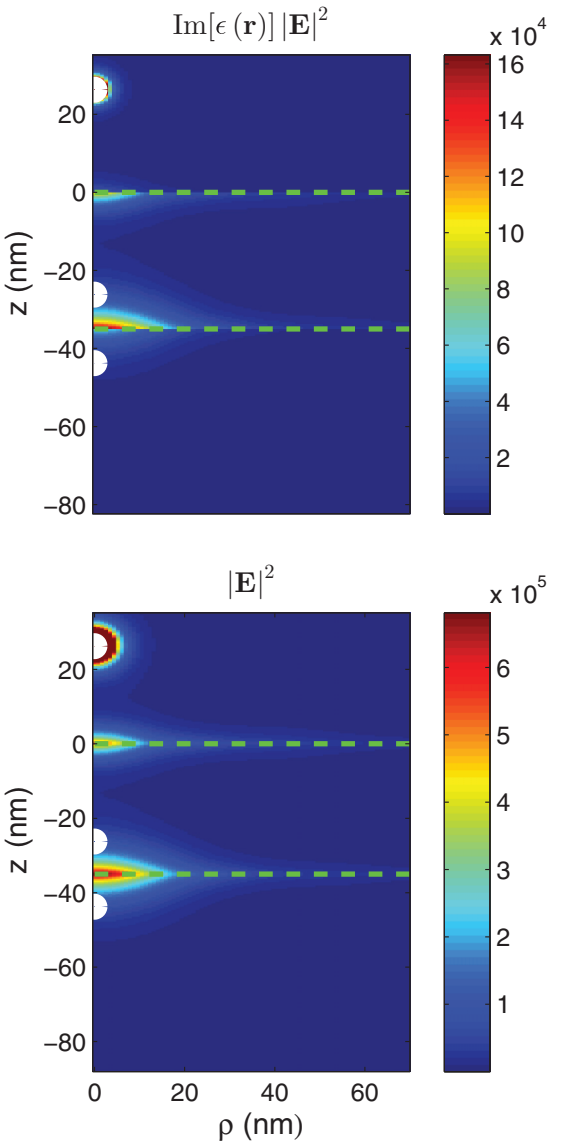


FIG. 12. (Color online) Intensity and dissipation for $z_0 = 3L_1/4$, $\Delta s = 0.0014 + 0.00032i$.

the imaginary part of the permittivity is small everywhere in the system). This is due to the fact that $\psi$ and $\mathbf{E}$ tend to $\infty$ as $\Delta s \to 0$ only at the lower interface.

In Fig. 13 the intensity and the horizontally normalized intensity for two charges in Region I are presented. In this case the minimum separation distance between two objects for resolution of the images is 44.8 nm, which is significantly better than when $\mathrm{Im}(\Delta s)$ was not decreased by a factor of 100.

#### 2. $\Delta s$ *with both* $\mathbf{Re}\,(\Delta s)$ *and* $\mathbf{Im}\,(\Delta s)$ *divided by* 100

In Fig. 14 $\mathrm{Re}(\psi)$ and $\mathrm{Im}(\psi)$ are presented. They peak (in absolute value) at the bottom and top interfaces, respectively, and they have alternating signs. In Fig. 15 the intensity and dissipation for all the regions are presented. It can be seen that $I$ and $W$ at the bottom interface are higher compared to the case when we decreased just the imaginary part of $\Delta s$. In Fig. 16 the intensity and the horizontally normalized intensity in Region I for two separated charge objects are displayed.

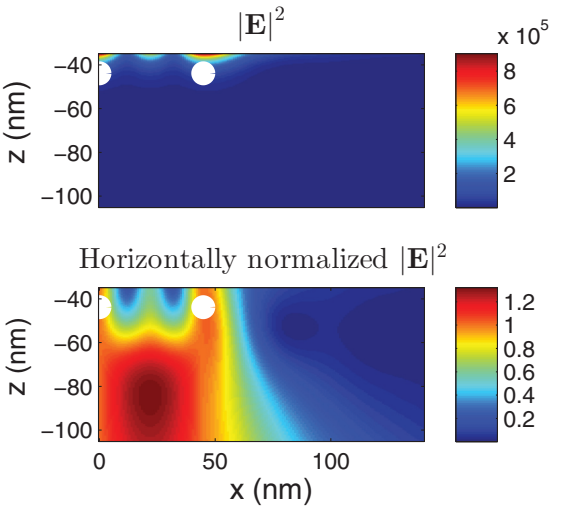


FIG. 13. (Color online) Intensity and horizontally normalized intensity for 2 charges $z_0 = 3L_1/4$, $x_1 = 0$, $x_2 = 44.8$ nm.

The minimum separation distance for this $\Delta s$ value is 32 nm. It can be seen that when we also decrease $\mathrm{Re}(\Delta s)$ we have better separation between the images.

We can conclude that when the value of $\Delta s$ is lowered, the optimal image locations are also at the interfaces. As we decrease the real and imaginary parts of $\Delta s$ both the intensity

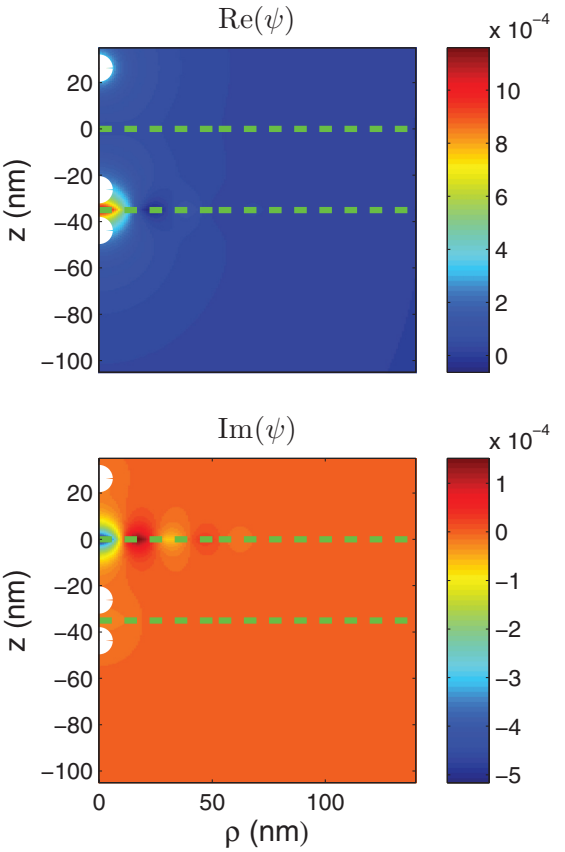


FIG. 14. (Color online) Real and imaginary part of the potential $z_0 = 3L_1/4$, $\Delta s = 0.000014 + 0.00032i$.

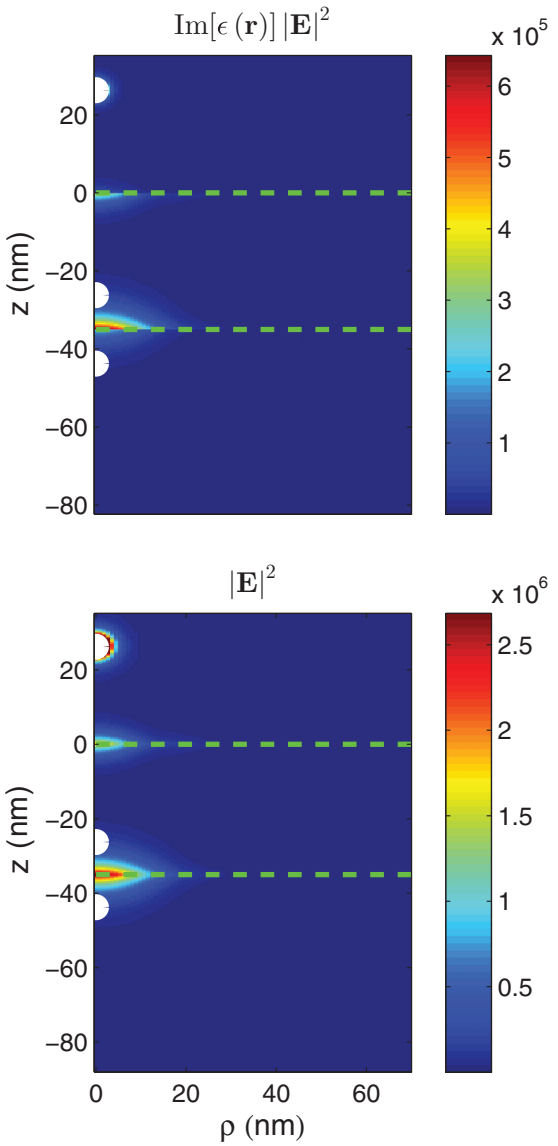


FIG. 15. (Color online) Intensity and dissipation for $z_0 = 3L_1/4$, $\Delta s = 0.000014 + 0.00032i$.

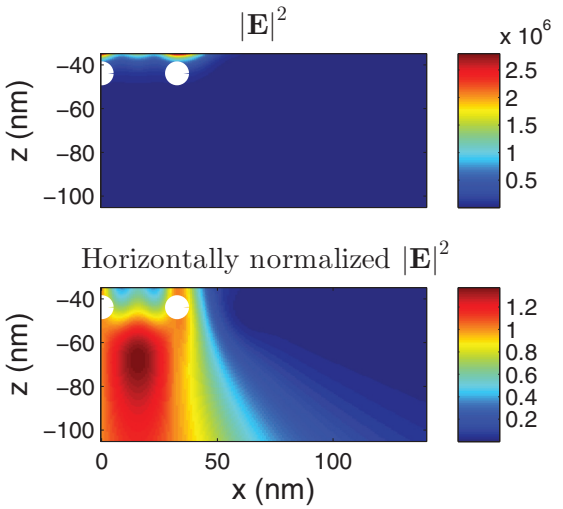


FIG. 16. (Color online) Intensity and horizontally normalized intensity in Region I for 2 charges $z_0 = 3L_1/4, x_1 = 0, x_2 = 32$ nm , $\Delta s = 0.000014 + 0.00032i$

and the resolution become better for imaging. The analysis suggests that in the quasistatic regime for a setup with a small value of $\Delta s$, very high intensity and resolution can be reached (this occurs when $\epsilon_1 \approx -\epsilon_2$). It would be interesting to investigate whether such a pair of materials exists or can be engineered.

### C. Analysis for a definite value of $k$

The expressions for the potential and the electric field can be easily decomposed into their $k$ components. Thus, in Region II, the component associated with a specific $k = |\mathbf{k}|$ is simply the integrand in Eqs. (8), (12), and (13). Using this, we can easily calculate the contribution of each $k$ component to the potential and the electric field.

It was interesting, in the case where $\Delta s \to 0$, to calculate the amplitude of the electric field for given $\rho$ and $k$ values at the top interface and compare it to the same quantity at the bottom interface. To that end we substituted $z = 0$ and $z = -L_1$ in the integrands of Eqs. (12) and (13) and took the limit $\Delta s \to 0$. This leads to the following results:

$$\frac{\lim_{\Delta s\to 0} E_{\mathrm{II}\,\rho}(z=-L_1)}{\lim_{\Delta s\to 0} E_{\mathrm{II}\,\rho}(z=0)} = \frac{C_2 k J_1(k\rho) e^{-z_0 k} e^{L_1 k}}{C_2 k J_1(k\rho) e^{-z_0 k}} = e^{L_1 k},$$

$$\frac{\lim_{\Delta s\to 0} E_{\mathrm{II}\,z}(z=-L_1)}{\lim_{\Delta s\to 0} E_{\mathrm{II}\,z}(z=0)} = \frac{C_2 k J_0(k\rho) e^{-z_0 k} e^{L_1 k}}{C_2 k J_0(k\rho) e^{-z_0 k}} = e^{L_1 k}.$$

These $k$-dependent ratios are the same as the transmission coefficient of the slab derived from the multiple scattering calculation in Ref. [5]. This is another confirmation of the validity of our results.

## V. DISCUSSION

We analyzed a two-constituents setup of three dielectric slabs, in which an electric point charge is located in the top slab. We first derived exact expressions for the local electric field in the form of one-dimensional integrals and verified our results. We then performed numerical computations of the electric potential, intensity, and dissipation for a setup that was previously tested in experiments. We calculated these quantities of interest for several charge locations and several permittivity values. Finally, we showed that our results agree with previous analytic results.

The computations reveal several important effects. The best images are formed at the interfaces between the slab and the surrounding medium rather than at the geometric optics foci. This optimality is in terms of both intensity and resolution. In addition the computations confirm previous analysis in which it was stated that the dissipation rate diverges when $\epsilon_1 = -\epsilon_2$. This can occur either when this quantity is real, in which case the constituents are free of any dissipation, or when they have imaginary parts with opposite signs. In the latter case one of the constituents exhibits dissipation while the other exhibits gain.

As was explained in that analysis, this counterintuitive effect originates from the fact that $s = 1/2$ is the accumulation point of all the eigenvalues and is therefore a very singular point of Maxwell's equations [6,7]. The computations for several charge locations show that when the object is closer to the interface with the intermediate slab, the imaging is better. The computations for several permittivity values show that as $\epsilon_1 \to -\epsilon_2$ the imaging becomes better.

## APPENDIX: VERIFICATION OF THE ANALYTIC RESULTS

Calculations of $\psi(\mathbf{r})$ and $\mathbf{D}(\mathbf{r})$ at the two interfaces lead to

$$\psi_{\mathrm{I}}(z=-L_1)=\psi_{\mathrm{II}}(z=-L_1)=\frac{4qs(1-s)}{\epsilon_2}\int e^{k(-L_1-z_0)}\left[\frac{1}{e^{-2kL_1}-(1-2s)^2}\right]J_0(k\rho)dk, \tag{A1}$$

$$\psi_{\mathrm{II}}(z=0)=\psi_{\mathrm{III}}(z=0)=\frac{q(2\Delta s+1)}{\epsilon_2}\int_0^\infty dk\,J_0(k\rho)e^{-k(z_0)}\frac{e^{-2kL_1}-2(\Delta s)}{e^{-2kL_1}-4(\Delta s)^2}, \tag{A2}$$

$$\epsilon_1 E_{\mathrm{II}_z}(z=-L_1)=\epsilon_2 E_{\mathrm{I}_z}(z=-L_1)=\epsilon_1\frac{4q\left(\frac{1}{2}+\Delta s\right)^2}{\epsilon_2}\int_0^\infty dk k J_0(k\rho)e^{k(-L_1-z_0)}\frac{1}{e^{-2kL_1}-4(\Delta s)^2}, \tag{A3}$$

$$\epsilon_1 E_{\mathrm{II}_z}(z=0)=\epsilon_2 E_{\mathrm{III}_z}(z=0)=\epsilon_1\frac{(1+2\Delta s)q}{\epsilon_2}\int_0^\infty dk k J_0(k\rho)e^{-kz_0}\frac{e^{-2kL_1}+2\Delta s}{e^{-2kL_1}-4(\Delta s)^2}, \tag{A4}$$

where we used $\frac{\epsilon_1}{\epsilon_2-\epsilon_1}=\frac{\epsilon_1}{\epsilon_2}(\frac{1}{2}+\Delta s)=-(\frac{1}{2}-\Delta s)$ from the definition of $s$.


[1] V. Veselago, Usp. Fiz. Nauk **92**, 517 (1967) [Phys. Usp. **10**, 509 (1968)].

[2] D. F. Sievenpiper, M. E. Sickmiller, and E. Yablonovitch, Phys. Rev. Lett. **76**, 2480 (1996).

[3] J. B. Pendry, A. J. Holden, W. J. Stewart, and I. Youngs, Phys. Rev. Lett. **76**, 4773 (1996).

[4] J. B. Pendry, A. J. Holden, D. Robbins, and W. Stewart, IEEE Trans. Microwave Theory Tech. **47**, 2075 (1999).

[5] J. B. Pendry, Phys. Rev. Lett. **85**, 3966 (2000).

[6] D. J. Bergman, Phys. Rev. A **89**, 015801 (2014).

[7] D. J. Bergman and J. Ben Yakar, in *Proceedings of the SPIE Conference entitled "Plasmonics: Metallic Nanostructures and their Optical Properties XI"*, edited by M. I. Stockman, in the SPIE Meeting on Optics and Photonics, The San Diego Convention Center, San Diego, CA, August 2013 (SPIE, Bellingham, WA, 2013), p. 8809.

[8] D. J. Bergman, in *Les Méthodes de l'Homogénéisation: Théorie et Applications en Physiques*, edited by R. Dautray (Librairie Eyrolles, Paris, 1985), pp. 1–128.

[9] C. S. N. Fang, H. Lee, Cheng Sun, and X. Zhang, Science **308**, 534 (2005).

PHYSICAL REVIEW A **93**, 063844 (2016)

# Electromagnetic eigenstates and the field of an oscillating point electric dipole in a flat-slab composite structure

Asaf Farhi* and David J. Bergman†

*Raymond and Beverly Sackler School of Physics and Astronomy, Faculty of Exact Sciences, Tel Aviv University, IL-69978 Tel Aviv, Israel*

(Received 10 March 2016; published 27 June 2016)

An exact calculation of the local electric field $\mathbf{E}(\mathbf{r})$ is described for the case of a time-dependent point electric dipole $\mathbf{p}e^{-i\omega t}$ in the top layer of an $\epsilon_2$, $\epsilon_1$, $\epsilon_2$ three parallel slabs composite structure, where the $\epsilon_1$ layer has a finite thickness $2d$ but the $\epsilon_2$ layers are infinitely thick. For this purpose we first calculate all the eigenstates of the full Maxwell equations for the case where $\mu = 1$ everywhere in the system. The eigenvalues appear as special, nonphysical values of $\epsilon_1$ when $\epsilon_2$ is given. These eigenstates are then used to develop an exact expansion for the physical values of $\mathbf{E}(\mathbf{r})$ in the system characterized by physical values of $\epsilon_1(\omega)$ and $\epsilon_2(\omega)$. Results are compared with those of a previous calculation of the local field of a time-dependent point charge in the quasistatic regime. Numerical results are shown for the local electric field in practically important configurations where attaining an optical image with subwavelength resolution has practical significance.

DOI: 10.1103/PhysRevA.93.063844

## I. INTRODUCTION

In order to have a physical electromagnetic (EM) field in some system volume it is usually necessary to have either a field incident from outside of the system volume or a nonvanishing charge density and current density inside the system. However, when the material in the system has certain special values of its material parameters, a field can arise in the system spontaneously. Such a state is an EM eigenstate and the special parameters are the appropriate eigenvalues. While such eigenstates can never be realized in a passive physical system, because the necessary values of its material parameters are unachievable in a real material, these states are often useful in particular circumstances. Thus a real material can have parameters that approach some of the eigenvalues, in which case the EM response of such a material can become anomalously strong. Furthermore, the EM field of a real physical system can be expanded in a series of the eigenstates, leading to an alternative approach to the calculation of that field and its consequences. Such an approach was used in the past to describe the scattering of EM radiation by a collection of spheres [1]. Such an approach was also applied, in the past, to calculate the macroscopic response of a collection of spheres in the quasistatic regime, i.e., the macroscopic electric permittivity $\epsilon_e$ of such a material [2,3]. More recently, such an approach was used to compute the local electric field in a special structure, known as the Veselago Lens [4], where it had been claimed that an EM image was achievable with unrestricted resolution [5]. By exploiting an expansion of the local electric field in the exact quasistatic eigenstates for the case of a point charge, a much more detailed analysis of this system became possible [6,7]. In previous discussions the asymptotic expression for the potential at the interface between the lens and the medium when $\epsilon_1 = -\epsilon_2$, both real, was shown to diverge [8–10]. In Refs. [6,7] an exact expression for the potential (in all space) in the form of a one-dimensional (1D) integral was derived for general complex permittivity values and it was shown that the imaging, in terms of both intensity and resolution, is optimal at the interface. In recent works a 2D setup of a coated cylinder with an external line source was analyzed using the full Maxwell equations and the asymptotic expression for the electric field at the interface when $\epsilon_1 = -\epsilon_2$, both real, was shown to diverge [10,11]. In this article we attempt to extend the approach of Refs. [6,7] to expand the electric field (in all space) in the exact eigenstates of the full Maxwell equations for complex permittivity values and a general 3D current distribution. This will be used to extend the discussion of a Veselago Lens to the nonquasistatic regime. The formalism enables to calculate the electric field also for current sources in a simple manner, avoiding the complex calculation of the scattering of the electric field of these sources.

The general theory for this is developed in Sec. II. In Sec. III the eigenstates are calculated in closed form for the special structure of a flat slab, which is also the structure of the Veselago Lens. In Sec. IV these eigenstates are used to expand the local EM field produced in such a lens by an oscillating point electric dipole source directed parallel and perpendicular to the slab. Section V includes a summary of our main results and a discussion of possible future extensions of the approach developed here.

We note that our entire discussion assumes that all the interfaces are mathematically smooth and that the electric permitivity is local and jumps discontinuously at these interfaces. These are obviously idealizations. A less idealized picture of those interfaces would require a different type of theoretical approach which is beyond the scope of this article.

## II. THEORY OF THE EIGENSTATES OF MAXWELL'S EQUATIONS IN A TWO-CONSTITUENT COMPOSITE MEDIUM WHERE $\mu = 1$

We assume that all physical quantities are monochromatic functions of time, namely that they are proportional to $e^{-i\omega t}$. We confine ourselves to the case where $\mu = 1$ everywhere, but the position dependent electric permittivity $\epsilon(\mathbf{r})$ has two different values corresponding to a two-constituent composite

*asaffarhi@post.tau.ac.il
†bergman@post.tau.ac.il

 

medium:

$$\epsilon(\mathbf{r}) = \epsilon_1\theta_1(\mathbf{r}) + \epsilon_2\theta_2(\mathbf{r}), \tag{2.1}$$

where $\theta_i(\mathbf{r})$, $i = 1,2$ is a step function equal to 1 when $\mathbf{r}$ is inside the $\epsilon_i$ constituent and equal to zero elsewhere. Note that $\epsilon_i$ is usually complex and includes any electrical conductivity that the constituents may have. Assuming that all the EM fields are monochromatic and a general current distribution, Maxwell's equations become, in Gaussian units,

$$\begin{aligned} \nabla\cdot(\epsilon\mathbf{E}) = 0, \quad \nabla\times\mathbf{E} = \frac{i\omega}{c}\mathbf{H}, \\ \nabla\cdot\mathbf{H} = 0, \quad \nabla\times\mathbf{H} = -\frac{i\omega}{c}\epsilon\mathbf{E} + \frac{4\pi}{c}\mathbf{J}. \end{aligned} \tag{2.2}$$

From these we can obtain the following equation for the local electric field $\mathbf{E}(\mathbf{r})$:

$$-\nabla\times(\nabla\times\mathbf{E}) + k_2^2\mathbf{E} = uk_2^2\theta_1\mathbf{E} - \frac{4\pi i\omega}{c^2}\mathbf{J}, \tag{2.3}$$

$$u \equiv 1 - \frac{\epsilon_1}{\epsilon_2}, \quad k_2^2 \equiv \epsilon_2\frac{\omega^2}{c^2}. \tag{2.4}$$

The last differential equation can be transformed into an integral equation by using a tensor Green function $G_{\alpha\beta}(\mathbf{r},\mathbf{r}',k_2)$, defined by

$$-\nabla\times(\nabla\times\overleftrightarrow{G}) + k_2^2\overleftrightarrow{G} = k_2^2\mathbb{1}\delta^3(\mathbf{r}-\mathbf{r}') \tag{2.5}$$

and by appropriate outgoing boundary conditions at large distances $|\mathbf{r}-\mathbf{r}'|$. Noting that $G_{\alpha\beta}(\mathbf{r},\mathbf{r}',k)$ will depend on those position vectors only through their difference $\mathbf{R} \equiv \mathbf{r}-\mathbf{r}'$, we first apply a spatial Fourier transformation to this equation. This results in a linear algebraic equation for the Fourier transform of $G_{\alpha\beta}(\mathbf{r}-\mathbf{r}',k)$ which is easily solved, leading to the following expression for that Fourier transform:

$$G_{\alpha\beta}(\mathbf{q},k) = \frac{q_\alpha q_\beta - k^2\delta_{\alpha\beta}}{q^2-k^2}. \tag{2.6}$$

The inverse Fourier transform of this, with the boundary condition of an outgoing or evanescent wave at large distances, is found by first integrating over the direction of the three-dimensional vector $\mathbf{q}$, leading to the remaining integral over the magnitude of $\mathbf{q}$ ($q \equiv |\mathbf{q}|$):

$$\begin{aligned} G_{\alpha\beta}(\mathbf{R},k) &= (k^2\delta_{\alpha\beta} + \nabla_\alpha\nabla_\beta)\frac{i}{(2\pi)^2|\mathbf{R}|}\int q\,dq\,\frac{e^{iqR}}{q^2-k^2} \\ &= -(k^2\delta_{\alpha\beta} + \nabla_\alpha\nabla_\beta)\frac{e^{ikR}}{4\pi R}. \end{aligned} \tag{2.7}$$

The last integration here was carried out by adding to the real axis of $q$ an infinite radius semicircle in the upper complex plane of $q$ and then using Cauchy's theorem to evaluate the integral over the resulting closed contour. This closed form expression for $\overleftrightarrow{G}(\mathbf{r}-\mathbf{r}',k)$ was obtained many years ago in Ref. [1].

Using $\overleftrightarrow{G}(\mathbf{r}-\mathbf{r}',k_2)$ we can now "solve" Eq. (2.3) by treating its right-hand side (RHS) as if it were known. In this way we get the following integral equation for the local electric field $\mathbf{E}(\mathbf{r})$:

$$\mathbf{E} = \mathbf{E}_0 + u\hat{\Gamma}\mathbf{E}, \tag{2.8}$$

$$\hat{\Gamma}\mathbf{E} \equiv \int dV'\theta_1(\mathbf{r}')\,\overleftrightarrow{G}(\mathbf{r}-\mathbf{r}',k_2)\cdot\mathbf{E}(\mathbf{r}'), \tag{2.9}$$

where $\mathbf{E}_0$ is the the electric field generated by the external sources $\mathbf{J}(\mathbf{r})$ in a uniform $\epsilon_2$ medium.

The scalar product of two vector fields $\mathbf{F}(\mathbf{r})$, $\mathbf{E}(\mathbf{r})$ is now defined by

$$\langle\mathbf{F}|\mathbf{E}\rangle \equiv \int dV\,\theta_1(\mathbf{r})\mathbf{F}^*(\mathbf{r})\cdot\mathbf{E}(\mathbf{r}). \tag{2.10}$$

Under this definition $\hat{\Gamma}$ is a symmetric operator, as defined in Appendix A, because $G_{\alpha\beta}(\mathbf{R},k) = G_{\beta\alpha}(-\mathbf{R},k)$, but it is non-Hermitian because $\overleftrightarrow{G}(\mathbf{r}-\mathbf{r}',k_2)$ is complex valued. Thus the left eigenstates of $\hat{\Gamma}$ , $\langle\tilde{\mathbf{E}}_n|$ are just the dual states of its right eigenstates and the left and right eigenvalues are the same:

$$\begin{aligned} \langle\tilde{\mathbf{E}}_n|\hat{\Gamma}|\mathbf{r}\rangle &\equiv \int dV'\theta_1(\mathbf{r}')\mathbf{E}_n(\mathbf{r}')\cdot\overleftrightarrow{G}(\mathbf{r}'-\mathbf{r},k) \\ &= \int dV'\theta_1(\mathbf{r}')\,\overleftrightarrow{G}(\mathbf{r}-\mathbf{r}',k)\cdot\mathbf{E}_n(\mathbf{r}') = \langle\mathbf{r}|\hat{\Gamma}|\mathbf{E}_n\rangle \\ &\Longrightarrow s_n|\mathbf{E}_n\rangle = \hat{\Gamma}|\mathbf{E}_n\rangle, \quad s_n\langle\tilde{\mathbf{E}}_n| = \langle\tilde{\mathbf{E}}_n|\hat{\Gamma}, \end{aligned} \tag{2.11}$$

where $\langle\tilde{\mathbf{E}}_n|\mathbf{r}\rangle = \langle\mathbf{r}|\tilde{\mathbf{E}}_n\rangle^* \equiv \langle\mathbf{r}|\mathbf{E}_n\rangle \equiv \mathbf{E}_n(\mathbf{r})$.

Because $\hat{\Gamma}$ is a symmetric operator it therefore has the following property for any two states $|\mathbf{E}\rangle$ and $|\mathbf{F}\rangle$:

$$\langle\tilde{\mathbf{F}}|\hat{\Gamma}|\mathbf{E}\rangle = \langle\tilde{\mathbf{E}}|\hat{\Gamma}|\mathbf{F}\rangle.$$

From this it is now easy to show that the eigenstates and their duals satisfy

$$\langle\tilde{\mathbf{E}}_n|\mathbf{E}_m\rangle = 0 \tag{2.12}$$

if $s_n \neq s_m$.

The scalar product of a left eigenstate and a right eigenstate of $\hat{\Gamma}$ can be written as follows:

$$\langle\tilde{\mathbf{F}}_n|\mathbf{E}_m\rangle = \int dV\,\theta_1(\mathbf{r})\mathbf{F}_n(\mathbf{r})\cdot\mathbf{E}_m(\mathbf{r}). \tag{2.13}$$

This differs from Eq. (2.10) because the dual eigenfunction $\langle\mathbf{r}|\tilde{\mathbf{F}}_n\rangle$ is not equal to the eigenfunction $\langle\mathbf{r}|\mathbf{F}_n\rangle$ but rather to its complex conjugate $\langle\mathbf{r}|\mathbf{F}_n\rangle^*$. Clearly, in the general case where these eigenfunctions are complex valued this scalar product is not assured to be real or positive and could vanish even when the states $|\mathbf{E}_m\rangle$ and $|\mathbf{F}_n\rangle$ are the same, because the integrand is $\theta_1(\mathbf{r})[\mathbf{E}_n(\mathbf{r})]^2$ and not $\theta_1(\mathbf{r})|\mathbf{E}_n(\mathbf{r})|^2$. Thus the question of normalizability of the eigenstates must be investigated for each of them separately. We will nevertheless assume that they are normalizable in our case and that they therefore form a complete set. Thus, from the pair of equations (2.11) we conclude that the unit operator can be expanded in terms of those states and their duals $|\tilde{\mathbf{E}}_n\rangle$ as

$$\mathbb{1} = \sum_n \frac{|\mathbf{E}_n\rangle\langle\tilde{\mathbf{E}}_n|}{\langle\tilde{\mathbf{E}}_n|\mathbf{E}_n\rangle}. \tag{2.14}$$

We can now write the following formal solution of Eq. (2.8):

$$|\mathbf{E}\rangle = \frac{1}{1-u\hat{\Gamma}}|\mathbf{E}_0\rangle = |\mathbf{E}_0\rangle + \frac{\hat{\Gamma}}{s-\hat{\Gamma}}|\mathbf{E}_0\rangle, \tag{2.15}$$

$$s \equiv \frac{1}{u} \equiv \frac{\epsilon_2}{\epsilon_2-\epsilon_1}, \tag{2.16}$$

and insert the unit operator of Eq. (2.14) to obtain

$$\langle\mathbf{r}|\mathbf{E}\rangle - \langle\mathbf{r}|\mathbf{E}_0\rangle = \sum_n \frac{s_n}{s-s_n}\langle\mathbf{r}|\mathbf{E}_n\rangle\frac{\langle\tilde{\mathbf{E}}_n|\mathbf{E}_0\rangle}{\langle\tilde{\mathbf{E}}_n|\mathbf{E}_n\rangle}, \tag{2.17}$$

where $s_n \equiv \epsilon_2/(\epsilon_2-\epsilon_{1,n})$ and $\epsilon_{1,n}$ is the eigenvalue which corresponds to $s_n$.

Since the last equation constitutes an expansion of the function $\langle\mathbf{r}|\mathbf{E}\rangle - \langle\mathbf{r}|\mathbf{E}_0\rangle$ in a basis of Hilbert space, therefore it *always converges*, even where $\theta_1(\mathbf{r})$ has a discontinuous jump and consequently $\nabla\theta_1(\mathbf{r})$ has a $\delta$-function singularity.

It is now useful to recall that the eigenstates of $\hat{\Gamma}$ fall into two classes [1].

(1) *Longitudinal eigenstates* $\mathbf{E}(\mathbf{r}) = \nabla\phi(\mathbf{r})$. For these states the eigenvalue will always be $s = 1$ and $\mathbf{E}(\mathbf{r})$ must vanish outside the $\epsilon_1$ volume. Inside that volume $\phi(\mathbf{r})$ is almost arbitrary and the differential equation (2.3) is satisfied in a trivial fashion. The only restriction on $\phi(\mathbf{r})$ is due to the fact that the tangential component of $\mathbf{E}(\mathbf{r})$ must be continuous at the $\epsilon_1, \epsilon_2$ interface. Since its tangential component must vanish there, therefore $\phi(\mathbf{r})$ must be constant over every connected piece of that interface. Obviously, the magnetic field $\mathbf{H}(\mathbf{r})$ vanishes everywhere for these states.

(2) *All the eigenstates for which* $s \neq 1$ *(these are transverse fields)*. From Eq. (2.3) it follows that $\nabla\cdot\mathbf{E} = 0$ inside both the $\epsilon_1$ and the $\epsilon_2$ regions, though not at their interface. These states must obey Eq. (2.3) in a nontrivial fashion.

Although the Class 1 eigenstates are difficult to catalog, since they have a degenerate eigenvalue, it turns out that they are not needed for expanding any physical solutions of Eq. (2.3). That is because they are orthogonal to any solution $\mathbf{E}(\mathbf{r})$ of Maxwell's equations. To see this, we denote by $\mathbf{E}_1(\mathbf{r}) \equiv \nabla\phi_1$ any longitudinal eigenstate and write

$$\langle\tilde{\mathbf{E}}_1|\mathbf{E}\rangle = \int dV\,\theta_1\mathbf{E}_1\cdot\mathbf{E} = \int_{V_1} dV[\nabla\cdot(\phi_1\mathbf{E}) - \phi_1\nabla\cdot\mathbf{E}],$$

where $V_1$ is the $\epsilon_1$ subvolume. The second term under the last integral vanishes because the field $\mathbf{E}(\mathbf{r})$ is a transverse field inside $V_1$ as long as $\epsilon_1 \neq 0$—see Eq. (2.2). (Note that in a real physical material $\epsilon_1$ can never vanish: it must always have a nonzero imaginary part which represents dissipation.) The first term can be transformed into a surface integral over the $\epsilon_1, \epsilon_2$ interface, where $\phi_1$ is a constant, denoted by $\phi_{1i}$, over every connected portion of that interface. Transforming the surface integral back to a sum of volume integrals over the different connected pieces $V_i$ of $V_1$, where $\phi_1$ is replaced by $\phi_{1i}$ which is constant over any connected volume piece $V_i$, each of those integrals can be written as

$$\phi_{1i}\int_{V_i} dV\,\nabla\cdot\mathbf{E} = 0.$$

We have thus shown that $\langle\tilde{\mathbf{E}}_1|\mathbf{E}\rangle = 0$ for $u \neq 1$.

The physical significance of the Class 2 eigenstates is that at special values of $\epsilon_1/\epsilon_2$ (the eigenvalues) a wave can arise in the system spontaneously, i.e., without the presence of an incident wave or any source of radiation. Since the fields are periodic in time, the local energy density must be constant when averaged over one period. However, if the eigenfunction is an outgoing propagating wave at large distances then it constantly radiates energy out to infinity. In order to preserve the local energy density the system must therefore create energy. For this to happen then at least one of the two constituent permittivities must have an imaginary part with the "wrong sign." Thus, if $\epsilon_2$, which is where the outgoing wave must propagate, has a physically admissible value with an imaginary part that has the right sign, then $\epsilon_1$ will have to have an imaginary part with the wrong sign. This means, of course, that the system can never actually be at a resonance, but can only approach it if the magnitude of the wrong signed eigenvalue $\mathrm{Im}\,\epsilon_1$, is small. On the other hand, if the eigenfunction decays exponentially at large distances, and thus no energy is radiated, then the special values of $\epsilon_1/\epsilon_2$ and $s \equiv \epsilon_2/(\epsilon_2-\epsilon_1)$ can be real.

If all the eigenvalues $s_n$ are nondegenerate then the above analysis often suffices to fix the states $|\mathbf{E}_n\rangle$ as a basis of Hilbert space, subject to their normalizability. However, if the system has some symmetries, which are represented by Hermitian or unitary operators $\hat{P}_i$ that commute with $\hat{\Gamma}$, then that complicates the situation: we usually try to characterize the eigenstates of $\hat{\Gamma}$ by requiring them to also be eigenstates of those symmetry operators. However, since the operator $\hat{\Gamma}$ is symmetric we defined $\langle\tilde{\mathbf{E}}_n|\mathbf{r}\rangle \equiv \langle\mathbf{r}|\mathbf{E}_n\rangle$, whereas the requirement for the eigenstates of Hermitian operators is that $\langle\psi|\mathbf{r}\rangle = \langle\mathbf{r}|\psi\rangle^*$. An example of a symmetry generator is the infinitesimal spatial translation operator $-i\nabla$, where

$$-i\nabla\, e^{i\mathbf{q}\cdot\mathbf{r}} = \mathbf{q}\, e^{i\mathbf{q}\cdot\mathbf{r}},$$

which is relevant for any microstructure that has translational symmetry along certain directions. Clearly, the complex conjugate of any such eigenfunction will have the different eigenvalue $-\mathbf{q}$. This problem can be overcome as follows: in the subspace of the complex conjugates of all the right eigenfunctions $\langle\mathbf{r}|\mathbf{F}_n\rangle$ of $\hat{\Gamma}$ with the same eigenvalue $s_n$ as $\langle\mathbf{r}|\mathbf{E}_n\rangle$ we choose one such that $\langle\mathbf{r}|\mathbf{F}_n\rangle^*$ is a right eigenfunction of $-i\nabla$ with the same eigenvalue as $\langle\mathbf{r}|\mathbf{E}_n\rangle$. This is done in Sec. III below for the particular case of a flat-slab microstructure.

## III. EIGENSTATES OF A FLAT-SLAB MICROSTRUCTURE

Consider a medium with electric permittivity $\epsilon_2$ in which there is a flat slab, of thickness $2d$, with a different electric permittivity $\epsilon_1$ (see Fig. 1). The magnetic permeabilty is everywhere equal to 1, as in the vacuum [here and throughout this article we use Gaussian units for all electromagnetic (EM) quantities]. This is also the structure of a Veselago Lens, which will be discussed in Sec. IV below.

This microstructure is uniform in all $x, y$ planes; therefore, all the eigenstates can have the form

$$\langle\mathbf{r}|\mathbf{E}_n\rangle = e^{i\mathbf{k}\cdot\boldsymbol{\rho}}\mathbf{f}(z),$$

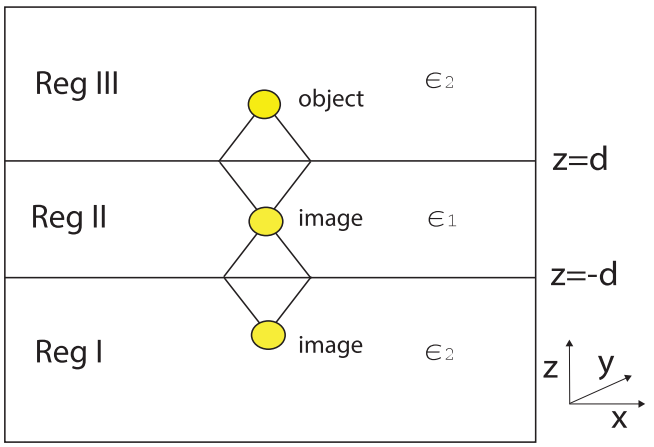


FIG. 1. Illustration of the setup of an $\epsilon_1$ slab in an $\epsilon_2$ medium. The object and images according to geometrical optics are represented by circles.

where $\mathbf{k}$ is a real 2D wave vector in the $x,y$ plane, while $\boldsymbol{\rho}$ is a 2D position vector in that plane. It is easy to show that $\mathbf{f}(z)$ satisfies the following ordinary second order differential equation:

$$\left(\frac{d^2}{dz^2}+k_{2z}^2\right)\mathbf{f}=uk_2^2\theta_1(\mathbf{r})\mathbf{f},$$

where $\theta_1(\mathbf{r})=1$ for $|z|<d$ and vanishes elsewhere. In each region of $z$ this is a one-dimensional Helmholtz equation, the solution of which is a linear combination of sine and cosine functions with coefficients that must satisfy $\boldsymbol{\nabla}\cdot\mathbf{E}=0$ in each region. They must also satisfy the outgoing wave condition for $|z|>d$ and continuity requirements on $E_x$ and $E_y$ and $D_z\equiv\epsilon E_z$, as well as on all components of the magnetic field, at the $\epsilon_1$, $\epsilon_2$ interfaces. The microstructure is also invariant under the reflection $z\to -z$. These symmetries are not violated by complex conjugation of the eigenfunctions. Therefore, the eigenfunctions can be characterized as transverse electric (TE) or transverse magnetic (TM), and also as even (+) or odd (−) under $z\to -z$.

In the following subsections we will first find closed form expressions for the eigenstates and closed form expressions for the nonlinear equation whose solutions are the eigenvalues. In order to discuss qualitatively the properties of the eigenvalues we will restrict our considerations to the case where $\epsilon_2$ is real and positive. In that case, when $|\mathbf{k}|<k_2$, $k_{2z}=\sqrt{k_2^2-|\mathbf{k}|^2}$ is real and the mode propagates out of the slab. However, when $|\mathbf{k}|>k_2$, $k_{2z}=\sqrt{k_2^2-|\mathbf{k}|^2}$ is imaginary and the mode decays away from the slab. We refer to these modes, respectively, as propagating and evanescent modes. When $|\mathbf{k}|=k_2$, $k_{2z}=0$ and the mode propagates parallel to the slab without any decay or radiation away from the slab.

In Sec. III C we will describe numerical calculations of the eigenvalues for the general nonquasistatic cases [Eqs. (3.1) and (3.3)] and their consequences. When the physical value of $\epsilon_1$ is very close to one of the eigenvalues the contribution of this eigenstate to the physical electric field can become very large, greatly exceeding the field in the absence of the $\epsilon_1$ layer (Region II). When the physical $\epsilon_2\approx-\epsilon_1$ then $s\approx 1/2$ and $s_k/(s-s_k)$ becomes very large for many of the TM eigenstates when $k$ is large. This may lead to a large contribution of the large $|\mathbf{k}|$ modes to the expansion of the electric field in Eq. (2.17), as already found earlier in the quasistatic regime [6,7].

### A. TM modes

Those are

$$\mathbf{E}_{\mathbf{k}}^{+}=e^{i\mathbf{k}\cdot\boldsymbol{\rho}}\begin{cases}e^{-ik_{2z}z}A_k^{+}\left(\mathbf{e}_z\frac{k}{k_{2z}}+\mathbf{e}_{\mathbf{k}}\right), & \mathbf{r}\in\mathrm{I},\\ B_k^{+}\left(-\mathbf{e}_z\frac{ik}{k_{1z}^{+}}\sin\left(k_{1z}^{+}z\right)+\mathbf{e}_{\mathbf{k}}\cos\left(k_{1z}^{+}z\right)\right), & \mathbf{r}\in\mathrm{II},\\ e^{ik_{2z}z}A_k^{+}\left(-\mathbf{e}_z\frac{k}{k_{2z}}+\mathbf{e}_{\mathbf{k}}\right), & \mathbf{r}\in\mathrm{III},\end{cases}$$

$$\mathbf{E}_{\mathbf{k}}^{-}=e^{i\mathbf{k}\cdot\boldsymbol{\rho}}\begin{cases}e^{-ik_{2z}z}A_k^{-}\left(\mathbf{e}_z\frac{k}{k_{2z}}+\mathbf{e}_{\mathbf{k}}\right), & \mathbf{r}\in\mathrm{I},\\ B_k^{-}\left(\mathbf{e}_z\frac{ik}{k_{1z}}\cos\left(k_{1z}^{-}z\right)+\mathbf{e}_{\mathbf{k}}\sin\left(k_{1z}^{-}z\right)\right), & \mathbf{r}\in\mathrm{II},\\ e^{ik_{2z}z}A_k^{-}\left(\mathbf{e}_z\frac{k}{k_{2z}}-\mathbf{e}_{\mathbf{k}}\right), & \mathbf{r}\in\mathrm{III},\end{cases}$$

where $\mathbf{e}_{\mathbf{k}}\equiv\mathbf{k}/|\mathbf{k}|$, $k_{1z}^{\pm}\equiv\sqrt{(k_1^{\pm})^2-\mathbf{k}^2}$, $k_{2z}\equiv\sqrt{(k_2)^2-\mathbf{k}^2}$, $k_1^{\pm}\equiv\sqrt{\epsilon_1^{\pm}}\omega/c$, $k_2\equiv\sqrt{\epsilon_2}\omega/c$, and where $\boldsymbol{\nabla}\cdot\mathbf{E}=0$ is already satisfied in Regions I, II, and III. Note that $E_z^{+}$ (i.e., the $z$ component of $\mathbf{E}_{\mathbf{k}}^{+}$) changes sign under the reflection $z\to -z$. Thus $E_z^{+}(-z)=-E_z^{+}(z)$ but $E_{\mathbf{k}}^{+}(-z)=E_{\mathbf{k}}^{+}(z)$ (this is the $x,y$-plane component of $\mathbf{E}_{\mathbf{k}}^{+}$) in the even modes while $E_z^{-}(-z)=E_z^{-}(z)$ but $E_{\mathbf{k}}^{-}(-z)=-E_{\mathbf{k}}^{-}(z)$ in the odd modes. For $k=0$ $\mathbf{e}_{\mathbf{k}}$ is not defined and we can replace it by $\mathbf{e}_x$. The $A$ and $B$ coefficients are determined by the continuity requirements on the tangential components of $\mathbf{E}$ and the normal component of $\mathbf{D}\equiv\epsilon\mathbf{E}$ at the two interfaces $z=\pm d$. We thus get

$$B_k^{\pm}\begin{Bmatrix}\cos(k_{1z}^{+}d)\\ -\sin(k_{1z}^{-}d)\end{Bmatrix}=A_k^{\pm}e^{ik_{2z}d},$$

$$\frac{i\epsilon_1^{\pm}B_k^{\pm}}{k_{1z}^{\pm}}\begin{Bmatrix}\sin(k_{1z}^{+}d)\\ \cos(k_{1z}^{-}d)\end{Bmatrix}=\epsilon_2A_k^{\pm}\frac{e^{ik_{2z}d}}{k_{2z}}.$$

From these two homogeneous linear equations for $A_k^{\pm}$ and $B_k^{\pm}$ we get the following nonlinear equation for the eigenvalues of $\epsilon_{1k}^{\pm}$ which also depend upon $k\equiv|\mathbf{k}|$ but not on the direction of $\mathbf{k}$:

$$\frac{\epsilon_2}{\epsilon_{1k}^{\pm}}=\frac{ik_{2z}}{k_{1z}^{\pm}}\begin{Bmatrix}\tan\left(dk_{1z}^{+}\right)\\ -\cot\left(dk_{1z}^{-}\right)\end{Bmatrix}. \tag{3.1}$$

From this equation it follows that the eigenvalues of $k_{1z}^{\pm}$ and $\epsilon_{1k}^{\pm}$ depend only on the magnitude $k$ of the 2D wave vector $\mathbf{k}$. The eigenfunctions depend on the direction of that vector only through the $e^{i\mathbf{k}\cdot\boldsymbol{\rho}}$ factor. When $\epsilon_2$ is real and positive and $k>k_2$ then $k_{2z}$ is imaginary and the eigenstate is evanescent and nonradiating. Also, we can write $k_{2z}\equiv i\kappa_{2z}$, leading to the following form for the eigenvalue equation:

$$-\frac{\epsilon_2}{\epsilon_{1k}^{\pm}}=\frac{\kappa_{2z}}{k_{1z}^{\pm}}\begin{Bmatrix}\tan\left(dk_{1z}^{+}\right)\\ -\cot\left(dk_{1z}^{-}\right)\end{Bmatrix}.$$

From the above remark it follows that the solutions for $\epsilon_{1k}^{\pm}$ and $s_k^{\pm}$ are real and involve no dissipation and no creation of energy. Many of those $\epsilon_{1k}^{\pm}$ eigenvalues are negative and therefore the appropriate values of $s_k^{\pm}$ lie between 0 and 1, as we found in the past for all the $s_k^{\pm}$ eigenvalues in the quasistatic limit [6].

When $k$ is less than $k_2$ then $k_{2z}$ is real and the eigenstates will be radiating energy away from the $\epsilon_1$ slab. In that case the eigenvalues $k_{1z}^{\pm}$ will be complex and usually have real and imaginary parts, as can be seen from Eq. (3.1). In this case $\epsilon_1^{\pm}$ must have an imaginary part with the "wrong sign" so as to create energy that compensates for the radiation losses.

When $k$ is much larger than both $k_1^{\pm}$ and $k_2$ we get $\kappa_{1z}^{\pm} \approx -k$, $\kappa_{2z} \approx -k$, and consequently the eigenvalue equation becomes

$$\frac{\epsilon_2}{\epsilon_{1k}^{\pm}} = -\begin{Bmatrix} \tanh(dk) \\ \coth(dk) \end{Bmatrix}.$$

This agrees with results previously found in the quasistatic limit for all values of $\mathbf{k}$ [6,7]. Clearly, when $dk \to \infty$ we get $\epsilon_2/\epsilon_{1k}^{\pm} \to -1$ or $s_k^{\pm} \to 1/2$, which is therefore an accumulation point of the TM eigenvalues.

The eigenfunction $\tilde{\mathbf{E}}_{\mathbf{k}}^{\mp}(\mathbf{r})$, which is dual to $\mathbf{E}_{\mathbf{k}}^{\mp}(\mathbf{r})$, is now chosen as

$$\langle \mathbf{r}|\mathbf{E}_{\mathbf{k}}^{\mp}\rangle = \mathbf{E}_{\mathbf{k}}^{\mp}(\mathbf{r}), \quad \langle \mathbf{r}|\tilde{\mathbf{E}}_{\mathbf{k}}^{\mp}\rangle = [\mathbf{E}_{-\mathbf{k}}^{\mp}(\mathbf{r})]^*, \ \langle \tilde{\mathbf{E}}_{\mathbf{k}}^{\mp}|\mathbf{r}\rangle = \langle \mathbf{r}|\mathbf{E}_{-\mathbf{k}}^{\mp}\rangle.$$

It follows that any eigenstate is orthogonal to any dual eigenstate with a different value of the 2D wave vector $\mathbf{k}$.

Even though $|\mathbf{E}_{\mathbf{k}}^{-}\rangle$ and $\langle \tilde{\mathbf{E}}_{\mathbf{k}}^{+}|$ are assured to be orthogonal because they usually have different eigenvalues, we also verified this by a direct calculation:

$$\langle \tilde{\mathbf{E}}_{\mathbf{k}}^{+}|\mathbf{E}_{\mathbf{k}}^{-}\rangle = \int_{|z|<d} dV\, \mathbf{E}_{-\mathbf{k}}^{+}(\mathbf{r}) \cdot \mathbf{E}_{\mathbf{k}}^{-}(\mathbf{r}) = 0.$$

A similar direct calculation leads to $\langle \tilde{\mathbf{E}}_{\mathbf{k}}^{-}|\mathbf{E}_{\mathbf{k}}^{+}\rangle = 0$.

The inner product of a TM mode and its dual leads to the following normalization integral ($L_x$, $L_y$ are the system sizes in the $x, y$ plane):

$$\frac{\langle \tilde{\mathbf{E}}_{\mathbf{k}}^{\pm}|\mathbf{E}_{\mathbf{k}}^{\pm}\rangle}{L_x L_y} = \frac{(B_k^{\pm})^2}{k_{1z}^{\pm 2}}\left[-(k_1^{\pm})^2 d \pm \left(\left(k^2 - k_{1z}^{\pm 2}\right)\sin(2k_{1z}^{\pm}d)/2k_{1z}^{\pm}\right)\right]. \tag{3.2}$$

### B. TE modes

Those are

$$\mathbf{E}_{\mathbf{k}}^{+} = e^{i\mathbf{k}\cdot\boldsymbol{\rho}} \begin{cases} \mathbf{e}_{\perp} A_{\perp}^{+} e^{-ik_{2z}z}, & \mathbf{r} \in \mathrm{I}, \\ \mathbf{e}_{\perp} B_{\perp}^{+} \cos(k_{1z}^{+}z), & \mathbf{r} \in \mathrm{II}, \\ \mathbf{e}_{\perp} A_{\perp}^{+} e^{ik_{2z}z}, & \mathbf{r} \in \mathrm{III}, \end{cases}$$

$$\mathbf{E}_{\mathbf{k}}^{-} = e^{i\mathbf{k}\cdot\boldsymbol{\rho}} \begin{cases} -\mathbf{e}_{\perp} A_{\perp}^{-} e^{-ik_{2z}z}, & \mathbf{r} \in \mathrm{I}, \\ \mathbf{e}_{\perp} B_{\perp}^{-} \sin(k_{1z}^{-}z), & \mathbf{r} \in \mathrm{II}, \\ \mathbf{e}_{\perp} A_{\perp}^{-} e^{ik_{2z}z}, & \mathbf{r} \in \mathrm{III}, \end{cases}$$

where $\mathbf{e}_{\perp} \equiv \mathbf{e}_{\mathbf{k}} \times \mathbf{e}_z$. Note that $E_{\perp}$ is parallel to the slab and therefore does not change sign under the reflection $z \to -z$. Here $\nabla \cdot \mathbf{E} = 0$ and $\nabla \cdot \mathbf{B} = 0$ are satisfied automatically in the various regions. However, we need to impose the continuity of $\mathbf{E} \parallel \mathbf{e}_{\perp}$ and $\mathbf{B}$. This leads to

$$A_{\perp}^{\pm} e^{ik_{2z}d} = B_{\perp}^{\pm} \begin{Bmatrix} \cos(k_{1z}^{+}d) \\ \sin(k_{1z}^{-}d) \end{Bmatrix},$$

$$\mp ik_{2z} A_{\perp}^{\pm} e^{ik_{2z}d} = k_{1z}^{\pm} B_{\perp}^{\pm} \begin{Bmatrix} \sin(k_{1z}^{+}d) \\ \cos(k_{1z}^{-}d) \end{Bmatrix},$$

and hence to the following equation for the TE eigenvalues:

$$\frac{ik_{2z}}{k_{1z}^{\pm}} = \begin{Bmatrix} -\tan(k_{1z}^{+}d) \\ \cot(k_{1z}^{-}d) \end{Bmatrix}. \tag{3.3}$$

If $k < k_2$ then $k_{2z}$ is real and the eigenstates will be radiating states. Solutions of Eq. (3.3) for $k_{1z}^{\pm}$ will therefore have a real part and an imaginary part and the eigenvalues $\epsilon_{1k}^{\pm}$ will have an imaginary part with the wrong sign.

If $k > k_2$, then $k_{2z} = i\kappa_{2z}$ is imaginary and the eigenstates will be evanescent nonradiating states. Therefore, the $\epsilon_{1k}^{\pm}$ and $s_k^{\pm}$ eigenvalues are real and involve no dissipation and no creation of energy. Equation (3.3) then becomes

$$-\frac{\kappa_{2z}}{k_{1z}^{\pm}} = \begin{Bmatrix} -\tan(dk_{1z}^{+}) \\ \cot(dk_{1z}^{-}) \end{Bmatrix}.$$

Some consideration leads to the conclusion that all the solutions of this equation for $k_{1z}^{\pm}$ will be either pure real, in which case $\epsilon_{1k}^{\pm} > \epsilon_2$ and $s_k^{\pm} < 0$, or else pure imaginary. In the quasistatic limit, when $k_2/k \to 0^+$, the numerical calculations show that $\epsilon_2/\epsilon_1^{\pm} \to 0^-$ and therefore also $s_k^{\pm} \to 0^-$. Consequently, these states do not contribute to the expansion of Eq. (2.17) for the local physical field.

The normalization integral of the TE modes is

$$\frac{\langle \tilde{\mathbf{E}}_{\mathbf{k}}^{\pm}|\mathbf{E}_{\mathbf{k}}^{\pm}\rangle}{L_x L_y} = (B_{\perp}^{\pm})^2 \begin{Bmatrix} \int_{-d}^{d} dz\, \cos^2(k_{1z}^{+}z) \\ \int_{-d}^{d} dz\, \sin^2(k_{1z}^{-}z) \end{Bmatrix}$$

$$= \frac{(B_{\perp}^{\pm})^2}{2k_{1z}^{\pm}}\left[2k_{1z}^{\pm}d \pm \sin\left(2k_{1z}^{\pm}d\right)\right] \neq 0.$$

### C. Calculation of the eigenvalues

The permittivity values and the slab thickness in the following calculations correspond to the values in the experiment with the PMMA-silver-photoresist setup described in Ref. [12], where in our case $\epsilon_1$ is the silver permittivity and $\epsilon_2$ is the average permittivity of PMMA and the photoresist. These permittivity values are appropriate for a free-space wavelength of 365 nm. We calculated the eigenvalues of the even and odd TM and TE modes according to Eqs. (3.1) and (3.3), respectively, for $2d = 35$ nm, $\lambda = 365$ nm, and $\epsilon_2 = 2.57 + 0.09i$. For any choice of $k \equiv |\mathbf{k}|$ there is an infinite number of solutions to the eigenvalue equations. Fortunately, for modes with high eigenvalues $\epsilon_{1k}$, $s_k/(s - s_k) \to 0$ and these modes give a negligible contribution to the expansion of the electric field [see Eq. (2.17)]. We define these modes as the high order modes and associate low mode index numbers to the modes with low $\epsilon_{1\mathbf{k}}$ values.

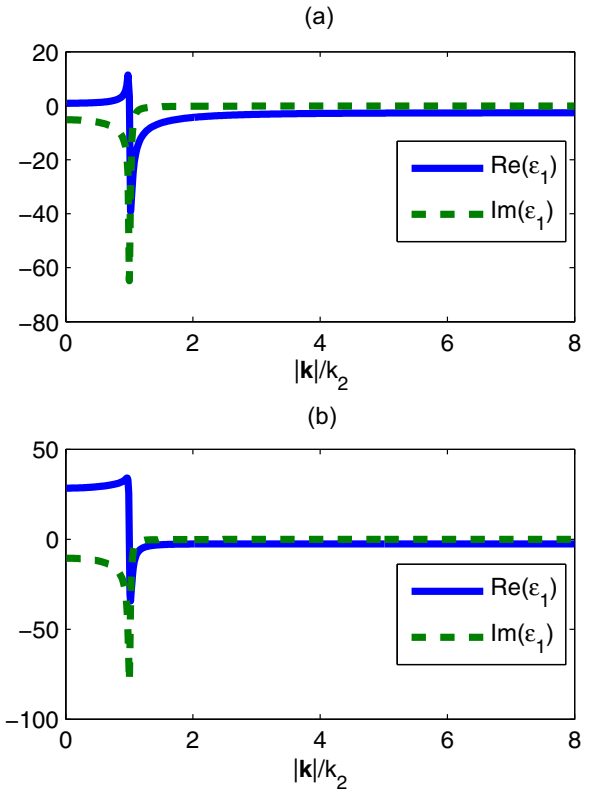


FIG. 2. Eigenvalues for the first even (a) and odd (b) TM modes as functions of $|\mathbf{k}|$.

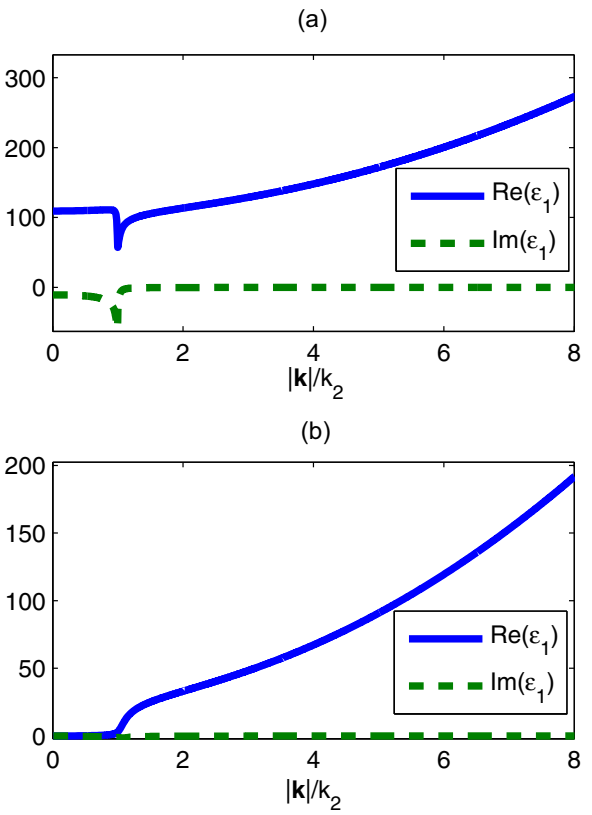


FIG. 3. Eigenvalues for the second even (a) and odd (b) TM modes as functions of $|\mathbf{k}|$.

#### *1. Eigenvalues of the TM modes*

In Fig. 2 we present the eigenvalues of the first even and odd TM modes as functions of $|\mathbf{k}|$. It can be seen that in the limit $|\mathbf{k}| \to \infty$ the eigenvalues $\epsilon_{1\mathbf{k}}$ tend to $-\epsilon_2$ and hence $s_{\mathbf{k}} \approx 1/2$. Thus, when the physical $\epsilon_2 \approx -\epsilon_1$, $s \approx 1/2$ and $s_k/(s - s_k) \to \infty$. Thus the evanescent eigenstates which have spatial frequencies $|\mathbf{k}| > k_2$ play an important role in the imaging and can lead to an enhanced resolution image as argued in Ref. [5].

In Fig. 3 we present the eigenvalues of the second even and odd TM modes as functions of $|\mathbf{k}|$. The second even mode has high values of $\mathrm{Re}(\epsilon_{1k})$ which means that $s_k/(s - s_k) \approx 0$ and the contribution of this mode to the expansion is very small. Interestingly, the second odd mode, even though for large values of $|\mathbf{k}|$ has high values of $\mathrm{Re}(\epsilon_{1\mathbf{k}})$, in the range where $|\mathbf{k}| \approx 0$ has $\epsilon_{1k} \approx 0$ which means that $s_k/(s - s_k)$ is not negligible for our physical $\epsilon_1$ and can become large for $\epsilon_1 \approx 0$.

Since the eigenstates do not decay in magnitude with time, one should expect that there should be constructive interference inside the slab. To verify this we calculated for the $\mathbf{k} = 0$ eigenstates of the first two even and odd TM modes the phase accumulated due to the propagation in the $z$ and $-z$ directions inside the slab and the double reflection from the interfaces. The total phases for the roundtrips inside the slab which were calculated were all integer multiples of $2\pi$ as expected.

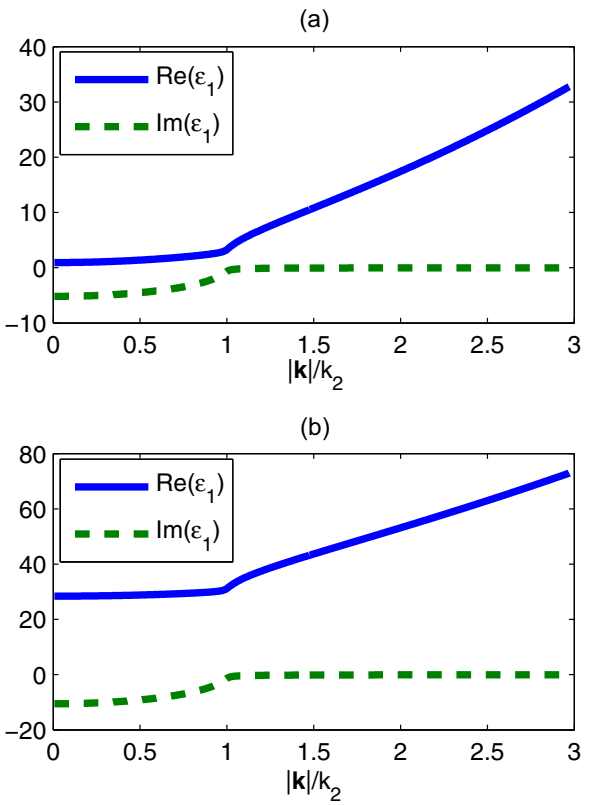


FIG. 4. Eigenvalues for the first even (a) and odd (b) TE modes as functions of $|\mathbf{k}|$.

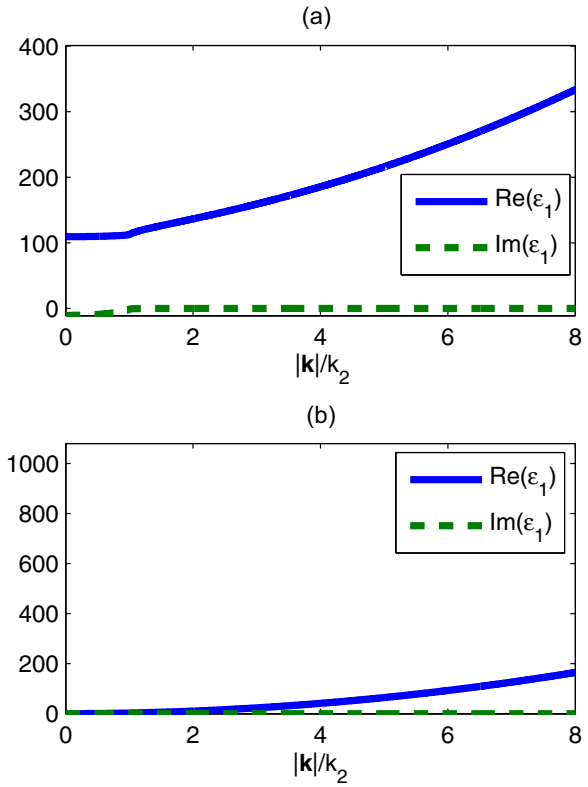


FIG. 5. Eigenvalues for the second even (a) and odd (b) TE modes as functions of $|\mathbf{k}|$.

#### 2. *Eigenvalues of the TE modes*

In Fig. 4 we present the eigenvalues of the first even and odd TE modes as functions of $|\mathbf{k}|$. It can be seen that in the limit $|\mathbf{k}| \to \infty$ the eigenvalues $\epsilon_{1\mathbf{k}}$ tend to infinity. When $|\mathbf{k}| = 0$ the modes propagate perpendicular to the slab and can therefore be defined both as TM and TE. This is apparent in the equality of the TM and TE eigenvalues at $|\mathbf{k}| = 0$.

In Fig. 5 we present the eigenvalues of the second even and odd TE modes as functions of $|\mathbf{k}|$. Here, too, the eigenvalues at $|\mathbf{k}| = 0$ are the same as those of the TM modes. It can also be seen that the first even and second odd TE modes at $|\mathbf{k}| \approx 0$ can give a small and a significant contribution to the expansion of $\mathbf{E}(\mathbf{r})$, respectively, since their $\epsilon_{1k}$ values are not far from physical values of $\epsilon_1$. On the other hand, the first odd and second even TE modes should give a negligible contribution to the expansion since their $\epsilon_{1k}$ values are far from physical values of $\epsilon_1$. Interestingly, the eigenvalues of the second odd TE mode have a small imaginary part and are close to physical $\epsilon_1$ values which are realizable in experiments.

## IV. USING THE EIGENSTATE EXPANSION TO CALCULATE THE ELECTRIC FIELD OF A POINT ELECTRIC DIPOLE IN A FLAT-SLAB STRUCTURE

We now use the eigenfunctions derived in Sec. III to expand the resulting electric field. Figure 1 shows this structure, where the object and images according to geometrical optics are represented by circles. We will consider oscillating electric point dipoles in Region III directed along $z$ and $x$ axes as the source of the EM field.

### A. Dipole object directed along $z$

We consider an oscillating electric point dipole at $\mathbf{r} = (0,0,z_0) \equiv \mathbf{z}_0$ in Region III directed along $z$ as the source of the EM field. The current distribution of the dipole at $\mathbf{z}_0$ can be written as $\mathbf{J}_{\rm dip} = -i\mathbf{e}_z\omega p\delta^3(\mathbf{r}-\mathbf{z}_0)$, where $p$ is the *electric dipole moment*.

The electric field of this dipole in a uniform $\epsilon_2$ medium is

$$\mathbf{E}_0(\mathbf{r}) = \frac{1}{\epsilon_2} e^{ik_2 r}\left\{\left[k_2^2(\mathbf{n}\times\mathbf{p})\times\mathbf{n}\right]\frac{1}{r} + \left[3\mathbf{n}(\mathbf{n}\cdot\mathbf{p})-\mathbf{p}\right]\left(\frac{1}{r^3}-\frac{ik_2}{r^2}\right)\right\}, \tag{4.1}$$

where $r \equiv |\mathbf{r}-\mathbf{z}_0|, \mathbf{n} \equiv \frac{\mathbf{r}-\mathbf{z}_0}{|\mathbf{r}-\mathbf{z}_0|}$. This differs from the expression for the electric field of an electric point dipole in vacuum [13] by the $\epsilon_2$ factor in the denominator and by the appearance of $k_2 \equiv \sqrt{\epsilon_2}\omega/c$ instead of just $\omega/c$.

Because the expression for $\mathbf{E}_0(\mathbf{r})$ can be obtained by using Green's function of Eq. (2.7) and $\mathbf{J}_{\rm dip}$ defined above, therefore the scalar product $\langle\tilde{\mathbf{E}}^{\pm}_{\mathbf{k}}|\mathbf{E}_0\rangle$, which appears in Eq. (2.17), can be written as

$$\begin{aligned}\langle\tilde{\mathbf{E}}^{\pm}_{\mathbf{k}}|\mathbf{E}_0\rangle &= -\frac{4\pi i}{\epsilon_2\omega}\int dV'\theta_1(\mathbf{r}')\mathbf{E}^{\pm}_{-\mathbf{k}}(\mathbf{r}') \\ &\quad\times\int dV\ \overleftrightarrow{G}(\mathbf{r}',\mathbf{r})\cdot\mathbf{J}_{\rm dip}(\mathbf{r}) \\ &= -\frac{4\pi i}{\epsilon_2\omega}s_k^{\pm}\int dV\ \mathbf{E}^{\pm}_{-\mathbf{k}}(\mathbf{r})\cdot\mathbf{J}_{\rm dip}(\mathbf{r}) \qquad (4.2)\\ &= -\frac{4\pi p}{\epsilon_2}s_k^{\pm}E^{\pm}_{-\mathbf{k}z}(\mathbf{z}_0). \qquad (4.3)\end{aligned}$$

It can be seen that an oscillating electric dipole introduces in $\langle\tilde{\mathbf{E}}^{\pm}_{\mathbf{k}}|\mathbf{E}_0\rangle$ an additional factor $s_k$ which leads to a singularity when $\epsilon_{1\mathbf{k}} = \epsilon_2$. This differs from the $\epsilon_{1\mathbf{k}} = \epsilon_1$ singularity which arises from $s_k/(s-s_k)$. The inner product vanishes for all of the TE modes, but for each of the TM modes we get

$$\frac{\langle\tilde{\mathbf{E}}^{\pm}_{\mathbf{k}\,\rm TM}|\mathbf{E}_0\rangle}{L_xL_y} = B_k^{\pm}\begin{Bmatrix}\cos(dk_{1z}^{+})\\ \sin(dk_{1z}^{-})\end{Bmatrix}\frac{4\pi p s_k^{\pm}k\,e^{ik_{2z}(z_0-d)}}{\epsilon_2 k_{2z}}. \tag{4.4}$$

Equation (2.17) now becomes

$$\mathbf{E}(\mathbf{r})-\mathbf{E}_0(\mathbf{r}) = \sum_{\rm TM,\,\alpha=\pm}\int\frac{d^2k}{(2\pi)^2}\frac{s_k^{\alpha}}{s-s_k^{\alpha}}\frac{\langle\tilde{\mathbf{E}}^{\alpha}_{\mathbf{k}}|\mathbf{E}_0\rangle}{\langle\tilde{\mathbf{E}}^{\alpha}_{\mathbf{k}}|\mathbf{E}^{\alpha}_{\mathbf{k}}\rangle}\mathbf{E}^{\alpha}_{\mathbf{k}}(\mathbf{r}), \tag{4.5}$$

where $\sum_{\rm TM,\,\alpha=\pm}$ means that one should sum over all the TM (+) and TM (−) eigenstates. Since the only dependence on the direction of $\mathbf{k}$ comes from the unit vector $\mathbf{e}_{\mathbf{k}}$ and the factor $e^{i\mathbf{k}\cdot\rho}$ which are in $\mathbf{E}^{\alpha}_{\mathbf{k}}(\mathbf{r})$, therefore the integration over the azimuth angle $\varphi$ between $\mathbf{k}$ and $\boldsymbol{\rho}$ can be carried out analytically, as we show in Sec. IV A 1 below. This leaves only a 1D integration over $k \equiv |\mathbf{k}|$ to be calculated numerically. Those integrals are shown below.

One can see from Eq. (4.2) that when the source is located far from the slab, the evanescent eigenstates give only a small contribution to Eq. (4.5) since they have a small amplitude at that location. This is apparent from the exponential factor in Eq. (4.4) which expresses this evanescent behavior.

#### 1. Analytic integration with respect to $\varphi$

We notice that in the eigenstate expansion the only expression which depends on the 2D orientation of $\mathbf{k}$ is $|\mathbf{E}_{\mathbf{k}}^{\pm}\rangle$. Therefore, the integration over the azimuthal angle $\varphi$ can be performed analytically,

$$\int \mathbf{E}_{\mathbf{k}}^{\pm} d\varphi = 2\pi B_k^{\pm} \begin{cases} e^{-ik_{2z}(z+d)} \begin{Bmatrix} \cos(k_{1z}^{+} d) \\ \sin(k_{1z}^{-} d) \end{Bmatrix} \left( \pm \mathbf{e}_z J_0(k\rho) \frac{k}{k_{2z}} \pm i \mathbf{e}_\rho J_1(k\rho) \right), & \mathbf{r} \in \mathrm{I}, \\ \mathbf{e}_z \frac{ik}{k_{1z}^{\pm}} \begin{Bmatrix} -\sin(k_{1z}^{+} z) \\ \cos(k_{1z}^{-} z) \end{Bmatrix} J_0(k\rho) + \mathbf{e}_\rho i J_1(k\rho) \begin{Bmatrix} \cos(k_{1z}^{+} z) \\ \sin(k_{1z}^{-} z) \end{Bmatrix}, & \mathbf{r} \in \mathrm{II}, \\ e^{ik_{2z}(z-d)} \begin{Bmatrix} \cos(k_{1z}^{+} d) \\ \sin(k_{1z}^{-} d) \end{Bmatrix} \left( -\mathbf{e}_z J_0(k\rho) \frac{k}{k_{2z}} + \mathbf{e}_\rho i J_1(k\rho) \right), & \mathbf{r} \in \mathrm{III}, \end{cases} \tag{4.6}$$

where $J_0(x)$ is a Bessel function of the first kind. Equation (4.5) now reads

$$|\mathbf{E}\rangle - |\mathbf{E}_0\rangle = \sum_{\mathrm{TM}} \sum_{+,-} \int \frac{dk}{(2\pi)^2} \frac{s_{\mathbf{k}}}{s - s_{\mathbf{k}}} \frac{\langle \tilde{\mathbf{E}}_{\mathbf{k}} | \mathbf{E}_0 \rangle}{\langle \tilde{\mathbf{E}}_{\mathbf{k}} | \mathbf{E}_{\mathbf{k}} \rangle} \left( \int |\mathbf{E}_{\mathbf{k}}\rangle d\varphi \right) k$$

$$\equiv \sum_{\mathrm{TM}} \sum_{+,-} \int dk\, \mathbf{F}(\mathbf{r},k), \tag{4.7}$$

where $(\int |\mathbf{E}_{\mathbf{k}}\rangle d\varphi)$ is given by Eq. (4.6).

#### 2. Calculation of the integrands as functions of $|\mathbf{k}|$

We calculated the integrands in Eq. (4.7) for the first two even and odd TM modes for the coordinates $z = -d, \rho = 0$. This was performed by simply substituting the physical parameters and the eigenvalues in $s_{\mathbf{k}}/(s - s_{\mathbf{k}})$ and in Eqs. (3.2), (4.4), and (4.6), where in the last expression we also substituted the coordinates. In Fig. 6 we present the integrands as functions of $|\mathbf{k}|$. It can be seen that the modes with the dominant contribution to the expansion are the first even and odd modes. The second even and odd modes give a negligible contribution and a very small contribution to the expansion, respectively (very small values of the integrand of the second even mode which cannot be seen in the figure). This validates our analysis in the previous subsection.

#### 3. Calculation of the electric field

*(a) A setup with* $\epsilon_2 = 2.57 + 0.09i$, $\epsilon_1 = -2.55 + 0.24i$. We calculated the electric field in the three regions by numerically integrating Eq. (4.7) with respect to $|\mathbf{k}|$. In Fig. 7 we present $|\mathbf{E}|^2$ in the three regions for a dipole located at $z = d + 7 \cdot (2d)/8$ and permittivity values of $\epsilon_1 = -2.55 + 0.24i$, $\epsilon_2 = 2.57 + 0.09i$. The white circles denote the object and the image expected according to geometrical optics. In this

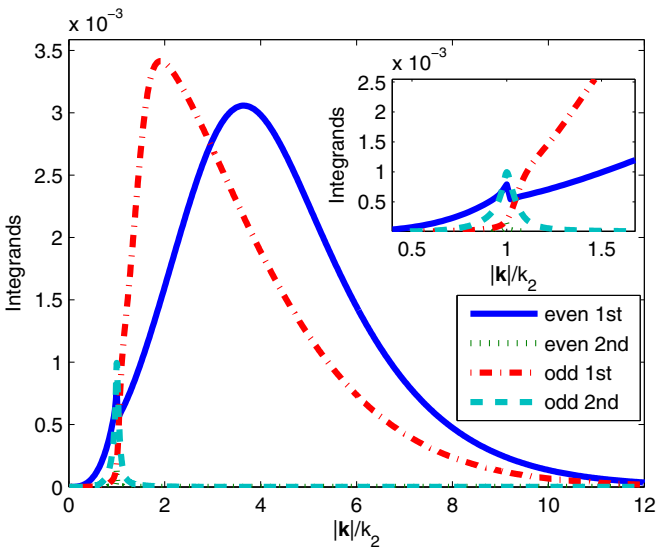


FIG. 6. Integrands of Eq. (4.7) for the first two even and odd TM modes at $\rho = 0, z = -d$.

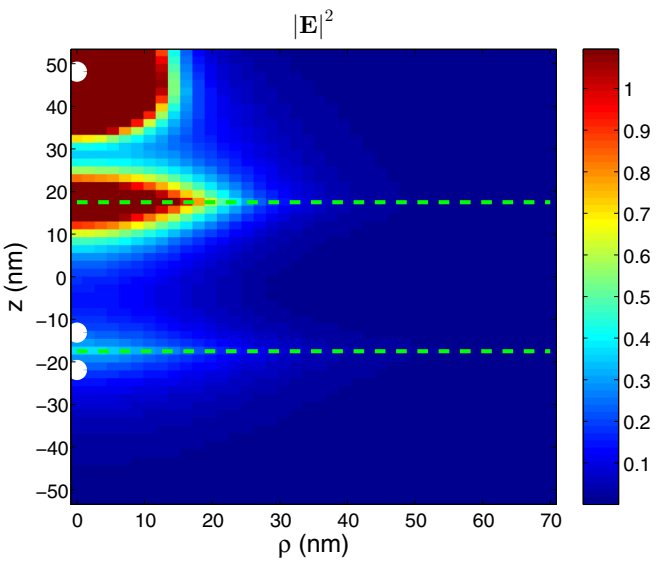


FIG. 7. $|\mathbf{E}|^2$ in the three regions for a dipole located at $\rho = 0$, $z = d + 7 \cdot (2d)/8$ and $\epsilon_1 = -2.55 + 0.24i, \epsilon_2 = 2.57 + 0.09i$.

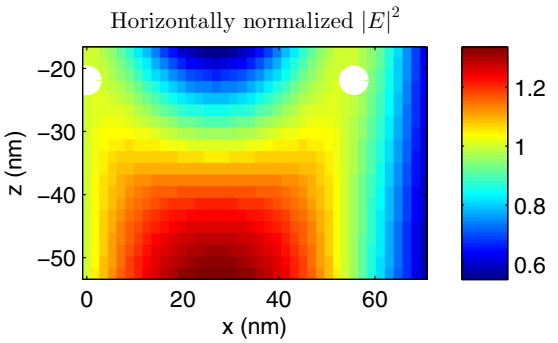


FIG. 8. Horizontally normalized $|\mathbf{E}|^2$ in Region I for two oscillating dipoles located at $z = d + 7 \cdot (2d)/8$ and $\epsilon_1 = -2.55 + 0.24i$, $\epsilon_2 = 2.57 + 0.09i$.

figure, as well as in Fig. 9 that display all the regions, we used a linear color scale. In order to present an informative figure we mapped all the values higher than a certain value to this value. Thus, in all the locations which exhibit the highest value, the actual values are often much higher than the apparent value. It can be seen that the maximal intensity is at the interfaces between the slab and the surrounding medium.

The numerical expansion of Eq. (4.7) for the local electric field $\mathbf{E}(\mathbf{r})$ is well converged even at the interface, where $\mathbf{E}(\mathbf{r})$ undergoes a discontinuous jump. This is due to the fact, mentioned after Eq. (2.17), that the expansion is in terms of a basis in Hilbert space.

At this point it is worth mentioning that exploiting the eigenstates of the previous section to calculate the physical electric field $\mathbf{E}(\mathbf{r})$ is justified as long as $1/k$ is larger, say by a factor of 10, than the scale of interface roughness and the nonlocality of $\epsilon(\mathbf{r})$.

In Fig. 8 we present $|\mathbf{E}|^2$, normalized by the maximal horizontal intensity, in Region I for two horizontally distanced electric dipole sources. The location of the second dipole was set to be such that the field intensity at the midpoint between the two images is $e^{-1/2}$ times the intensity at the image maximum. We define this distance as the separation distance needed to resolve the two images. It can be seen that the optimal resolution is at the interface between the slab and the medium. Thus the optimal imaging is at the interface between the slab and Region I in terms of both intensity and resolution. These results are in agreement with our quasistatic analysis in Ref. [7].

*(b) A setup in which $s - 1/2$ is divided by 1000.* We divided $\Delta s \equiv s - \frac{1}{2}$ by 1000 and calculated the electric field in the three regions. This setup, in which $\epsilon_1$ is much closer to $-\epsilon_2$, was expected to achieve better resolution according to the explanation in Sec. III C. In Fig. 9 we present $|\mathbf{E}|^2$ in the three regions for a dipole located at $z = d + 7 \cdot (2d)/8$ (top region) and $\Delta s$ divided by 1000. It can be seen that the intensity here is higher by more than an order of magnitude compared to the previous case.

In Fig. 10 we present the horizontally normalized $|\mathbf{E}|^2$ in Region I for two horizontally distanced dipoles. Here, too, the optimal resolution is at the interface between the slab and Region I.

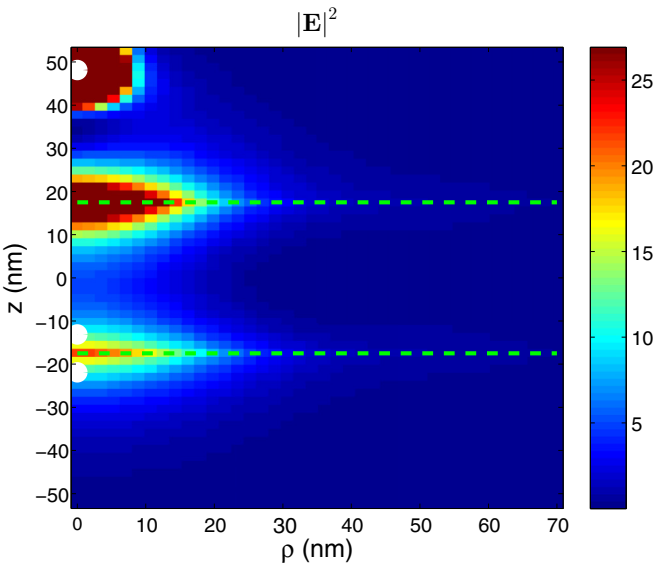


FIG. 9. $|\mathbf{E}|^2$ in the three regions for a dipole located at $z = d + 7 \cdot (2d)/8$ and $\Delta s$ divided by 1000.

In conclusion, when we decrease $\Delta s$, $\epsilon_1$ becomes closer to $\epsilon_{1\mathbf{k}}$ for the evanescent modes. Thus there is a stronger amplification of these modes and the resolution is further enhanced since modes with higher $|\mathbf{k}|$ values are exploited in the imaging. It should be noted that $\Delta s \approx 0$ can be achieved also when the imaginary parts of $\epsilon_1$ and $\epsilon_2$ have opposite signs, in which case one of the constituents exhibits dissipation, while the other exhibits gain.

### B. Dipole object directed along *x*

We consider an oscillating electric point dipole at $\mathbf{r} = (0,0,z_0) \equiv \mathbf{z}_0$ in Region III directed along $x$ as the source of the EM field. The current distribution of the dipole at $\mathbf{z}_0$ can be written as $\mathbf{J}_{\text{dip}} = -i\mathbf{e}_x \omega p \delta^3(\mathbf{r} - \mathbf{z}_0)$, where $p$ is the *electric dipole moment*. The electric field of this dipole in a uniform $\epsilon_2$ medium is given by the expression in Eq. (4.1), where $\mathbf{p} = p\mathbf{e}_x$.

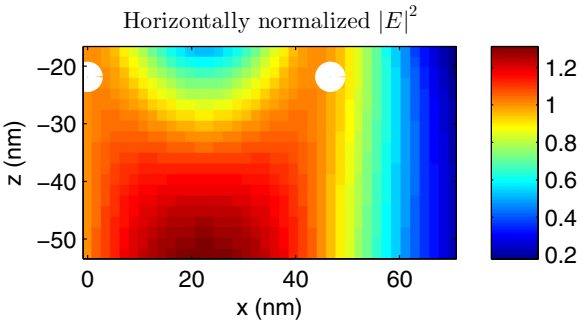


FIG. 10. Horizontally normalized $|\mathbf{E}|^2$ in Region I for two oscillating dipoles located at $z = d + 7 \cdot (2d)/8$ and $\Delta s$ divided by 1000.

### *1. Contribution of the TM modes*

We define $\varphi_{\mathbf{k}}$ as the azimuthal angle of $\mathbf{k}$ relative to $\mathbf{e}_x$ and project $\mathbf{e}_{\mathbf{k}}$ onto the $x$ and $y$ axes. We substitute $(\mathbf{e}_{\mathbf{k}} \cdot \mathbf{e}_x) = \cos\varphi_{\mathbf{k}}$, $(\mathbf{e}_{\mathbf{k}} \cdot \mathbf{e}_y) = \sin\varphi_{\mathbf{k}}$ and write the TM eigenfunctions as follows:

$$\mathbf{E}^{\pm}_{\mathbf{k}} = B^{\pm}_k e^{i\mathbf{k}\cdot\boldsymbol{\rho}} \begin{cases} \pm e^{-ik_{2z}(z+d)} \begin{Bmatrix} \cos(k_1^+ d) \\ -\sin(k_1^- d) \end{Bmatrix} \left(\mathbf{e}_z \frac{k}{k_{2z}} + \mathbf{e}_x \cos\varphi_{\mathbf{k}} + \mathbf{e}_y \sin\varphi_{\mathbf{k}}\right), & \mathbf{r} \in \mathrm{I}, \\ \mp \mathbf{e}_z \frac{ik}{k^{\pm}_{1z}} \begin{Bmatrix} \sin(k_1^+ z) \\ \cos(k_1^- z) \end{Bmatrix} + (\mathbf{e}_x \cos\varphi_{\mathbf{k}} + \mathbf{e}_y \sin\varphi_{\mathbf{k}}) \begin{Bmatrix} \cos(k_1^+ z) \\ \sin(k_1^- z) \end{Bmatrix}, & \mathbf{r} \in \mathrm{II}, \\ e^{ik_{2z}(z-d)} \begin{Bmatrix} \cos(k_1^+ d) \\ \sin(k_1^- d) \end{Bmatrix} \left(-\mathbf{e}_z \frac{k}{k_{2z}} + \mathbf{e}_x \cos\varphi_{\mathbf{k}} + \mathbf{e}_y \sin\varphi_{\mathbf{k}}\right), & \mathbf{r} \in \mathrm{III}. \end{cases} \tag{4.8}$$

The scalar product $\langle \tilde{\mathbf{E}}^{\pm}_{\mathbf{k}\,\mathrm{TM}} | \mathbf{E}_0 \rangle$ can be written according to Eq. (4.2) as

$$\frac{\langle \tilde{\mathbf{E}}^{\pm}_{\mathbf{k}\,\mathrm{TM}} | \mathbf{E}_0 \rangle}{L_x L_y} = \frac{4\pi p s^{\pm}_k}{\epsilon_2} B^{\pm}_k e^{ik_{2z}(z_0-d)} \begin{Bmatrix} \cos(k_{1z}^+ d) \\ \sin(k_{1z}^- d) \end{Bmatrix} \cos(\varphi_{\mathbf{k}}). \tag{4.9}$$

Here both $\langle \tilde{\mathbf{E}}^{\pm}_{\mathbf{k}\,\mathrm{TM}} | \mathbf{E}_0 \rangle$ and $\mathbf{E}^{\pm}_{\mathbf{k}}$ depend upon $\varphi_{\mathbf{k}}$. We change the integration variables $d^2k = k\, d\varphi_{\mathbf{k}} dk$ and integrate $\frac{\langle \tilde{\mathbf{E}}^{\pm}_{\mathbf{k}\,\mathrm{TM}} | \mathbf{E}_0 \rangle}{L_x L_y} \mathbf{E}^{\pm}_{\mathbf{k}}$ analytically with respect to the azimuthal angle $\varphi_{\mathbf{k}}$,

$$\int \frac{\langle \tilde{\mathbf{E}}^{\pm}_{\mathbf{k}\,\mathrm{TM}} | \mathbf{E}_0 \rangle}{L_x L_y} \mathbf{E}^{\pm}_{\mathbf{k}} d\varphi_{\mathbf{k}} = \frac{4\pi p s^{\pm}_k}{\epsilon_2} e^{ik_{2z}(z_0-d)} \begin{Bmatrix} \cos(k_{1z}^+ d) \\ \sin(k_{1z}^- d) \end{Bmatrix} 2\pi (B^{\pm}_k)^2$$

$$\times \begin{cases} e^{-ik_{2z}(z+d)} \begin{Bmatrix} \cos(k_{1z}^+ d) \\ -\sin(k_{1z}^- d) \end{Bmatrix} \left(\mathbf{e}_z \frac{k}{k_{2z}} i\, \cos(\varphi_{\boldsymbol{\rho}}) J_1(k\rho) + \mathbf{e}_x \left[\cos^2(\varphi_{\boldsymbol{\rho}}) J_0(k\rho) - \frac{\cos(2\varphi_{\boldsymbol{\rho}}) J_1(k\rho)}{k\rho}\right] - \mathbf{e}_y \frac{\sin(2\varphi_{\boldsymbol{\rho}})}{2} J_2(k\rho)\right), \\ \mathbf{e}_z \frac{k}{k^{\pm}_{1z}} \begin{Bmatrix} \sin(k_{1z}^+ z) \\ -\cos(k_{1z}^- z) \end{Bmatrix} \cos(\varphi_{\boldsymbol{\rho}}) J_1(k\rho) + \left(\mathbf{e}_x \left[\cos^2(\varphi_{\boldsymbol{\rho}}) J_0(k\rho) - \frac{\cos(2\varphi_{\boldsymbol{\rho}}) J_1(k\rho)}{k\rho}\right] - \mathbf{e}_y \frac{\sin(2\varphi_{\boldsymbol{\rho}})}{2} J_2(k\rho)\right) \begin{Bmatrix} \cos(k_{1z}^+ z) \\ \sin(k_{1z}^- z) \end{Bmatrix}, \\ e^{ik_{2z}(z-d)} \begin{Bmatrix} \cos(k_{1z}^+ d) \\ \sin(k_{1z}^- d) \end{Bmatrix} \left(-\mathbf{e}_z \frac{k}{k_{2z}} i\, \cos(\varphi_{\boldsymbol{\rho}}) J_1(k\rho) + \mathbf{e}_x \left[\cos^2(\varphi_{\boldsymbol{\rho}}) J_0(k\rho) - \frac{\cos(2\varphi_{\boldsymbol{\rho}}) J_1(k\rho)}{k\rho}\right] - \mathbf{e}_y \frac{\sin(2\varphi_{\boldsymbol{\rho}})}{2} J_2(k\rho)\right), \end{cases} \tag{4.10}$$

where the upper, middle, and bottom lines are for Regions I, II, and III, respectively. $\varphi_{\boldsymbol{\rho}}$ denotes the angle of $\boldsymbol{\rho}$ with respect to $\mathbf{e}_x$.

For $\rho = 0$ we obtain

$$\int \frac{\langle \tilde{\mathbf{E}}^{\pm}_{\mathbf{k}\,\mathrm{TM}} | \mathbf{E}_0 \rangle}{L_x L_y} \mathbf{E}^{\pm}_{\mathbf{k}} d\varphi_{\mathbf{k}} = \frac{4\pi p s^{\pm}_k}{\epsilon_2} e^{ik_{2z}(z_0-d)} \begin{Bmatrix} \cos(k_{1z}^+ d) \\ \sin(k_{1z}^- d) \end{Bmatrix} \pi (B^{\pm}_k)^2 \begin{cases} e^{-ik_{2z}(z+d)} \begin{Bmatrix} \cos(k_{1z}^+ d) \\ -\sin(k_{1z}^- d) \end{Bmatrix} \mathbf{e}_x, & \mathbf{r} \in \mathrm{I}, \\ \begin{Bmatrix} \cos(k_{1z}^+ z) \\ \sin(k_{1z}^- z) \end{Bmatrix} \mathbf{e}_x, & \mathbf{r} \in \mathrm{II}, \\ e^{ik_{2z}(z-d)} \begin{Bmatrix} \cos(k_{1z}^+ d) \\ \sin(k_{1z}^- d) \end{Bmatrix} \mathbf{e}_x, & \mathbf{r} \in \mathrm{III}. \end{cases} \tag{4.11}$$

### *2. Contribution of the TE modes*

By substituting $\mathbf{e}_\perp = \sin(\varphi_{\mathbf{k}})\mathbf{e}_x - \cos(\varphi_{\mathbf{k}})\mathbf{e}_y$ we arrive at the following expression for the TE eigenfunctions:

$$\mathbf{E}^{\pm}_{\mathbf{k}} = e^{i\mathbf{k}\cdot\rho} \begin{cases} \left(\sin(\varphi_{\mathbf{k}})\mathbf{e}_x - \cos(\varphi_{\mathbf{k}})\mathbf{e}_y\right) B^{\pm}_\perp \begin{Bmatrix} \cos(k_{1z}^+ d) \\ -\sin(k_{1z}^- d) \end{Bmatrix} e^{-ik_{2z}(z+d)}, & \mathbf{r} \in \mathrm{I}, \\ (\sin(\varphi_{\mathbf{k}})\mathbf{e}_x - \cos(\varphi_{\mathbf{k}})\mathbf{e}_y) B^{\pm}_\perp \begin{Bmatrix} \cos(k_{1z}^+ z) \\ \sin(k_{1z}^- z) \end{Bmatrix}, & \mathbf{r} \in \mathrm{II}, \\ (\sin(\varphi_{\mathbf{k}})\mathbf{e}_x - \cos(\varphi_{\mathbf{k}})\mathbf{e}_y) B^{\pm}_\perp \begin{Bmatrix} \cos(k_{1z}^+ d) \\ \sin(k_{1z}^- d) \end{Bmatrix} e^{ik_{2z}(z-d)}, & \mathbf{r} \in \mathrm{III}. \end{cases}$$

The scalar product $\langle \tilde{\mathbf{E}}^{\pm}_{\mathbf{k}\,\mathrm{TE}} | \mathbf{E}_0 \rangle$ can be written as

$$\frac{\langle \tilde{\mathbf{E}}^{\pm}_{\mathbf{k}\,\mathrm{TE}} | \mathbf{E}_0 \rangle}{L_x L_y} = \frac{4\pi p s^{\pm}_k}{\epsilon_2} B^{+}_\perp \begin{Bmatrix} \cos(k_{1z}^+ d) \\ \sin(k_{1z}^- d) \end{Bmatrix} e^{ik_{2z}(z_0-d)} \sin(\varphi_{\mathbf{k}}).$$

Integrating $\frac{\langle\tilde{\mathbf{E}}^{\pm}_{\mathbf{k}\,\mathrm{TE}}|\mathbf{E}_0\rangle}{L_xL_y}\mathbf{E}^{\pm}_{\mathbf{k}}$ with respect to $\varphi_{\mathbf{k}}$ we obtain

$$\int \frac{\langle\tilde{\mathbf{E}}^{\pm}_{\mathbf{k}\,\mathrm{TE}}|\mathbf{E}_0\rangle}{L_xL_y}\mathbf{E}^{\pm}_{\mathbf{k}}d\varphi_{\mathbf{k}} = \frac{4\pi p s^{\pm}_k}{\epsilon_2}(B^{\pm}_{\perp})^2\begin{Bmatrix}\cos(k_1^+d)\\ \sin(k_1^-d)\end{Bmatrix}e^{ik_{2z}(z_0-d)}$$
$$\times 2\pi\begin{cases}\left[\left(\sin^2(\varphi_{\boldsymbol{\rho}})J_0(k\rho)+\frac{\cos(2\varphi_{\boldsymbol{\rho}})J_1(k\rho)}{k\rho}\right)\mathbf{e}_x+\frac{1}{2}\sin(2\varphi_{\boldsymbol{\rho}})J_2(k\rho)\mathbf{e}_y\right]\begin{Bmatrix}\cos(k_{1z}^+d)\\ -\sin(k_{1z}^-d)\end{Bmatrix}e^{-ik_{2z}(z+d)}, & \mathbf{r}\in\mathrm{I},\\ \left[\left(\sin^2(\varphi_{\boldsymbol{\rho}})J_0(k\rho)+\frac{\cos(2\varphi_{\boldsymbol{\rho}})J_1(k\rho)}{k\rho}\right)\mathbf{e}_x+\frac{1}{2}\sin(2\varphi_{\boldsymbol{\rho}})J_2(k\rho)\mathbf{e}_y\right]\begin{Bmatrix}\cos(k_{1z}^+z)\\ \sin(k_{1z}^-z)\end{Bmatrix}, & \mathbf{r}\in\mathrm{II},\\ \left[\left(\sin^2(\varphi_{\boldsymbol{\rho}})J_0(k\rho)+\frac{\cos(2\varphi_{\boldsymbol{\rho}})J_1(k\rho)}{k\rho}\right)\mathbf{e}_x+\frac{1}{2}\sin(2\varphi_{\boldsymbol{\rho}})J_2(k\rho)\mathbf{e}_y\right]\begin{Bmatrix}\cos(k_{1z}^+d)\\ \sin(k_{1z}^-d)\end{Bmatrix}e^{ik_{2z}(z-d)}, & \mathbf{r}\in\mathrm{III}.\end{cases} \tag{4.12}$$

For $\rho=0$ we obtain

$$\int \frac{\langle\tilde{\mathbf{E}}^{\pm}_{\mathbf{k}\,\mathrm{TE}}|\mathbf{E}_0\rangle}{L_xL_y}\mathbf{E}^{\pm}_{\mathbf{k}}d\varphi_{\mathbf{k}} = \frac{4\pi p s^{\pm}_k}{\epsilon_2}(B^{\pm}_{\perp})^2\begin{Bmatrix}\cos(k_1^+d)\\ \sin(k_1^-d)\end{Bmatrix}e^{ik_{2z}(z_0-d)}\pi\begin{cases}\mathbf{e}_x\begin{Bmatrix}\cos(k_{1z}^+d)\\ -\sin(k_{1z}^-d)\end{Bmatrix}e^{-ik_{2z}(z+d)}, & \mathbf{r}\in\mathrm{I},\\ \mathbf{e}_x\begin{Bmatrix}\cos(k_{1z}^+z)\\ \sin(k_{1z}^-z)\end{Bmatrix}, & \mathbf{r}\in\mathrm{II},\\ \mathbf{e}_x\begin{Bmatrix}\cos(k_{1z}^+d)\\ \sin(k_{1z}^-d)\end{Bmatrix}e^{ik_{2z}(z-d)}, & \mathbf{r}\in\mathrm{III}.\end{cases} \tag{4.13}$$

When $k\approx 0$ for the second odd TE mode in which $\epsilon_1^-\approx 0$ we get that $k_{1z}^- = \sqrt{k_0^2\epsilon_1^- - k^2}\approx 0$ and $\langle\tilde{\mathbf{E}}^-_{\mathbf{k}}|\mathbf{E}^-_{\mathbf{k}}\rangle\approx 0$. To avoid numerical inaccuracies we approximate $\langle\tilde{\mathbf{E}}^-_{\mathbf{k}}|\mathbf{E}^-_{\mathbf{k}}\rangle$ for $k_{1z}^-\approx 0$ as follows:

$$\frac{\langle\tilde{\mathbf{E}}^-_{\mathbf{k}}|\mathbf{E}^-_{\mathbf{k}}\rangle}{L_xL_y(B^-_{\perp})^2} = d-\sin(2k_{1z}^-d)/2k_{1z}^-$$
$$\approx d-\frac{(2k_{1z}^-d)-\frac{(2k_{1z}^-d)^3}{3}}{2k_{1z}^-} = \frac{4}{3}(k_{1z}^-)^2d^3.$$

Equation (2.17) now reads

$$|\mathbf{E}\rangle-|\mathbf{E}_0\rangle = \sum_{\mathrm{TM,TE}}\sum_{+,-}\int\frac{dk}{(2\pi)^2}\frac{s_{\mathbf{k}}}{s-s_{\mathbf{k}}}\frac{\left(\int\langle\tilde{\mathbf{E}}_{\mathbf{k}}|\mathbf{E}_0\rangle|\mathbf{E}_{\mathbf{k}}\rangle d\varphi_{\mathbf{k}}\right)}{\langle\tilde{\mathbf{E}}_{\mathbf{k}}|\mathbf{E}_{\mathbf{k}}\rangle}k$$
$$\equiv\sum_{\mathrm{TM,TE}}\sum_{+,-}\int dk\,\mathbf{F}(\mathbf{r},k), \tag{4.14}$$

where $\int\langle\tilde{\mathbf{E}}_{\mathbf{k}}|\mathbf{E}_0\rangle|\mathbf{E}_{\mathbf{k}}\rangle d\varphi_{\mathbf{k}}$ is given by Eqs. (4.10), (4.11), (4.12), and (4.13) and the expressions for $s_k$ and $\langle\tilde{\mathbf{E}}_{\mathbf{k}}|\mathbf{E}_{\mathbf{k}}\rangle$ are given in Sec. III.

#### 3. Calculation of the integrands as functions of k

We calculated the integrands in Eq. (4.14) for the first two even and odd TM and TE modes for the coordinates $z=-d,\rho=0$. In Fig. 11 we present the absolute value of the integrands as functions of $|\mathbf{k}|$. It can be seen that the modes with the dominant contribution to the expansion are the first even and odd TM modes and the second odd TE mode. While the contribution of the first even and odd TM modes originates from $s_k/(s-s_k)$ since $\epsilon_{1k}\approx\epsilon_1$ for $k>k_2$, the contribution of the second odd TE mode originates from $s_k$ which appears when there are current sources since $\epsilon_{1k}\approx\epsilon_2$ for $k\approx k_2$.

#### 4. Calculation of the electric field

We calculated the electric field in the three regions by numerically integrating Eq. (4.14) with respect to $k$. In Fig. 12 we present the intensity at the $y=0$ plane for a dipole directed along $x$ axis located at $z=d+7\cdot(2d)/8$ and permittivity values of $\epsilon_1=-2.55+0.24i$, $\epsilon_2=2.57+0.09i$. It can be seen that the intensity peaks at the top interface at $x=0$ and at the bottom interface there are two peaks at $x=-23$ nm and $x=23$ nm. In Fig. 13 we present the intensity for the dipole at the $x=0$ plane. It can be seen that intensity peaks at the top and bottom interfaces at $y=0$ and that the horizontal width of the intensity is smaller compared to the previous case.

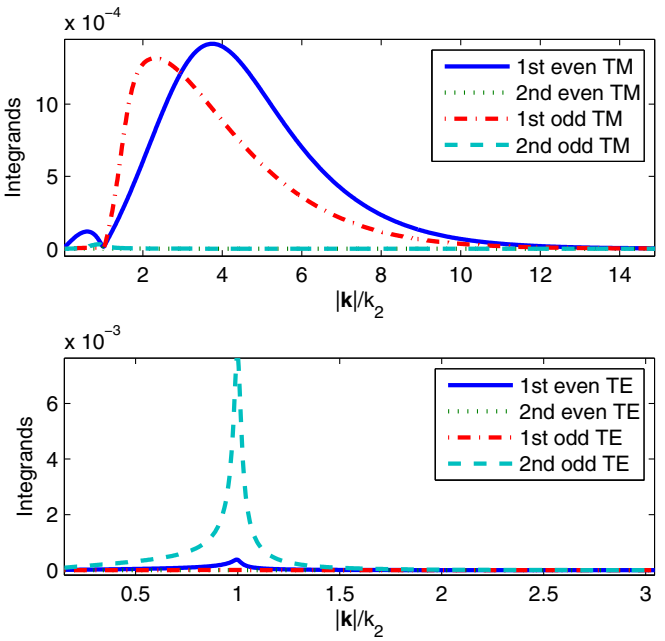


FIG. 11. Integrands of Eq. (4.14) for the first two even and odd TM and TE modes at $\rho = 0, z = -d$.

In Fig. 14 we present the horizontally normalized $|\mathbf{E}|^2$ in Region I for two dipole objects shifted in the $y$ axis. The white circles denote the images expected according to geometric optics. It can be seen that the optimal separation between the images is at the interface. In Fig. 15 we present the horizontally normalized $|\mathbf{E}|^2$ in Region I for two dipole objects shifted in the $x$ axis. Since each image is approximately composed of a sum of two Gaussians we regarded the separation between the images as the separation between the two internal Gaussians (higher intensity due to constructive interference). Here, too, the optimal separation between the images is at the interface.

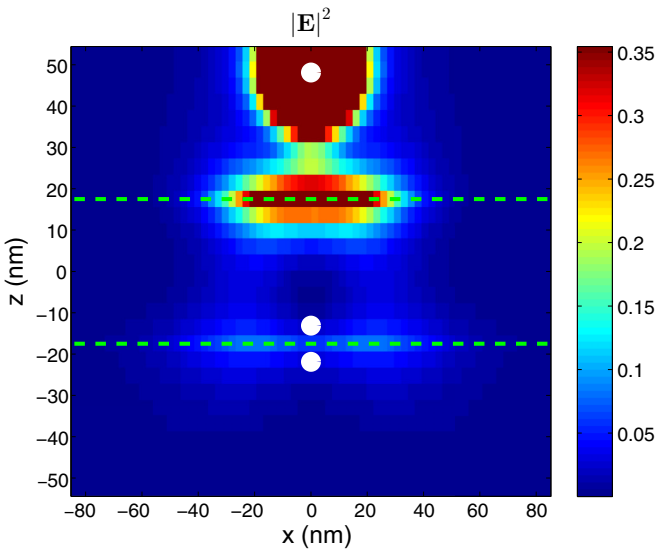


FIG. 12. $|\mathbf{E}|^2$ in the three regions for a dipole directed along $x$ located at $\rho = 0, z = d + 7 \cdot (2d)/8$ and $\epsilon_1 = -2.55 + 0.24i$, $\epsilon_2 = 2.57 + 0.09i$.

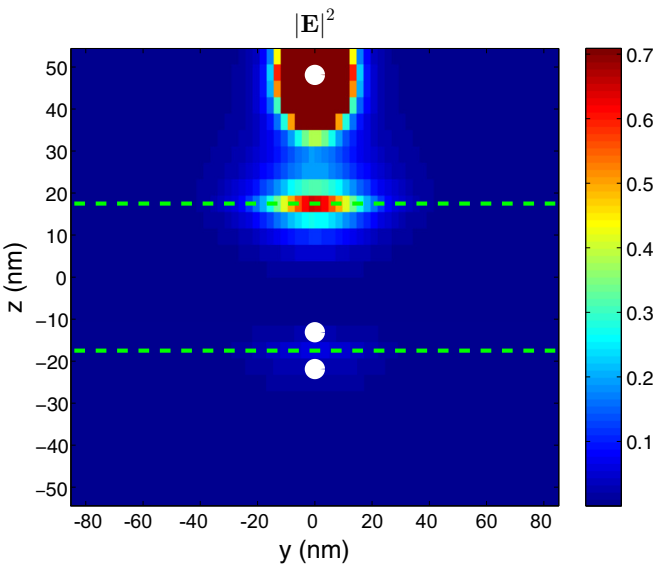


FIG. 13. $|\mathbf{E}|^2$ in the three regions for a dipole directed along $x$ located at $\rho = 0, z = d + 7 \cdot (2d)/8$ and $\epsilon_1 = -2.55 + 0.24i$, $\epsilon_2 = 2.57 + 0.09i$.

### C. Verification of the results

To verify our results we checked the continuity of the physical $D_z$ at the interfaces. This continuity is not trivially satisfied as the continuity of $D_z$ of each eigenmode is satisfied for the eigenvalue $\epsilon_{1\mathbf{k}}$ and not for the physical value of $\epsilon_1$. In fact each term in Eq. (2.17) usually violates the continuity of $D_z$ at the interfaces for the physical permittivity values. We calculated $D_z$ throughout the interfaces and it was found to be continuous to a very high precision for the perpendicular and parallel dipole calculations.

## V. DISCUSSION

We presented an exact calculation of the local electric field $\mathbf{E}(\mathbf{r})$ for a setup of an $\epsilon_1$ slab in an $\epsilon_2$ medium and a time-dependent electric point dipole $\mathbf{p}e^{-i\omega t}$ situated in the medium and directed parallel and perpendicular to the slab. For this purpose we first reformulated the differential equation which follows from Maxwell's equations as an integro-differential equation and expressed $\mathbf{E}(\mathbf{r})$ in terms of the eigenfunctions of the setup. We constructed all the TE and TM modes for the

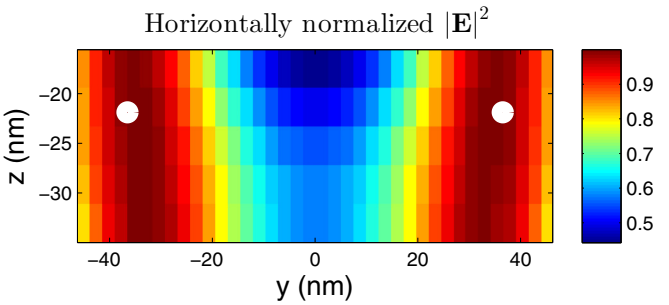


FIG. 14. Horizontally normalized $|\mathbf{E}|^2$ in Region I for two oscillating dipoles shifted in the $y$ axis located at $z = d + 7 \cdot (2d)/8$ and $\epsilon_1 = -2.55 + 0.24i, \epsilon_2 = 2.57 + 0.09i$.

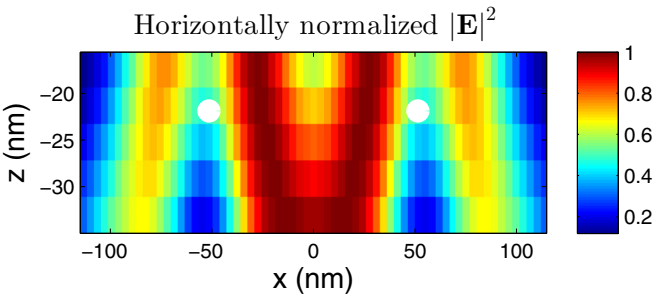


FIG. 15. Horizontally normalized $|\mathbf{E}|^2$ in Region I for two oscillating dipoles shifted in the $x$ axis located at $z = d + 7 \cdot (2d)/8$ and $\epsilon_1 = -2.55 + 0.24i, \epsilon_2 = 2.57 + 0.09i$.

setup using its symmetry properties. We then simplified the calculation of $\langle \tilde{\mathbf{E}}_n | \mathbf{E}_0 \rangle$ for external current sources in order to enable that calculation to be performed analytically. We calculated the eigenvalues of the even and odd TM and TE modes as functions of $|\mathbf{k}|$. Finally, we calculated $|\mathbf{E}|^2$ and the horizontal resolution for permittivity values which match the PMMA-silver-photoresist experiment [12] and for a setup in which $\Delta s$ is divided by 1000.

The set of eigenvalues $\epsilon_{1\mathbf{k}}$ are nonphysical values which are determined by the values of $\epsilon_2$, $\lambda$, and $d$. When the physical value of $\epsilon_1(\omega)$ of the slab becomes closer to $\epsilon_{1\mathbf{k}}$, the incoming EM wave with the same $|\mathbf{k}|$ will experience amplification. Since the eigenvalues $\epsilon_{1\mathbf{k}}$ sometimes tend to $-\epsilon_2$ when $|\mathbf{k}| \to \infty$, a slab with $\epsilon_1 \approx -\epsilon_2$ will amplify the evanescent waves, resulting in enhanced resolution. When $\epsilon_1$ further approaches $-\epsilon_2$, modes with higher $|\mathbf{k}|$ will also be employed in the imaging, resulting in further enhanced resolution. In this connection it is useful to recall that the value $\epsilon_1 = -\epsilon_2$ is an accumulation point of the eigenvalues and therefore a very singular point of Maxwell's equations. When $\epsilon_1 \to -\epsilon_2$, the physical electric field diverges in parts of the system, doing that most rapidly at the interfaces [6,7]. The optimal imaging, as in our quasistatic analysis, was found to be not at the geometric optics foci but at the interface between the slab and Region I [6,7]. In addition, when there are current sources an additional $s_k$ factor is introduced, resulting in another singularity when $\epsilon_{1k} \approx \epsilon_2$. Interestingly, the second odd TM and TE modes in the range where $|\mathbf{k}| \approx 0$ have $\epsilon_{1\mathbf{k}}^{-} \approx 0$. The second odd TE mode in the range $|\mathbf{k}| < k_2$ has $\epsilon_{1\mathbf{k}}^{-}$ which are close to real. These ranges of $\epsilon_{1\mathbf{k}}$ are not far from $\epsilon_1$ values which are realizable in experiments and may have implications in optical devices where amplification of optical signals is important. In addition, since for the second odd TE mode $\epsilon_{1k} \approx \epsilon_2$ for $k \approx k_2$ there is an enhancement of the electric field due to the additional $s_k$ factor which is introduced when there are current sources.

The formalism enables one to calculate the electric field of oscillating current sources in a simple and well convergent manner, avoiding the complex calculation of the scattering of the electric field emanating from these sources. Since current sources are used to represent polarized media and objects in imaging, the formalism can find use in many applications.

The propagating and evanescent eigenstates are related to the incoming propagating and evanescent waves, respectively, through $\langle \mathbf{E}_{-\mathbf{k}}^{\mp} | \mathbf{E}_0 \rangle$. Since $\langle \mathbf{E}_{-\mathbf{k}_1}^{\mp} | \mathbf{E}_{\mathbf{k}_2}^{\mp} \rangle \propto \delta^2(\mathbf{k}_2 - \mathbf{k}_1)$, when the incoming EM waves include waves with a given $\mathbf{k}$ as the 2D vector, the eigenmodes with the same $\mathbf{k}$ will contribute to the expansion. Thus, if the object is far from the slab and the evanescent waves reach the slab with low amplitude, the scalar product $\langle \mathbf{E}_{-\mathbf{k}}^{\mp} | \mathbf{E}_{0\mathbf{k}} \rangle$ (where $|\mathbf{E}_{0\mathbf{k}}\rangle$ denotes the $\mathbf{k}$ component of the source) will be small and the evanescent modes will have a low contribution to the expansion of the electric field.

The evanescent modes have 2D spatial frequencies $k > k_2$ and make a dominant contribution to the expansion of the electric field in enhanced resolution imaging. These modes in the $\epsilon_2$ medium decay away from the slab (maximal intensity at the interface) and do not accumulate phase along the $z$ axis (for real $k_2$). Similarly, the evanescent waves emanating from the object decay along the $z$ axis, except inside the slab in which they experience amplification [5]. Therefore, it is not surprising that the intensity of the electric field associated with these waves peaks at the interfaces between the slab and the medium.

## ACKNOWLEDGMENT

Y. Sivan is acknowledged for useful comments.

## APPENDIX A: LEFT AND RIGHT EIGENSTATES OF A SYMMETRIC OPERATOR AS A BIORTHOGONAL BASIS IN HILBERT SPACE

This Appendix is based upon material covered in Sec. II of Ref. [1].

For any state $|\psi\rangle$ in Hilbert space we define the "dual state" $|\tilde{\psi}\rangle$ by citing the following relation for its wave function representation $\langle \mathbf{r} | \tilde{\psi} \rangle$:

$$\langle \mathbf{r} | \tilde{\psi} \rangle \equiv \langle \mathbf{r} | \psi \rangle^* = \langle \psi | \mathbf{r} \rangle. \tag{A1}$$

An operator $\hat{\Gamma}$ will be called symmetric if it satisfies

$$\langle \tilde{\phi} | \hat{\Gamma} | \psi \rangle = \langle \tilde{\psi} | \hat{\Gamma} | \phi \rangle$$

for any two states $|\phi\rangle$, $|\psi\rangle$ in Hilbert space. Using the wave function representation for these states we can write their scalar product $\langle \tilde{\phi} | \psi \rangle$ in the following explicit form as an integral over space:

$$\langle \tilde{\phi} | \psi \rangle = \int d^3 r \langle \tilde{\phi} | \mathbf{r} \rangle \langle \mathbf{r} | \psi \rangle = \int d^3 r \langle \mathbf{r} | \phi \rangle \langle \mathbf{r} | \psi \rangle = \langle \tilde{\psi} | \phi \rangle. \tag{A2}$$

If $|\psi_n\rangle$ is a right eigenstate of the symmetric operator $\hat{\Gamma}$

$$\hat{\Gamma} | \psi_n \rangle = s_n | \psi_n \rangle,$$

then $\langle \tilde{\psi}_n |$ is a left eigenstate of $\hat{\Gamma}$ with same eigenvalue $s_n$ since the following holds for any state $|\psi\rangle$ in Hilbert space:

$$\langle \tilde{\psi}_n | \hat{\Gamma} | \psi \rangle = \langle \tilde{\psi} | \hat{\Gamma} | \psi_n \rangle = s_n \langle \tilde{\psi} | \psi_n \rangle = s_n \langle \tilde{\psi}_n | \psi \rangle,$$

therefore

$$\langle \tilde{\psi}_n | \hat{\Gamma} = s_n \langle \tilde{\psi}_n |. \tag{A3}$$

By considering a pair of right and left eigenstates we get that

$$\langle \tilde{\psi}_m | \hat{\Gamma} | \psi_n \rangle = s_m \langle \tilde{\psi}_m | \psi_n \rangle = s_n \langle \tilde{\psi}_m | \psi_n \rangle.$$

Thus, if $s_m \neq s_n$ then these two states must be mutually orthogonal, i.e., $\langle\tilde{\psi}_m|\psi_n\rangle = \langle\tilde{\psi}_n|\psi_m\rangle = 0$. Such a set of states is called a biorthogonal set. From Eq. (A2) it follows that the scalar product of any state $|\psi\rangle$ and its dual $|\tilde{\psi}\rangle$ becomes

$$\langle\tilde{\psi}|\psi\rangle = \int d^3r \langle\mathbf{r}|\psi\rangle^2. \tag{A4}$$

Because the integrand is not necessarily positive nor even real, this integral could possibly vanish. In order for the set of right eigenstates of $\hat{\Gamma}$ to be a complete set in Hilbert space, i.e., a basis, the scalar product of any eigenstate $|\psi_n\rangle$ and its dual must be nonzero. This needs to be verified for all the eigenstates. If this requirement is satisfied then the unit operator can be written as

$$\mathbb{1} = \sum_n \frac{|\psi_n\rangle\langle\tilde{\psi}_n|}{\langle\tilde{\psi}_n|\psi_n\rangle} \tag{A5}$$

and the state $|\psi\rangle$ can be expanded in a series of the right eigenstates $|\psi_n\rangle$,

$$|\psi\rangle = \sum_n |\psi_n\rangle \frac{\langle\tilde{\psi}_n|\psi\rangle}{\langle\tilde{\psi}_n|\psi_n\rangle}. \tag{A6}$$

These eigenstates are called a "biorthogonal basis" of Hibert space.

A complication arises when eigenstates of $\hat{\Gamma}$ are degenerate due to the existence of symmetry operators. Those are one or more Hermitian or unitary operators $\hat{P}$ that commute with $\hat{\Gamma}$. In that case we often like to select eigenstates of $\hat{\Gamma}$ that are also eigenstates of $\hat{P}$. A difficulty occurs when the complex conjugation that leads to the dual eigenstate of $\hat{\Gamma}$ results in a state which is not an eigenstate of $\hat{P}$ or is an eigenstate of $\hat{P}$ with a different eigenvalue. Such a situation occurs in the case of a spherical inclusion and also in the case of a flat-slab microstructure. The first case was discussed in Ref. [1], while the second case is discussed in Sec. III of the current article.

## APPENDIX B: QUASISTATIC RESULTS

### 1. Flat-slab modes

By taking the quasistatic limit $k_0 \to 0$ we obtain the following results for the TM modes which are associated with electrostatics:

$$\mathbf{E}^+_{\mathbf{k}} = e^{i\mathbf{k}\cdot\boldsymbol{\rho}} \begin{cases} e^{kz}A^+_k(-i\mathbf{e}_z + \mathbf{e}_{\mathbf{k}}), & \mathbf{r} \in \text{I}, \\ B^+_k(-\mathbf{e}_z i\ \sinh(kz) + \mathbf{e}_{\mathbf{k}}\cosh(kz)), & \mathbf{r} \in \text{II}, \\ e^{-kz}A^+_k(i\mathbf{e}_z + \mathbf{e}_{\mathbf{k}}), & \mathbf{r} \in \text{III}, \end{cases} \tag{B1}$$

$$\mathbf{E}^-_{\mathbf{k}} = e^{i\mathbf{k}\cdot\boldsymbol{\rho}} \begin{cases} e^{kz}A^-_k(-i\mathbf{e}_z + \mathbf{e}_{\mathbf{k}}), & \mathbf{r} \in \text{I}, \\ B^-_k(\mathbf{e}_z\cosh(kz) + \mathbf{e}_{\mathbf{k}} i\ \sinh(kz)), & \mathbf{r} \in \text{II}, \\ e^{-kz}A^-_k(-i\mathbf{e}_z - \mathbf{e}_{\mathbf{k}}), & \mathbf{r} \in \text{III}, \end{cases} \tag{B2}$$

$$\frac{\langle\tilde{\mathbf{E}}^\pm_{\mathbf{k}}|\mathbf{E}^\pm_{\mathbf{k}}\rangle}{L_xL_y} = \mp\frac{(B^\pm_k)^2}{k}\sinh(2kd). \tag{B3}$$

### 2. Results for a point dipole in Region III directed along $z$

We calculated $\langle\tilde{\mathbf{E}}^\pm_{\mathbf{k}}|\mathbf{E}_0\rangle$ in the quasistatic limit and obtained

$$\frac{\langle\tilde{\mathbf{E}}^\pm_{\mathbf{k}\,\text{TM}}|\mathbf{E}_0\rangle}{L_xL_y} = B^\pm_k \begin{Bmatrix} -i\ \cosh(dk) \\ \sinh(dk) \end{Bmatrix} \frac{4\pi p s^\pm_k e^{-k(z_0-d)}}{\epsilon_2}.$$

We performed the analytic integration with respect to $\varphi$ in the quasistatic limit,

$$\int \mathbf{E}^\pm_{\mathbf{k}} d\varphi = 2\pi B^\pm_k \begin{cases} \pm e^{k(z+d)} \begin{Bmatrix} i\cosh(kd) \\ -\sinh(kd) \end{Bmatrix} \big(-\mathbf{e}_z J_0(k\rho) + \mathbf{e}_{\boldsymbol{\rho}} J_1(k\rho)\big), & \mathbf{r} \in \text{I}, \\ \mathbf{e}_z \begin{Bmatrix} -i\sinh(kz) \\ \cosh(kz) \end{Bmatrix} J_0(k\rho) + \mathbf{e}_{\boldsymbol{\rho}} i J_1(k\rho) \begin{Bmatrix} \cosh(kz) \\ i\sinh(kz) \end{Bmatrix}, & \mathbf{r} \in \text{II}, \\ e^{-k(z-d)} \begin{Bmatrix} i\cosh(kd) \\ -\sinh(kd) \end{Bmatrix} \big(\mathbf{e}_z J_0(k\rho) + \mathbf{e}_{\boldsymbol{\rho}} J_1(k\rho)\big), & \mathbf{r} \in \text{III}. \end{cases}$$

#### *a. Region I*

The integrand in Region I is

$$\sum_{\alpha=\pm} \frac{\frac{s^\alpha_{\mathbf{k}}}{s-s^\alpha_{\mathbf{k}}}\langle\mathbf{E}^\alpha_{-\mathbf{k}}|\mathbf{E}_0\rangle \int E^\alpha_{\mathbf{k},\text{I}}(\mathbf{r}) k\, d\varphi}{(2\pi)^2\langle\tilde{\mathbf{E}}^\alpha_{\mathbf{k}}|\mathbf{E}^\alpha_{\mathbf{k}}\rangle} = \frac{k^2 p(e^{4dk}-1)e^{k(z-z_0)}}{\epsilon_2(4\Delta s^2 e^{4dk}-1)}[-J_0(k\rho)\hat{z} + J_1(k\rho)\hat{\rho}].$$

For $\Delta s = 0$ we get

$$\sum_{\alpha=\pm} \left. \frac{\frac{s_{\mathbf{k}}^{\alpha}}{s-s_{\mathbf{k}}^{\alpha}} \langle \mathbf{E}_{-\mathbf{k}}^{\alpha} | \mathbf{E}_0 \rangle \int E_{\mathbf{k},\mathrm{I}}^{\alpha}(\mathbf{r}) k \, d\varphi}{(2\pi)^2 \langle \tilde{\mathbf{E}}_{\mathbf{k}}^{\alpha} | \mathbf{E}_{\mathbf{k}}^{\alpha} \rangle} \right|_{\Delta s=0} = \frac{k^2 p (e^{4dk}-1) J_0(k\rho) e^{k(z-z_0)}}{\epsilon_2} \hat{z} - \frac{k^2 p (e^{4dk}-1) J_1(k\rho) e^{k(z-z_0)}}{\epsilon_2} \hat{\rho}. \tag{B4}$$

The integral with respect to $|\mathbf{k}|$ diverges for $z > z_0 - 4d$, which is above the geometric optics image (see Fig. 1). We integrate analytically with respect to $|\mathbf{k}|$ for $z < z_0 - 4d$, where the integral converges

$$\begin{aligned} &\int \sum_{\alpha=\pm} \left( \left. \frac{\frac{s_{\mathbf{k}}^{\alpha}}{s-s_{\mathbf{k}}^{\alpha}} \langle \mathbf{E}_{-\mathbf{k}}^{\alpha} | \mathbf{E}_0 \rangle \int E_{\mathbf{k},\mathrm{I}}^{\alpha}(\mathbf{r}) k \, d\varphi}{(2\pi)^2 \langle \tilde{\mathbf{E}}_{\mathbf{k}}^{\alpha} | \mathbf{E}_{\mathbf{k}}^{\alpha} \rangle} \right|_{\Delta s=0} \right) dk \\ &= \frac{p}{\epsilon_2} \left\{ \left[ \frac{3(4d+z-z_0)^2}{((4d+z-z_0)^2+\rho^2)^{5/2}} - \frac{1}{((4d+z-z_0)^2+\rho^2)^{3/2}} - \left( \frac{3(z-z_0)^2}{(\rho^2+(z-z_0)^2)^{5/2}} - \frac{1}{(\rho^2+(z-z_0)^2)^{3/2}} \right) \right] \hat{z} \right. \\ &\left. + \left[ \frac{3\rho(4d+z-z_0)}{(\rho^2+(4d+z-z_0)^2)^{5/2}} - \frac{3\rho(z-z_0)}{(\rho^2+(z-z_0)^2)^{5/2}} \right] \hat{\rho} \right\}. \end{aligned}$$

Adding to this expression

$$\mathbf{E}_0 = \frac{p}{\epsilon_2} \frac{1}{(\rho^2+(z-z_0)^2)^{3/2}} \left\{ \left[ \frac{3(z-z_0)^2}{\rho^2+(z-z_0)^2} - 1 \right] \hat{z} + 3 \frac{\rho(z-z_0)}{\rho^2+(z-z_0)^2} \hat{\rho} \right\},$$

we obtain

$$\mathbf{E}_{\mathrm{I}}|_{\Delta s=0} = \frac{p}{\epsilon_2} \left\{ \left[ \frac{3[z-(z_0-4d)]^2}{([z-(z_0-4d)]^2+\rho^2)^{5/2}} - \frac{1}{([z-(z_0-4d)]^2+\rho^2)^{3/2}} \right] \hat{z} + \left[ \frac{3\rho[z-(z_0-4d)]}{(\rho^2+[z-(z_0-4d)]^2)^{5/2}} \right] \hat{\rho} \right\},$$

which is the electric field of an electric point dipole located at $z = z_0 - 4d$, oriented along the $z$ axis.

#### *b. Region II*

The integrand in Region II is

$$\begin{aligned} \sum_{\alpha=\pm} \frac{\frac{s_{\mathbf{k}}^{\alpha}}{s-s_{\mathbf{k}}^{\alpha}} \langle \mathbf{E}_{-\mathbf{k}}^{\alpha} | \mathbf{E}_0 \rangle \int E_{\mathbf{k},\mathrm{II}}^{\alpha}(\mathbf{r}) k \, d\varphi}{(2\pi)^2 \langle \tilde{\mathbf{E}}_{\mathbf{k}}^{\alpha} | \mathbf{E}_{\mathbf{k}}^{\alpha} \rangle} &= \frac{k^2 p \, e^{k(d-z_0)} \cosh(dk) \operatorname{csch}(2dk) J_0(k\rho) \left[ \frac{\left(e^{2dk}-1\right)^2 \sinh(kz)}{2\Delta s \, e^{4dk}+e^{2dk}} + \frac{2 \sinh(2dk) \cosh(kz)}{2\Delta s \, e^{2dk}-1} \right]}{\epsilon_2} \hat{z} \\ &- \frac{k^2 p J_1(k\rho) \left\{ e^{2dk} \left[ 2\Delta s \left( e^{2k(d+z)}-1 \right) - 1 \right] + e^{2kz} \right\} e^{-k(z+z_0)}}{\epsilon_2 (4\Delta s^2 e^{4dk}-1)} \hat{\rho}. \end{aligned} \tag{B5}$$

For $\Delta s = 0$ we obtain

$$\left. \sum_{\alpha=\pm} \frac{\frac{s_{\mathbf{k}}^{\alpha}}{s-s_{\mathbf{k}}^{\alpha}} \langle \mathbf{E}_{-\mathbf{k}}^{\alpha} | \mathbf{E}_0 \rangle \int E_{\mathbf{k},\mathrm{II}}^{\alpha}(\mathbf{r}) k \, d\varphi}{(2\pi)^2 \langle \tilde{\mathbf{E}}_{\mathbf{k}}^{\alpha} | \mathbf{E}_{\mathbf{k}}^{\alpha} \rangle} \right|_{\Delta s=0} = -\frac{p}{\epsilon_2} \left\{ k^2 J_0(k\rho) \left[ e^{k(2d-z-z_0)} + e^{k(z-z_0)} \right] \hat{z} + k^2 J_1(k\rho) \left[ e^{k(2d-z-z_0)} - e^{k(z-z_0)} \right] \hat{\rho} \right\}. \tag{B6}$$

We add to this expression $\mathbf{E}_0$ and integrate analytically with respect to $|\mathbf{k}|$. This integral diverges for $z < 2d - z_0$, which is below the geometric optics image. For $z > 2d - z_0$, where the integral converges, we obtain

$$\mathbf{E}_{\mathrm{II}}|_{\Delta s=0} = -\frac{p}{\epsilon_2} \left\{ \left[ \frac{[3z-(2d-z_0)]^2}{([z-(2d-z_0)]^2+\rho^2)^{5/2}} - \frac{1}{([z-(2d-z_0)]^2+\rho^2)^{3/2}} \right] \hat{z} + \left[ \frac{3\rho[z-(2d-z_0)]}{([z-(2d-z_0)]^2+\rho^2)^{5/2}} \right] \hat{\rho} \right\},$$

which is the electric field of an electric point dipole located at $z = 2d - z_0$, directed in $-\hat{z}$ direction.

#### *c. Region III*

The integrand in Region III is

$$\sum_{\alpha=\pm} \frac{\frac{s_{\mathbf{k}}^{\alpha}}{s-s_{\mathbf{k}}^{\alpha}} \langle \mathbf{E}_{-\mathbf{k}}^{\alpha} | \mathbf{E}_0 \rangle \int E_{\mathbf{k},\mathrm{III}}^{\alpha}(\mathbf{r}) k \, d\varphi}{(2\pi)^2 \langle \tilde{\mathbf{E}}_{\mathbf{k}}^{\alpha} | \mathbf{E}_{\mathbf{k}}^{\alpha} \rangle} = -\frac{4p\Delta s \, \sinh(2kd) e^{4dk} k^2 e^{-k(z+z_0)}}{\epsilon_2 (4\Delta s^2 e^{4dk}-1)} [J_0(k\rho)\hat{z} + J_1(k\rho)\hat{\rho}].$$

For $\Delta s = 0$ we get

$$\sum_{\alpha=\pm} \left. \frac{\frac{s_{\mathbf{k}}^{\alpha}}{s-s_{\mathbf{k}}^{\alpha}} \langle \mathbf{E}_{-\mathbf{k}}^{\alpha} | \mathbf{E}_0 \rangle \int E_{\mathbf{k},\mathrm{III}}^{\alpha}(\mathbf{r}) k \, d\varphi}{(2\pi)^2 \langle \tilde{\mathbf{E}}_{\mathbf{k}}^{\alpha} | \mathbf{E}_{\mathbf{k}}^{\alpha} \rangle} \right|_{\Delta s=0} = 0.$$

Therefore, the electric field for $\Delta s = 0$ is

$$\mathbf{E}_{\mathrm{III}}|_{\Delta s=0} = \mathbf{E}_0 = \frac{p}{\epsilon_2}\frac{1}{(\rho^2+(z-z_0)^2)^{3/2}}\left\{\left[\frac{3(z-z_0)^2}{(\rho^2+(z-z_0)^2)}-1\right]\hat{z}+3\frac{\rho(z-z_0)}{(\rho^2+(z-z_0)^2)}\hat{\rho}\right\},$$

which is the electric field of the electric point dipole located at $z = z_0$, oriented along the $z$ axis.

For $\Delta s = 0$ the regions where the electric field diverges are between the images expected according to geometric optics in Regions I and II. This is in agreement with the conclusions in Ref. [6] where a point charge object was considered. For $\Delta s = 0$ the electric field (where it does not diverge) in Regions I, II, and III is equal to the electric field of point dipoles located at the geometric image foci directed in the $\hat{z}$, $-\hat{z}$, and $\hat{z}$ directions, respectively. This is in agreement with the results in Ref. [6] in which the electric field of a point charge object and $\Delta s = 0$, in Regions I, II, and III is equal to the electric field of point charges located at the geometric image foci.


[1] D. J. Bergman and D. Stroud, Theory of resonances in the electromagnetic scattering by macroscopic bodies, Phys. Rev. B **22**, 3527 (1980).

[2] D. J. Bergman, The dielectric constant of a two-component granular composite—a practical scheme for calculating the pole spectrum, Phys. Rev. B **19**, 2359 (1979).

[3] D. J. Bergman, The dielectric constant of a simple-cubic array of identical spheres, J. Phys. C **12**, 4947 (1979).

[4] V. G. Veselago, The electrodynamics of substances with simultaneously negative values of $\epsilon$ and $\mu$ Sov. Phys. Usp. **10**, 509 (1968).

[5] J. B. Pendry, Negative Refraction Makes a Perfect Lens, Phys. Rev. Lett. **85**, 3966 (2000).

[6] D. J. Bergman, Perfect imaging of a point charge in the quasistatic regime, Phys. Rev. A **89**, 015801 (2014).

[7] A. Farhi and D. J. Bergman, Analysis of a Veselago lens in the quasistatic regime, Phys. Rev. A **90**, 013806 (2014).

[8] N. A. Nicorovici, R. C. McPhedran, and G. W. Milton, Optical and dielectric properties of partially resonant composites, Phys. Rev. B **49**, 8479 (1994).

[9] G. W. Milton, N.-A. P. Nicorovici, R. C. McPhedran, and V. A. Podolskiy, A proof of superlensing in the quasistatic regime, and limitations of superlenses in this regime due to anomalous localized resonance, Proc. R. Soc. A **461**, 3999 (2005).

[10] G. W. Milton and N.-A. P. Nicorovici, On the cloaking effects associated with anomalous localized resonance, Proc. R. Soc. A **462**, 3027 (2006).

[11] H. Kettunen, M. Lassas, and P. Ola, On absence and existence of the anomalous localized resonance without the quasi-static approximation, arXiv:1406.6224 [math-ph].

[12] C. S. N. Fang, H. Lee, and X. Zhang, Sub-Diffraction-limited optical imaging with a silver superlens, Science **308**, 534 (2005).

[13] J. D. Jackson, *Classical Electrodynamics*, 2nd ed. (Wiley, New York, 1975), Sec. 7.3.

# Generating an electromagnetic multipole by oscillating currents

Asaf Farhi* and David J. Bergman†
*Raymond and Beverly Sackler School of Physics and Astronomy, Faculty of Exact Sciences, Tel Aviv University, IL-69978 Tel Aviv, Israel*
(Received 25 June 2017; published 28 August 2017)

Based on the relation between a plane phased array and plane waves we show that a spherical current layer or a current sphere proportional to a multipole electric field and situated in a uniform medium generates the same multipole field in all space. We calculate TE and TM multipoles inside and outside the spherical layer. The $l = 1$ TM multipoles are localized at the origin with a focal spot with full width at half maximum of $0.4\lambda$ in the lateral axes and $0.58\lambda$ in the vertical axis. The multipole fields near the origin are prescriptions for the current distributions required to generate those multipole fields. A spherical layer can couple to a multipole source since the oscillation of the electrons in the layer due to the multipole field generates the multipole field in all space, which in turn can drive the multipole currents. Exciting a multipole in a polarizable sphere or spherical layer can couple it to another polarizable sphere or spherical layer.

DOI: 10.1103/PhysRevA.96.023857

## I. INTRODUCTION

Scattering eigenstates of Maxwell's equations for a two-constituent composite medium are fields that can exist in the system without an external source for a given permittivity value (eigenvalue) of one of the constituents, which will be called the inclusion. When the outgoing waves are propagating the system radiates and that permittivity should have gain. When the outgoing waves are evanescent and the system does not radiate, that permittivity value is real.

By defining $\theta_1$ to be 1 inside the inclusion volume and zero otherwise, one can arrive from Maxwell's equations at the following equation for $\mathbf{E}(\mathbf{r})$ in Gaussian units [1]:

$$-\nabla\times(\nabla\times\mathbf{E})+k_2^2\mathbf{E}=uk_2^2\theta_1\mathbf{E}-\frac{4\pi i\omega}{c^2}\mathbf{J},$$
$$u\equiv 1-\frac{\epsilon_1}{\epsilon_2},\quad k_2^2\equiv\epsilon_2\frac{\omega^2}{c^2},\quad (1.1)$$

where $\epsilon_1$,$k_1$ are the permittivity and the wave vector of the inclusion, respectively, and $\epsilon_2$,$k_2$ are the permittivity and wave vector of the host medium. The eigenstates satisfy the following equation:

$$-\nabla\times(\nabla\times\mathbf{E}_n)+k_2^2\mathbf{E}_n=u_nk_2^2\theta_1\mathbf{E}_n,$$
$$u_n\equiv 1-\frac{\epsilon_{1n}}{\epsilon_2},\quad (1.2)$$

where $\mathbf{E}_n$ has to satisfy the electric field continuity conditions at the interface characterized by $\theta_1$.

Since $\theta_1\mathbf{E}_n$ in Eq. (1.2) plays the role of current sources, an external current proportional to an eigenstate in the inclusion volume situated in a homogeneous medium, denoted by $\mathbf{J}_{\rm ext}$, will generate the two-constituent eigenstate, namely

$$-\nabla\times(\nabla\times\mathbf{E}_n)+k_2^2\mathbf{E}_n=u_nk_2^2\theta_1\mathbf{J}_{\rm ext}.\quad (1.3)$$

In this equation the inclusion geometry is not specified and this statement is therefore applicable to any inclusion geometry and in particular for a flat slab, a cylinder, and a sphere [1–3].

The electromagnetic eigenstates for a flat slab $-a<z<a$ in a host medium are of the form [2]

$$\mathbf{E}^+_{\mathbf{k}\,\rm TE}=e^{i\mathbf{k}\cdot\boldsymbol{\rho}}\begin{cases}\mathbf{e}_\perp A^+_\perp e^{-ik_{2z}z} & z>a\\ \mathbf{e}_\perp B^+_\perp\cos(k^+_{1z}z) & -a<z<a\\ \mathbf{e}_\perp A^+_\perp e^{ik_{2z}z} & z<-a\end{cases},$$

where an even (+) TE eigenstate is presented, $\hat{\mathbf{x}}$,$\hat{\mathbf{y}}$, and $\hat{\mathbf{z}}$ are parallel and perpendicular to the slab, respectively, $k^+_{1z}\equiv\sqrt{(k^+_1)^2-\mathbf{k}^2}$, $k_{2z}\equiv\sqrt{(k_2)^2-\mathbf{k}^2}$, $k^+_1\equiv\sqrt{\epsilon^+_{1k}}\omega/c$, $k_2\equiv\sqrt{\epsilon_2}\omega/c$, $\mathbf{e}_\perp=\mathbf{e}_\mathbf{k}\times\mathbf{e}_z$, $\mathbf{e}_\mathbf{k}\equiv\mathbf{k}/|\mathbf{k}|$, $\mathbf{k}$ is a real two-dimensional (2D) wave vector in a direction parallel to the slab, $\boldsymbol{\rho}$ is a 2D position vector in that plane, and $\epsilon^+_{1k}$ is the $k$-dependent slab permittivity eigenvalue. Thus, $\mathbf{J}_{\rm ext}\propto\theta_1e^{i\mathbf{k}\cdot\boldsymbol{\rho}}\mathbf{e}_\perp B^+_\perp\cos(k^+_{1z}z)$ in a homogeneous medium will generate this eigenstate in all space.

Phased arrays are arrays of antennas with predetermined phases, which generate a desired electromagnetic wave, usually a plane wave propagating in a given direction. Optical antenna arrays are based on the polarization of a material due to an applied electric field and act as current sources at optical frequencies [4].

To understand how a plane-phased array can generate a plane wave we can operate with the free-space Green's tensor on a continuous current sheet $\mathbf{J}_{\rm ext}=\mathbf{e}_\perp e^{-i\mathbf{k}\cdot\boldsymbol{\rho}}\delta(z)$ to obtain

$$\overleftrightarrow{G}*[\mathbf{e}_\perp e^{-i\mathbf{k}\cdot\boldsymbol{\rho}}\delta(z)]\propto\mathbf{e}_\perp[\theta(z)e^{-i\mathbf{k}\cdot\boldsymbol{\rho}+ik_{2z}z}+\theta(-z)e^{-i\mathbf{k}\cdot\boldsymbol{\rho}-ik_{2z}z}],\quad (1.4)$$

where Green's tensor is defined by the following equation:

$$-\nabla\times\nabla\times\overleftrightarrow{G}+k_2^2\overleftrightarrow{G}=k_2^2I\delta^3(\mathbf{r}-\mathbf{r}')$$

and is an outgoing wave at large distances. Here $\theta(z)$ is the usual step function, $\mathbf{k}$ is a 2D wave vector parallel to the plane, and $\boldsymbol{\rho}$ is a 2D position vector in that plane. Thus, a current sheet, which is proportional to a plane wave modulated by $e^{-i\mathbf{k}\cdot\boldsymbol{\rho}}$, generates outgoing plane waves away from the current sheet with the same 2D phase modulation.

In the discussion above on the flat-slab eigenstates and the phased array we have presented volume and surface current sources modulated by a uniform medium eigenstate in the

*asaffarhi@post.tau.ac.il
†bergman@post.tau.ac.il

 

parallel directions, which generate the same uniform medium eigenstate outside the source. It will be therefore interesting to check if the same applies for sphere (and cylinder) geometries. Light usually comprises a variety of multipoles [5] and our goal is to generate only a given multipole. Vector spherical harmonics with the electric field continuity conditions are the eigenstates of a spherical inclusion [1]. Standard vector spherical harmonics are the eigenstates of a uniform medium similarly to plane waves. The analog of a planar phased array is therefore a spherical current layer modulated by a vector spherical harmonic.

Light can be localized in free space by focusing a laser beam using a circular lens. The size of the focal spot is related to the imaging resolution since the scattered light can be collected from the focal spot, enabling us to resolve features with the size of the focal spot. Smaller focal spots can thus enable us to image or sense objects with a better resolution. A laser beam with a uniform distribution passing through a circular lens has a focal spot with a full width at half maximum (FWHM) of $1.03\lambda\ f/D$ in the lateral axes, where $f$ is the focal length and $D$ is the lens diameter (commercially available lenses have $f/D \gtrsim 1$). Setups of molecules coupled to optical cavities have attracted much attention recently. In the weak-coupling regime the emission of the molecule can be enhanced and in the strong-coupling regime the system has hybrid eigenstates [6,7]. The electric field of an oscillating dipole in a setup of a sphere in a host medium has been calculated in the electrodynamic regime [8,9]. Radiation emission rates for a molecule in a dielectric sphere which also accounts for electrostatic spherical and spheroidal cavity effects have also been calculated [10]. The field outside a sphere of a spherically symmetric electrostatic multipole density has been shown to be the multipole field [11].

Here we show that a spherical current layer or a sphere modulated by a vector spherical harmonic can generate the corresponding vector spherical harmonic field both inside and outside the current layer or sphere. In addition, a spherical current layer proportional to an $l = 1$ TM mode can focus light at the origin with a focal spot with a FWHM of $0.4\lambda$ in the lateral axes and $0.58\lambda$ in the vertical axis. Such currents at optical frequencies can be effectively generated by optical antennas. Moreover, we show that a polarizable spherical layer can couple to a multipole source. In Sec. II we present the theory. In Sec. III we calculate multipole fields and present results near the origin and in the far field. In Sec. IV we discuss our results.

## II. THEORY

The electric field can be expanded in the multipoles as follows:

$$\mathbf{E} = \sum_{l,m} [i/ka_E(l,m)\boldsymbol{\nabla} \times f_l(kr)\mathbf{X}_{lm} + a_M(l,m)g_l(kr)\mathbf{X}_{lm}], \tag{2.1}$$

where $a_E, a_M$ are the multipole strengths, $f_l(kr)$, $g_l(kr)$ are linear combinations of radial Hankel functions $h_l^{(1)}, h_l^{(2)}$, and $g_l(kr)\mathbf{X}_{lm}, \boldsymbol{\nabla} \times f_l(kr)\mathbf{X}_{lm}$ are the normalized forms of the TE and TM electric field multipoles $\mathbf{E}_{lm}^{(M)}$ and $\mathbf{E}_{lm}^{(E)}$ (the vector spherical harmonics) given by

$$\mathbf{E}_{lm}^{(M)} = g_l(kr)\mathbf{L}Y_{lm}(\theta,\phi), \quad \mathbf{L} \equiv \frac{1}{i}(\mathbf{r} \times \boldsymbol{\nabla}),$$
$$\mathbf{E}_{lm}^{(E)} = \frac{i}{k}\boldsymbol{\nabla} \times \mathbf{H}_{lm}^{(E)}, \quad \mathbf{H}_{lm}^{(E)} \equiv f_l(kr)\mathbf{L}Y_{lm}(\theta,\phi), \tag{2.2}$$

where $Y_{lm}(\theta,\phi)$ are the scalar spherical harmonics.

The multipole strengths $\alpha_M(l,m)$,$\alpha_E(l,m)$ can be written as follows:

$$\alpha_M(l,m)g_l(kr) = \frac{k}{\sqrt{l(l+1)}}\int Y_{lm}^*(\mathbf{r}\cdot\mathbf{H})d\Omega,$$
$$\alpha_E(l,m)f_l(kr) = -\frac{k}{\sqrt{l(l+1)}}\int Y_{lm}^*(\mathbf{r}\cdot\mathbf{E})d\Omega. \tag{2.3}$$

Denoting the intrinsic magnetization (caused by circular currents) by $\mathbf{M}(\mathbf{x})$ the following scalar wave equation for $\mathbf{r}\cdot\mathbf{H}$, $\mathbf{r}\cdot\mathbf{E}'$, where $\mathbf{E}'$ is the divergence-free field defined by $\mathbf{E}' = \mathbf{E} + \frac{i}{\omega\epsilon_0}\mathbf{J}$ (note that $\boldsymbol{\nabla}\cdot\mathbf{E} = \rho/\epsilon_0$, $\boldsymbol{\nabla}\cdot\mathbf{J} = i\omega\rho$), can be written as

$$(\nabla^2 + k^2)(\mathbf{r}\cdot\mathbf{H}) = -i\mathbf{L}\cdot(\mathbf{J} + \boldsymbol{\nabla}\times\mathbf{M}),$$
$$(\nabla^2 + k^2)(\mathbf{r}\cdot\mathbf{E}') = k\mathbf{L}\cdot\left(\mathbf{M} + \frac{1}{k^2}\boldsymbol{\nabla}\times\mathbf{J}\right) \tag{2.4}$$

from which one can write [12]

$$\mathbf{r}\cdot\mathbf{H} = \frac{i}{4\pi}\int\frac{e^{ik|\mathbf{x}-\mathbf{x}'|}}{|\mathbf{x}-\mathbf{x}'|}\mathbf{L}'\cdot[\mathbf{J}(\mathbf{x}') + \boldsymbol{\nabla}\times\mathbf{M}(\mathbf{x}')]d^3x',$$
$$\mathbf{r}\cdot\mathbf{E}' = -\frac{k}{4\pi}\int\frac{e^{ik|\mathbf{x}-\mathbf{x}'|}}{|\mathbf{x}-\mathbf{x}'|}\mathbf{L}'\cdot\left(\mathbf{M}(\mathbf{x}') + \frac{1}{k^2}\boldsymbol{\nabla}\times\mathbf{J}(\mathbf{x}')\right)d^3x', \tag{2.5}$$

where in the region outside the sources $\mathbf{E}'$ reduces to $\mathbf{E}$.

Now $\alpha_M(l,m)$,$\alpha_E(l,m)$ read [12]

$$\alpha_M(l,m)g_l(kr) = \frac{i}{4\pi}\frac{k}{\sqrt{l(l+1)}}\int Y_{lm}^*\int\frac{e^{ik|\mathbf{x}-\mathbf{x}'|}}{|\mathbf{x}-\mathbf{x}'|}\mathbf{L}'\cdot[\mathbf{J}(\mathbf{x}') + \boldsymbol{\nabla}\times\mathbf{M}(\mathbf{x}')]d^3x'd\Omega,$$
$$\alpha_E(l,m)f_l(kr) = \frac{1}{4\pi}\frac{k^2}{\sqrt{l(l+1)}}\int Y_{lm}^*\int\frac{e^{ik|\mathbf{x}-\mathbf{x}'|}}{|\mathbf{x}-\mathbf{x}'|}\mathbf{L}'\cdot\left[\mathbf{M}(\mathbf{x}') + \frac{1}{k^2}\boldsymbol{\nabla}\times\mathbf{J}(\mathbf{x}')\right]d^3x'd\Omega. \tag{2.6}$$

We substitute $\frac{e^{ik|\mathbf{x}-\mathbf{x}'|}}{4\pi|\mathbf{x}-\mathbf{x}'|} \equiv \sum_{l,m}\mathcal{G}_l(r,r')Y_{l,m}^*(\theta',\phi')Y_{l,m}(\theta,\phi)$, where $\mathcal{G}_l(r,r') = ikj_l(kr_<)h_l^{(1)}(kr_>)$, $r_<(r_>)$ is the smaller (larger) of $r$ and $r'$. Note that $g_l(kr) = f_l(kr) = h_l^{(1)}(kr)$ outside the current layer ($r > r'$), and $g_l(kr) = f_l(kr) = j_l(kr)$ inside ($r < r'$) so one of the functions in $\mathcal{G}_l(r,r')$ cancels out with $g_l(kr)$ or $f_l(kr)$ on the left-hand side of Eq. (2.6). Consequently $\alpha_M(l,m)$,$\alpha_E(l,m)$ inside and outside take the form

$$\alpha_M^{\text{inside/outside}}(l,m) = -\frac{k^2}{\sqrt{l(l+1)}}\int\begin{Bmatrix}h_l^{(1)}(kr)\\ j_l(kr)\end{Bmatrix}Y_{lm}^*(\theta,\phi)\mathbf{L}\cdot[\mathbf{J}(\mathbf{x}) + \boldsymbol{\nabla}\times\mathbf{M}(\mathbf{x})]d^3x,$$

$$\alpha_E^{\text{inside/outside}}(l,m) = \frac{ik^3}{\sqrt{l(l+1)}} \int \begin{Bmatrix} h_l^{(1)}(kr) \\ j_l(kr) \end{Bmatrix} Y_{lm}^*(\theta,\phi)\mathbf{L} \cdot \left[\mathbf{M}(\mathbf{x}) + \frac{1}{k^2}\nabla \times \mathbf{J}(\mathbf{x})\right] d^3x, \tag{2.7}$$

where "inside" and "outside" correspond to $h_l^{(1)}(kr)$ and $j_l(kr)$, respectively. Note that in the calculations after Eq. (2.6) we have extended the discussion in Ref. [12] to the field inside the current layer.

We consider a spherical current layer situated in free space with an inner radius $r_1$ and a thickness $d$ where for the case of a surface current $d \ll r_1$. The current is proportional to a TE multipole in its $\theta,\phi$ dependence in the spherical layer $\mathbf{J} = J_0\theta_1(r)w_{l'}(kr)\mathbf{L}Y_{l'm'}(\theta,\phi)$ where $\theta_1$ is equal to 1 when $r$ is inside the current layer and is equal to zero elsewhere. However, the function $w_{l'}(kr)$ in general is not a spherical Bessel function. We assume $\mathbf{M}(\mathbf{x}) = 0$ from here on and obtain

$$\alpha_M^{\text{inside/outside}}(lm,l'm') = -k^2\sqrt{l(l+1)}J_0\,\delta_{ll'}\delta_{mm'} \times \int_{r_1}^{r_1+d} \begin{Bmatrix} h_l^{(1)}(kr) \\ j_l(kr) \end{Bmatrix} w_{l'}(kr)r^2dr. \tag{2.8}$$

It can be seen that such a surface current source generates only the same TE multipole.

From here on we will consider $r$ that is inside and the calculations for $r$ outside readily follow, namely $h_l^{(1)}(kr)$ should be replaced by $j_l(kr)$ in the expressions for the multipole strengths. To prove that TM multipoles are not generated by TE surface currents we perform several mathematical operations and arrive from Eq. (2.7) at

$$\begin{aligned}
a_E^{\text{inside}}(lm,l'm') &= \frac{k^2}{i\sqrt{l(1+1)}} \int Y_{lm}^* \left[c\rho\frac{\partial}{\partial r}\left[rh_l^{(1)}(kr)\right] + ik(\mathbf{r}\cdot\mathbf{J})h_l^{(1)}(kr)\right] drd\Omega \\
&= \frac{k^2}{i\sqrt{l(1+1)}}\frac{c}{i\omega}\left[\int\int_{r_1-\frac{dr}{2}}^{r_1+\frac{dr}{2}} \left\{\nabla\cdot\left[Y_{lm}^*\frac{\partial}{\partial r}\left[rh_l^{(1)}(kr)\right]\mathbf{J}\right] - \mathbf{J}\cdot\nabla\left[Y_{lm}^*\frac{\partial}{\partial r}\left[rh_l^{(1)}(kr)\right]\right]\right\} r^2drd\Omega \right. \\
&\quad \left. + \int\int_{r_1+d-\frac{dr}{2}}^{r_1+d+\frac{dr}{2}} \left\{\nabla\cdot\left[Y_{lm}^*\frac{\partial}{\partial r}\left[rh_l^{(1)}(kr)\right]\mathbf{J}\right] - \mathbf{J}\cdot\nabla\left[Y_{lm}^*\frac{\partial}{\partial r}\left[rh_l^{(1)}(kr)\right]\right]\right\} r^2drd\Omega\right] \\
&= -\frac{ck^2}{\omega\sqrt{l(1+1)}} \int Y_{lm}^* \left[\mathbf{J}_{\text{above upper}}\cdot\hat{\mathbf{r}}\left[\frac{\partial}{\partial r}\left(rh_l^{(1)}(kr)\right)\right]_{r_1+d}(r_1+d)^2 - \mathbf{J}_{\text{below upper}}\cdot\hat{\mathbf{r}}\left[\frac{\partial}{\partial r}\left(rh_l^{(1)}(kr)\right)\right]_{r_1+d}(r_1+d)^2 \right. \\
&\quad \left. + \mathbf{J}_{\text{above lower}}\cdot\hat{\mathbf{r}}\left[\frac{\partial}{\partial r}\left(rh_l^{(1)}(kr)\right)\right]_{r_1} r_1^2 - \mathbf{J}_{\text{below lower}}\cdot\hat{\mathbf{r}}\left[\frac{\partial}{\partial r}\left(rh_l^{(1)}(kr)\right)\right]_{r_1} r_1^2\right] d\Omega = 0,
\end{aligned} \tag{2.9}$$

where $\hat{\mathbf{r}} = \mathbf{r}/|\mathbf{r}|$, $\mathbf{r}\cdot\mathbf{J} \propto \mathbf{r}\cdot\mathbf{E}_{l'm'}^{(M)} = 0$, $\rho = \frac{\nabla\cdot\mathbf{J}}{i\omega}$, inside the volume $\nabla\cdot\mathbf{J} = 0$ since $\mathbf{J} \propto \theta_1(r)\mathbf{E}_{l'm'}^{(M)}$, $\psi\nabla\cdot\mathbf{J} = \nabla\cdot(\psi\mathbf{J}) - \mathbf{J}\cdot\nabla\psi$, $\psi \equiv Y_{lm}^*\frac{\partial}{\partial r}[rh_l^{(1)}(kr)]$, the volume integrals over the interfaces transform to surface integrals using divergence theorem. "Upper" and "lower" denote the upper and lower interface, respectively, "above" and "below" stand for above and below an interface, $\mathbf{J}_{\text{above upper}} = \mathbf{J}_{\text{below lower}} = 0$, and $\mathbf{J}_{\text{below upper}}\cdot\hat{\mathbf{r}} = \mathbf{J}_{\text{above lower}}\cdot\hat{\mathbf{r}} = 0$. Also, the contribution of the $\mathbf{J}\cdot\nabla[Y_{lm}^*\frac{\partial}{\partial r}[rh_l^{(1)}(kr)]]$ terms in the volume integration over the interfaces is negligible since the interface thickness is infinitesimal and the function is finite there.

We define $\tilde{J}_\theta = \frac{J_\theta}{w_{l'}(kr)}, \tilde{J}_\phi = \frac{J_\phi}{w_{l'}(kr)}$ and since $J_r = 0$ we express $\nabla\cdot\mathbf{J}$ inside the volume as follows:

$$\nabla\cdot\mathbf{J} = \frac{1}{r\sin\theta}\left[\frac{\partial}{\partial\theta}(\sin\theta J_\theta) + \frac{\partial J_\phi}{\partial\phi}\right] = \frac{w_{l'}(kr)}{r\sin\theta}\left[\frac{\partial}{\partial\theta}(\sin\theta\tilde{J}_\theta) + \frac{\partial\tilde{J}_\phi}{\partial\phi}\right] = 0. \tag{2.10}$$

We get that since $\frac{\partial}{\partial\theta}(\sin\theta\tilde{J}_\theta) + \frac{\partial\tilde{J}_\phi}{\partial\phi} = 0$, the current satisfies $\nabla\cdot\mathbf{J} = 0$ independently of the form of $w_{l'}(kr)$. Here, too, $w_{l'}(kr)$ is not required to be a spherical Bessel function.

Similarly, substituting a spherical layer source proportional to a TM multipole

$$\mathbf{J} = \frac{i}{k}J_0\theta_1(r)\nabla\times f_{l'}(kr)\mathbf{L}Y_{l'm'}(\theta,\phi) \propto \theta_1(r)\mathbf{E}_{l'm'}^{(E)} \propto \theta_1(r)\frac{i}{k}\nabla\times\mathbf{H}_{l'm'}^{(E)}, \tag{2.11}$$

we obtain

$$\begin{aligned}
a_E^{\text{inside}}(lm,l'm') &= \frac{k^2}{i\sqrt{l(1+1)}} \int Y_{lm}^* \left[c\rho\frac{\partial}{\partial r}\left[rh_l^{(1)}(kr)\right] + i\,J_0l'(l'+1)f_{l'}(kr)Y_{l'm'}h_l^{(1)}(kr)d^3x\right] \\
&= \frac{k^2}{i\sqrt{l(1+1)}} \int Y_{lm}^* \left\{-\frac{c}{i\omega}\mathbf{J}(r_1+d,\theta,\phi)\cdot\hat{\mathbf{r}}\left[\frac{\partial}{\partial r}\left(rh_l^{(1)}(kr)\right)\right]_{r_1+d}(r_1+d)^2 \right. \\
&\quad \left. + \frac{c}{i\omega}\mathbf{J}(r_1,\theta,\phi)\cdot\hat{\mathbf{r}}\left[\frac{\partial}{\partial r}\left(rh_l^{(1)}(kr)\right)\right]_{r_1} r_1^2 + i\,J_0l'(l'+1)f_{l'}(kr)Y_{l'm'}h_l^{(1)}(kr)r^2dr\right\} d\Omega
\end{aligned}$$

$$= J_0 k\sqrt{l(1+1)}\delta_{ll'}\delta_{mm'}\left\{\frac{c}{\omega}\frac{f_{l'}(k(r_1+d))}{(r_1+d)}\left[\frac{\partial}{\partial r}\left(rh_l^{(1)}(kr)\right)\right]_{r_1+d}(r_1+d)^2\right.$$
$$\left.-\frac{c}{\omega}\frac{f_{l'}(kr_1)}{r_1}\left[\frac{\partial}{\partial r}\left(rh_l^{(1)}(kr)\right)\right]_{r_1}r_1^2+k\int_{r_1}^{r_1+d}f_{l'}(kr)h_l^{(1)}(kr)r^2dr\right\}, \quad (2.12)$$

where we have used $\mathbf{r}\cdot\mathbf{J} = J_0\frac{l'(l'+1)}{k}f_{l'}(kr)Y_{l'm'} \propto \mathbf{r}\cdot\mathbf{E}^{(E)}_{l'm'}$ for $\mathbf{r}\cdot\mathbf{J}$, $\mathbf{J}(r_1+d,\theta,\phi)\cdot\hat{\mathbf{r}}$, and $\mathbf{J}(r_1,\theta,\phi)\cdot\hat{\mathbf{r}}$, the orthogonality property of the $Y_{lm}$s, and $\nabla\cdot\mathbf{J}=0$ inside the current volume since $\mathbf{J}\propto\mathbf{E}^{(E)}_{l'm'}$. Since for every vector $\nabla\cdot\nabla\times\mathbf{A}=0$, it is easy to see from the definition of the TM multipole that we can replace $f_{l'}(kr)$ with any $r$-dependent function and the derivation above still holds.

To prove that a TM surface current does not generate TE multipoles we write

$$\alpha_M^{\text{inside}}(lm,l'm') = \frac{-k^2}{\sqrt{l(1+1)}}\int h_l^{(1)}(kr)Y^*_{lm}(\theta,\phi)\mathbf{L}\cdot\frac{i}{k}J_0\theta_1(r)\nabla\times[f_{l'}(kr)\mathbf{L}Y_{l'm'}(\theta,\phi)]d^3x = 0, \quad (2.13)$$

where we have used

$$\mathbf{L} = \frac{1}{i}(\mathbf{r}\times\nabla),$$
$$(\mathbf{r}\times\nabla)\cdot\nabla\times[f_{l'}(kr)\mathbf{L}Y_{l'm'}(\theta,\phi)]$$
$$= \mathbf{r}\cdot\nabla\times\{\nabla\times[f_{l'}(kr)\mathbf{L}Y_{l'm'}(\theta,\phi)]\}$$
$$= -\mathbf{r}\cdot[k^2 f_{l'}(kr)\mathbf{L}Y_{l'm'}(\theta,\phi)] = 0,$$

since $\nabla\cdot\mathbf{E}^{(E)}_{l'm'}=0, \nabla^2\mathbf{E}^{(E)}_{l'm'} = -k^2\mathbf{E}^{(E)}_{l'm'}$, and since $\mathbf{L}$ does not operate on $r$. Here, too, a surface current source that is proportional to a TM multipole generates only the same multipole. Clearly, the results for the strengths of the multipoles are also valid for a spherical current layer that is thick and for a sphere, where we are interested in $\alpha_M^{\text{outside}}(l,m), \alpha_E^{\text{outside}}(l,m)$.

## III. MULTIPOLE FIELDS NEAR THE ORIGIN AND IN THE FAR FIELD

We calculated the $l=1,m=0$ and the $l=2,m=0$ TM and TE multipole fields which can be generated by the corresponding spherical current layers. We first calculated the $l=1,m=0$, and the $l=2,m=0$ TM multipole fields with $f_l(kr)\equiv j_l(kr)$ using the following relations [12]

$$\nabla\times\mathbf{L} = \mathbf{r}\nabla^2-\nabla, \quad L_x = \tfrac{1}{2}(L_+ + L_-),$$
$$L_y = \frac{1}{2i}(L_+ - L_-), \quad L_z = mY_{lm},$$
$$L_+Y_{l,m} = \sqrt{(l-m)(l+m+1)}Y_{l,m+1},$$
$$L_-Y_{l,m} = \sqrt{(l+m)(l-m+1)}Y_{l,m-1}. \quad (3.1)$$

In Fig. 1 we present $|\mathbf{E}|^2$ of the $l=1,m=0$ TM multipole as a function of $y$ and $z$ near the origin. The electric field of this multipole is concentrated at the origin and has a FWHM of $0.4\lambda$ in the $y$ axis (and in the $x$ axis) and $0.58\lambda$ in the $z$ axis. Note that while to first order $j_{l=1}(kr)\simeq(kr)/3$, upon operating with $\nabla\times$ on $j_{l=1}(kr)\mathbf{L}Y_{lm}$ in the calculation of $\mathbf{E}^{(E)}_{l=1,m}$, the field does not vanish at the origin. In Fig. 2 we present $|\mathbf{E}|^2$ of the $l=2,m=0$ TM multipole. This multipole has two focal spots at $z=\pm0.4\lambda$ with focal width of approximately $0.4\lambda$.

We then calculated $|\mathbf{E}|^2$ of the $l=1,m=0$ and $l=2,m=0$ TE multipoles with $g_l(kr)\equiv j_l(kr)$ by using the relation $L^2 = l(1+1)$ and obtained

$$|\mathbf{E}_{\text{TE}\,1,0}|^2 = \frac{3}{8\pi}[j_1(kr)]^2\sin^2\theta,$$
$$|\mathbf{E}_{\text{TE}\,2,0}|^2 = \frac{15}{8\pi}[j_2(kr)]^2\sin^2\theta\cos^2\theta. \quad (3.2)$$

In Fig. 3 we present $|\mathbf{E}|^2$ of the $l=1,m=0$ TE multipole as a function of $y$ and $z$ near the origin. The intensity of this multipole is concentrated in a toruslike shape. In Fig. 4 we present $|\mathbf{E}|^2$ of the $l=2,m=0$ TE multipole. The intensity of this multipole is concentrated in two toruslike shapes situated at $z=\pm0.4\lambda$.

From the derivations in Sec. II it is clear that placing currents that are modulated according to the $l=1,m=0$ TE and TM multipoles inside a sphere near the origin generates the electric field of these modes in space. Thus, electric fields whose intensities are presented in Figs. 1 and 3, are prescriptions for the current distributions required to generate the $l=1,m=0$ TM and TE multipoles respectively. The $l=1,m=0$ TM multipole field in a very small sphere corresponds to an oscillating point dipole. In addition, the focal spot of this mode is similar to the current distribution of a $\lambda/2$ antenna, which has a dominant $l=1,m=0$ TM component in its radiation field pattern. The $l=1,m=0$ TE multipole field is similar to a current loop distribution.

In addition, a multipole current source at the origin and a spherical layer centered at the origin can be coupled. The

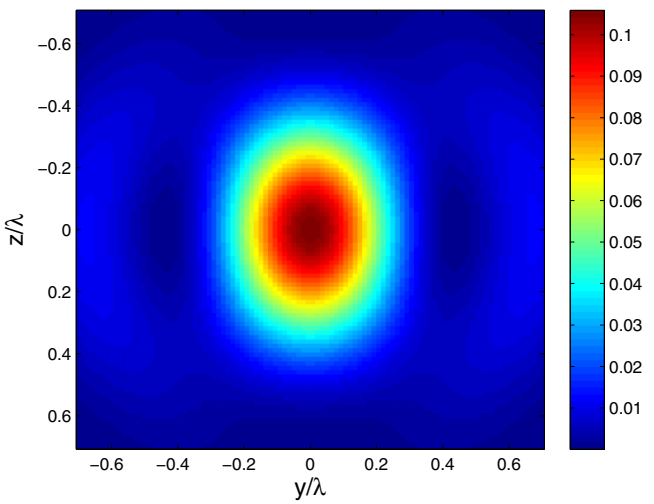


FIG. 1. $|\mathbf{E}|^2$ of a TM $l=1,m=0$ multipole.

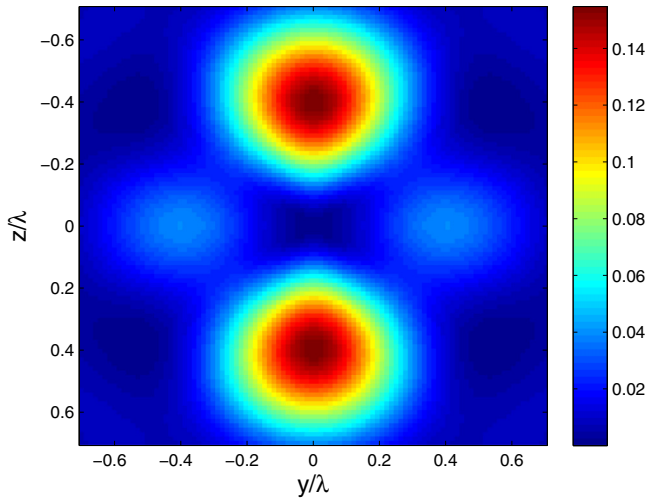


FIG. 2. $|\mathbf{E}|^2$ of a TM $l = 2, m = 0$ multipole.

radiation emitted from the multipole source impinges on the spherical layer, which in turn is polarized and emits radiation both inside and outside that layer. The radiation inside impinges on the current source and can reexcite the same radiation pattern, etc. The polarizable spherical layer is characterized by an $\epsilon$ value and can be either a dielectric or a metal. The polarization pattern in the spherical layer originates from the radiation field pattern of the current source and there is no need to design an optical antenna distribution inside the layer. This can be analyzed quantitatively by expanding the field generated by an electromagnetic multipole using the spherical layer eigenstates. Since the overlap integrals will be nonzero only for the corresponding multipole eigenstates, only this term will be employed in the expansion and the combined field can be readily calculated. The magnitude of the scattered field becomes larger as $s \equiv 1/u$ approaches the multipole eigenvalue $s_n \equiv 1/u_n$ (see Refs. [1,2]). In the quasistatic expansion the permittivity eigenvalues are real and can be approached with realizable materials. In the electromagnetic expansion the permittivity eigenvalues usually

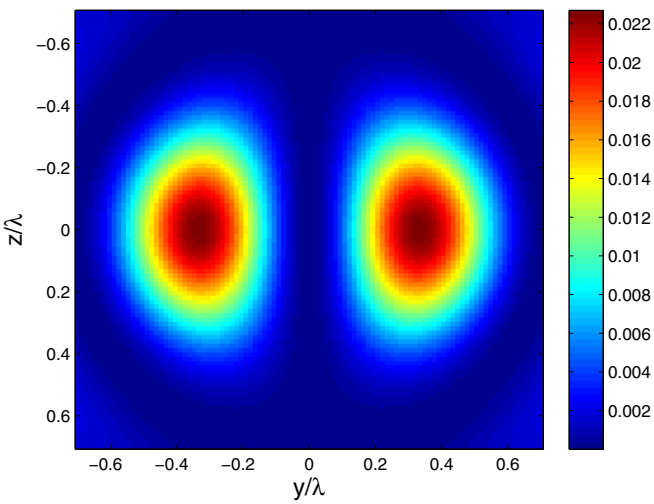


FIG. 3. $|\mathbf{E}|^2$ of a TE $l = 1, m = 0$ multipole.

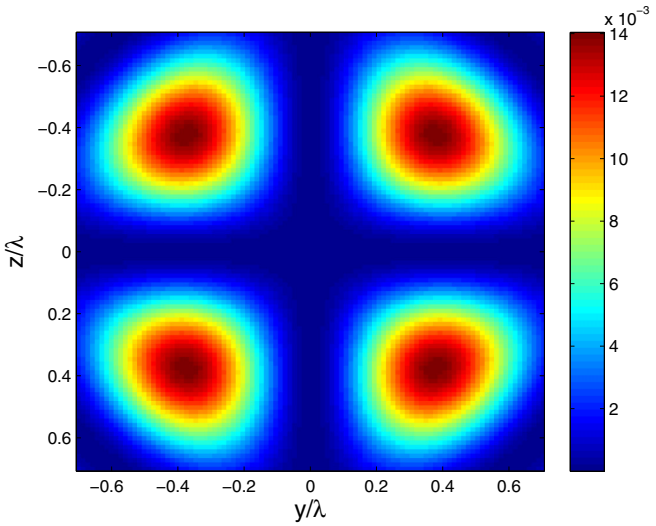


FIG. 4. $|\mathbf{E}|^2$ of a TE $l = 2, m = 0$ multipole.

have gain but in some cases they are also close to real [2]. Similarly if a polarizable spherical layer or a sphere is excited with a given multipole it will couple to another sphere or spherical layer centered at the origin for the reason mentioned above.

In the radiation zone we can write $\mathbf{E}_{lm}^{(M)} = \mathbf{H}_{lm}^{(M)} \times \mathbf{n}$. For a source that consists of a complete set of TE multipoles with the order $l$ all having the same strength $a_M(l)$, the time-averaged power radiated per solid angle is

$$\frac{dP}{d\Omega} = \frac{1}{2k^2}|a_M(l)|^2 \left| \sum_m (-1)^{i+1} \mathbf{X}_{lm} \right|^2, \tag{3.3}$$

which becomes for incoherent sources [12]

$$\frac{dP}{d\Omega} = \frac{1}{2k^2}|a_M(l)|^2 \frac{2l+1}{4\pi}. \tag{3.4}$$

Thus, generating such a set of incoherent TE multipoles will result in isotropic radiation, where the simplest configuration comprises the multipoles $\mathbf{X}_{10}, \mathbf{X}_{1,-1}, \mathbf{X}_{1,1}$.

## IV. DISCUSSION

We showed that a spherical layer or a sphere with currents that are proportional to an electromagnetic multipole field can generate the same multipole field. We calculated the first TE and TM multipole fields and presented results near the origin and in the far field. The intensity of the $l = 1, m = 0$ TM multipole peaks at the origin with FWHM of $0.4\lambda$ in the lateral axes and $0.58\lambda$ in the vertical axis and the intensity of the $l = 1, m = 0$ TE multipole is concentrated in a toruslike shape. Currents proportional to a multipole field near the origin generate the multipole in space so the multipole fields are prescriptions for such current sources. A spherical layer can couple to a multipole source centered at the origin and enhance its radiation. For example, an oscillating point dipole or a molecule, which emits a TM $l = 1$ multipole, can couple to a spherical dielectric layer, similarly to a molecule in an optical cavity [6,7,10]. An $l = 1$ TE multipole near the origin also generates the same multipole field which can excite a spherical

layer that will drive the multipole currents near the origin. This analysis is valid also for the coupling between $l > 1$ TE and TM multipoles and a spherical layer. Finally, if a spherical layer or a sphere is excited with a given multipole it can be coupled to another concentric polarizable spherical layer or sphere.


[1] D. J. Bergman and D. Stroud, Phys. Rev. B **22**, 3527 (1980).

[2] A. Farhi and D. J. Bergman, Phys. Rev. A **93**, 063844 (2016).

[3] D. J. Bergman, Proc. of SPIE, Plasmonics: Metallic Nanostructures and Their Optical Properties V **6641**, 66411F (2007).

[4] L. Novotny and N. van Hulst, Nature Photon. **5**, 83 (2011).

[5] S. Orlov, U. Peschel, T. Bauer, and P. Banzer, Phys. Rev. A **85**, 063825 (2012).

[6] R. Chikkaraddy, B. de Nijs, F. Benz, S. J. Barrow, O. A. Scherman, E. Rosta, A. Demetriadou, P. Fox, O. Hess, and J. J. Baumberg, Nature (London) **535**, 127 (2016).

[7] J. Thompson, T. Tiecke, N. de Leon, J. Feist, A. Akimov, M. Gullans, A. Zibrov, V. Vuletić, and M. Lukin, Science **340**, 1202 (2013).

[8] B. van der Pol and H. Bremmer, Philos. Mag. **24**, 141 (1937).

[9] H. Chew, P. McNulty, and M. Kerker, Phys. Rev. A **13**, 396 (1976).

[10] J. Gersten and A. Nitzan, J. Chem. Phys. **95**, 686 (1991).

[11] H. Essén, Phys. Scr. **40**, 761 (1989).

[12] J. D. Jackson, *Electrodynamics, Third Edition* (Wiley Online Library, New York, 1998).

PHYSICAL REVIEW A **96**, 043806 (2017)

# Eigenstate expansion of the quasistatic electric field of a point charge in a spherical inclusion structure

Asaf Farhi* and David J. Bergman†

*Raymond and Beverly Sackler School of Physics and Astronomy, Faculty of Exact Sciences, Tel Aviv University, IL-69978 Tel Aviv, Israel*

(Received 20 June 2017; published 3 October 2017)

A point charge in the presence of a metallic nanosphere is a fundamental setup, which has implications for Raman scattering, enhancement of spontaneous emission of a molecule by an antenna, sensing, and modeling a metallic tip in proximity to a nanoparticle. Here we analytically expand the electric field of a point charge in an $\epsilon_2$ host medium in the presence of an $\epsilon_1$ sphere using the sphere eigenstates, where $\epsilon_1$ and $\epsilon_2$ can take any complex values. We develop a simple procedure to treat charge distribution, which results in a simple eigenstate expansion for the electric field of charge sources and is able to treat volume sources analytically. The electric field is strongly enhanced when $\epsilon_1/\epsilon_2$ is close to an $(\epsilon_1/\epsilon_2)_l$ eigenvalue of a dominant mode, which is determined by the point charge location and the measurement point. An electric field exists inside the sphere when $\epsilon_1/\epsilon_2$ is close to a $(\epsilon_1/\epsilon_2)_l$ resonance even when $\epsilon_1$ is a conductor. Low-order modes generate an electric field far away from the interface, where the $l = 1$ mode with a resonance at $\epsilon_1 = -2\epsilon_2$ generates a field at the sphere center. The high-order modes, which are associated with high spatial frequencies, become more dominant when the point charge approaches the sphere surface or when the physical parameters are close the high-order modes resonances. When $\epsilon_1/\epsilon_2$ is smaller or larger than the eigenvalues of the dominant modes, the modes interfere constructively and generate a strong signal at an angular direction equal to that of the source. The spectral information at the sphere surface may be utilized to calculate the point charge location without knowing its magnitude.

DOI: 10.1103/PhysRevA.96.043806

## I. INTRODUCTION

The electrostatic potential of a point charge in proximity to a conducting sphere was calculated analytically long ago [1]. This calculation assumes a constant potential on the sphere envelope and uses the method of images to construct a potential outside the sphere. The electrostatic potential of a point charge next to a dielectric sphere with vanishing conductivity was calculated by using solutions of Laplace's equation and matching boundary conditions of the electric field [2]. The electrodynamics of surface systems has been approached using a Green's function formalism in Ref. [3]. The electromagnetic field of an oscillating dipole outside a conducting sphere has been calculated by transforming an infinite series of spherical harmonics for the Hertzian vector into a more rapidly converging series [4]. In another study the electric field of an oscillating dipole inside a dielectric sphere was calculated by expanding the field in the vector spherical harmonics and matching the field boundary conditions [5]. Radiation emission rates for such a setup, where the dipole models a molecule, were calculated, taking into account electrostatic spherical and spheroidal cavity effects [6]. Asymptotic expressions for the potential and the field very close to an interface between an inclusion and a host medium in the limit $\epsilon_1 = -\epsilon_2$, both real, have also been obtained [7–10].

In the quasistatic regime, which occurs when the typical lengths of the system are much shorter than the wavelength, Maxwell's equations reduce to Poisson's equation with a complex and frequency-dependent permittivity $\epsilon(\omega)$. To account for a nonlocal conductivity and permittivity, $\epsilon(\omega)$ should be expressed as a tensor that depends also on the wave vector $\mathbf{k}$ [1]. Metals at optical frequencies can be described using an only $\omega$-dependent permittivity and we therefore assume this dependence in our derivations. To investigate a composite system with a source in the quasistatic regime, a point charge is often used to observe its properties. Scattering eigenstates of Maxwell's equations have been exploited to calculate the electric field in electrostatics [11–15] and in electrodynamics [16,17]. Recently, a procedure to treat current sources using the electromagnetic spectral expansion has been introduced [17].

Here we introduce a procedure to treat charge sources using the electrostatic eigenstate expansion. Such a procedure results in a simple eigenstate expansion for the electric field of charge sources and is able to treat volume sources analytically. In addition, we show that when the system is close to a resonance a strong electric field exists inside the sphere even if it is a conductor.

Potential applications are enhancement of spontaneous emission of a molecule by an antenna [18] in the quasistatic regime, modeling a tip in proximity to a metallic nanosphere, near-field imaging, sensing, and Raman spectroscopy. In particular, enhancement of Raman scattering and spontaneous emission of a molecule become more dominant when the field intensity at the molecule is higher, which can be obtained when the system is close to a resonance. Near-field imaging exploits evanescent waves to generate an image with resolution that is better than the diffraction limit. In this technique a two-dimensional image is generated by scanning the surface with a scattering tip. We show that the spectral information of the electric field can be utilized to calculate the point charge location when it is not at the sphere surface, which we define as the detector.

In Sec. II we present the theory and introduce a procedure to treat charge sources. In Sec. III we describe how we can

*asaffarhi@post.tau.ac.il
†bergman@post.tau.ac.il

 

obtain the point charge location from the spectral content of the electric field on the sphere surface. In Sec. IV we present the potential and the electric field for permittivity values that are close to the resonances of the dominant eigenstates. In Sec. V we discuss our results and potential applications.

## II. THEORY

In the quasistatic regime Maxwell's equations reduce to Poisson's equation with a complex and frequency-dependent permittivity

$$\nabla \cdot (\epsilon \nabla \psi) = -4\pi\rho. \tag{2.1}$$

By expressing the permittivity using the step functions $\theta_1$ and $\theta_2$ of the $\epsilon_1$ and $\epsilon_2$ media [$\theta_i(\mathbf{r}) = 1$ when $\epsilon(\mathbf{r}) = \epsilon_i$; otherwise $\theta_i(\mathbf{r}) = 0$] we write [11]

$$\begin{aligned} &\nabla \cdot [(\epsilon_1\theta_1 + \epsilon_2\theta_2)\nabla\psi] = -4\pi\rho, \\ &\nabla^2\psi = -4\pi\rho + u\nabla\cdot(\theta_1\nabla\psi), \quad u \equiv 1 - \frac{\epsilon_1}{\epsilon_2}. \end{aligned} \tag{2.2}$$

This is transformed to [11]

$$\psi = \psi_0 + u\Gamma\psi, \tag{2.3}$$

where

$$\begin{aligned} \Gamma\psi &= \int dV'\theta_1(\mathbf{r}')\nabla' G(\mathbf{r},\mathbf{r}')\cdot\nabla'\psi(\mathbf{r}'), \\ G &= \frac{1}{4\pi|\mathbf{r}-\mathbf{r}'|}, \quad \psi_0 = \frac{q}{\epsilon_2|\mathbf{r}-\mathbf{r}_0|}, \end{aligned} \tag{2.4}$$

and $\mathbf{r}_0$ is the point charge position, assumed to be in the $\epsilon_2$ medium.

The eigenstates satisfy Eq. (2.3) when there is no source, namely,

$$s_n\psi_n = \Gamma\psi_n, \quad \frac{1}{s_n} \equiv u_n = 1 - \frac{\epsilon_{1n}}{\epsilon_2}. \tag{2.5}$$

By defining the scalar product

$$\langle\psi|\phi\rangle \equiv \int dV\,\theta_1\nabla\psi^*\cdot\nabla\phi, \tag{2.6}$$

$\Gamma$ becomes a Hermitian operator and therefore it has a complete set of eigenstates. We insert the unity operator in Eq. (2.3) and arrive at

$$\psi = \psi_0 + \sum_n \frac{s_n}{s-s_n}\langle\psi_n|\psi_0\rangle\psi_n, \quad s \equiv 1/u, \tag{2.7}$$

where $\psi_n$ are the normalized eigenstates.

The sphere eigenstates are [11]

$$\psi_n \equiv \psi_{lm}(\mathbf{r}) = \frac{Y_{lm}(\Omega)}{(la)^{1/2}} \times \begin{cases} \left(\frac{r}{a}\right)^l, & r < a \\ \left(\frac{a}{r}\right)^{l+1}, & r > a, \end{cases} \tag{2.8}$$

where $a$ is the sphere radius, $Y_{lm}$ are the spherical harmonics, and the eigenvalues are

$$\epsilon_{1l} = -\epsilon_2\frac{l+1}{l}, \quad s_{lm} \equiv s_l = \frac{l}{2l+1}. \tag{2.9}$$

Clearly, in the $l \to \infty$ limit $s_l \to 1/2$. Thus, for a choice of $s \approx 1/2$ the high-order modes make a large contribution to the potential [11,12,15].

Note that the inclusion permittivity eigenvalues are real and on the order of magnitude of the host medium permittivity (with the opposite sign). In statics, the imaginary part of a metal permittivity is very high and it is impossible to approach the resonances. At high frequencies that imaginary part can become small and the resonances can be approached. In such a case, the physical electric field becomes very large due to a high contribution of one of the modes in the eigenstate expansion. The coefficient of an eigenstate $s_l^2/(s-s_l)$ can be expressed as

$$\frac{s_l^2}{s-s_l} = \frac{s_l^2/s}{1 - s_l(1-\epsilon_1/\epsilon_2)}$$

and becomes large when the real and imaginary parts of the denominator $1 - s_l(1-\epsilon_1/\epsilon_2)$ are small. Assuming $\mathrm{Im}(\epsilon_1), \mathrm{Im}(\epsilon_2) > 0$ and $\mathrm{Re}(\epsilon_1) < 0$, $\mathrm{Im}(\epsilon_1)$ and $\mathrm{Im}(\epsilon_2)$ are required to be small with respect to $|\epsilon_2|^2/\mathrm{Re}(\epsilon_2)$ and $|\epsilon_2|^2/|\mathrm{Re}(\epsilon_1)|$, respectively, in order for the imaginary part of the denominator to be small. When one of the constituents has gain [14] we can approach the condition for vanishing imaginary part of the denominator $\mathrm{Im}(\epsilon_1)/\mathrm{Im}(\epsilon_2) = \mathrm{Re}(\epsilon_1)/\mathrm{Re}(\epsilon_2)$.

Now we proceed to calculate the scalar product $\langle\psi_{lm}|\psi_0\rangle$. We exploit the fact that $\psi_0(\mathbf{r}) = 4\pi/\epsilon_2\int G(\mathbf{r},\mathbf{r}')\rho(\mathbf{r}')dV'$ and use Eq. (2.5) to obtain

$$\begin{aligned} \langle\psi_{lm}|\psi_0\rangle &= \frac{4\pi}{\epsilon_2}\int\int \theta_1\nabla\psi_{lm}^*\cdot\nabla G(\mathbf{r},\mathbf{r}')\rho(\mathbf{r}')dV'dV \\ &= \frac{4\pi}{\epsilon_2}s_l\int\psi_{lm}^*(\mathbf{r}')\rho(\mathbf{r}')dV' \\ &= \frac{4\pi q}{\epsilon_2}s_l\psi_{lm}^*(\mathbf{r}_0), \end{aligned} \tag{2.10}$$

where we assumed a point charge $\rho = q\delta^3(\mathbf{r}-\mathbf{r}_0)$. We finally get

$$\psi(\mathbf{r}) = \psi_0(\mathbf{r}) + \frac{4\pi q}{\epsilon_2}\sum_{l,m}\frac{s_l^2}{s-s_l}\psi_{lm}^*(\mathbf{r}_0)\psi_{lm}(\mathbf{r}). \tag{2.11}$$

It can readily be seen from Eqs. (2.8) and (2.11) that as the point charge approaches the sphere surface the contribution of the high-order modes becomes non-negligible [because $\psi_{lm}^*(\mathbf{r}_0)$ is larger] and they become more dominant in the expansion. In addition, low-order modes decay more slowly away from the interface and can therefore generate fields far away from the interface.

The ratio $\epsilon_1/\epsilon_2$ can be chosen to enhance a contribution to the electric field of one or more modes. We can therefore decompose each term in the sum in Eq. (2.11) into $(4\pi q/\epsilon_2)s_l^2\psi_{lm}^*(\mathbf{r}_0)\psi_{lm}(\mathbf{r})$, which does not depend on $s$, and $1/(s-s_l)$, which is determined by the distance between the physical $s$ and an eigenvalue $s_l$.

For a point charge at $\mathbf{r}_0 = z_0\hat{\mathbf{z}}$, $\psi_{lm}^*(\mathbf{r}_0) = \psi_{lm}(\mathbf{r}_0)$ and $\psi_{lm}(\mathbf{r}_0) \neq 0$ only when $m = 0$. Thus, $\psi(\mathbf{r})$ is independent of the azimuthal angle $\phi$ and the sum in Eq. (2.11) is considerably simplified. In addition, it can be seen that when the ratio $\epsilon_1/\epsilon_2$ is fixed, $\psi(\mathbf{r})/\psi_0(\mathbf{r})$ is also fixed since $s$ does not

change and $\epsilon_2$ cancels out. Therefore, the relative effect of a sphere inclusion on the potential and the electric field does not change when keeping this ratio fixed, even when $\epsilon_1$ is large. For example, the $l=1$ resonance occurs when $\epsilon_1 \approx -2\epsilon_2$. If $\mathrm{Re}(\epsilon_1) \approx -2\,\mathrm{Re}(\epsilon_2)$ and $\epsilon_1$ and $\epsilon_2$ have small dissipation we will be close to the resonance. When downscaling the system by a factor $b$ we get that $|\mathbf{E}|^2$ increases by a factor of $b^4$, as is the case for a point charge in a uniform medium.

To verify our result in Eq. (2.11) we placed a point charge at $\mathbf{r}_0 = z_0\hat{\mathbf{z}}$ ($z_0 > a$) and took the $\epsilon_1 \to \infty$ limit, assuming $\epsilon_2$ is finite. We then summed a geometric series to obtain the known textbook result for $\mathbf{r}$ on the $+z$ axis

$$\psi(\mathbf{r}) = \psi_0(\mathbf{r}) - \frac{qa/z_0}{|r - a^2/z_0|}. \tag{2.12}$$

We also took the limit of a point charge near a plane. Assuming $r \approx z_0 \approx a$ and defining $k \equiv l/a$ and $z \equiv r$ we obtained

$$\left(\frac{r}{a}\right)^l \quad r < a \approx e^{-k(a-z)}, \quad \left(\frac{a}{r}\right)^{l+1} \quad r > a \approx e^{-k(z-a)},$$
$$\left(\frac{a}{z_0}\right)^{l+1} \quad z_0 > a \approx e^{-k(z_0-a)}, \quad s_k \approx \frac{1}{2}(1 - e^{-2ka}). \tag{2.13}$$

From symmetry considerations one can obtain for the eigenstates dependence on the directions parallel to the plane $\psi_{\mathbf{k}}(\boldsymbol{\rho},z) = \exp(i\mathbf{k}\cdot\boldsymbol{\rho}) f_k(z)$, where $\boldsymbol{\rho}$ is the radial vector in cylindrical coordinates and $\mathbf{k} \equiv (k_x,k_y)$. In this limit the spectrum of eigenvalues is continuous and there is an accumulation point of the eigenvalues at $s = 1/2$ [11,12,15]. Note that the eigenstates can be normalized according to Eq. (2.6) due to their exponential dependence on the direction perpendicular to the plane.

The electric field can be written as

$$\mathbf{E}(\mathbf{r}) = -\nabla\psi_0(\mathbf{r}) - \mathbf{E}_{\mathrm{scat}}, \tag{2.14}$$

where

$$\mathbf{E}_{\mathrm{scat}} \equiv -\frac{4\pi q}{\epsilon_2}\sum_l \frac{s_l^2}{s - s_l}\psi^*_{lm}(\mathbf{r}_0)\nabla\psi_{lm}(\mathbf{r}); \quad \nabla\psi_{lm}(\mathbf{r}) = \mathbf{e}_r Y_{lm}\frac{\partial f_l(r)}{\partial r} + \mathbf{e}_\phi \frac{f_l(r)}{r\sin\theta} im Y_{lm} + \mathbf{e}_\theta \frac{f_l(r)}{r}\frac{\partial Y_{l,m}}{\partial\theta};$$

$$f_l(r) = \frac{1}{(la)^{1/2}} \times \begin{cases} \left(\frac{r}{a}\right)^l, & r < a \\ \left(\frac{a}{r}\right)^{l+1}, & r > a; \end{cases} \quad \frac{\partial f_l(r)}{\partial r} = \frac{1}{(la)^{1/2}} \times \begin{cases} l\left(\frac{r}{a}\right)^l \frac{1}{r}, & r < a \\ -(l+1)\left(\frac{a}{r}\right)^{l+1}\frac{1}{r}, & r > a; \end{cases} \tag{2.15}$$

and where $\partial\psi_{lm}/\partial\theta$ can be written as [19]

$$\frac{\partial\psi_{lm}}{\partial\theta} = \mathbf{e}_\theta \frac{f_l(r)}{r\sin\theta}\left[\frac{l(l+1)}{[(2l+1)(2l+3)]^{1/2}}Y_{l+1,m} - \frac{l(l-1)}{[(2l-1)(2l+1)]^{1/2}}Y_{l-1,m}\right]. \tag{2.16}$$

Note also that the field of the $l=1$ mode does not vanish at the origin and extends far from the sphere surface. In addition, the spherical harmonics satisfy $Y_{l,m=0}(\theta=0) = 1$ and $Y_{l,m=0}(\theta=\pi) = \pm 1$. Hence, when $s$ is very close to a resonance a dominant mode is excited and the intensity peaks at both $\theta = 0$ and $\theta = \pi$. The $l$ components $E_{\mathrm{scat},r,l}$ at $\theta = 0$ have a positive sign for $s_l < s$ and a negative sign for $s_l > s$. In addition, $Y_{l,m=0}$ and $Y_{l+1,m=0}$ at $\theta = \pi$ have opposite signs, but at the transition between $s_{l'} < s$ and $s_{l'+1} > s$, $E_{\mathrm{scat},r,l'}$ and $E_{\mathrm{scat},r,l'+1}$ have the same sign because the coefficient $1/(s - s_l)$ also changes sign. Thus, when $s \approx (s_{l'} + s_{l'+1})/2$ the dominant $l'$ and $l'+1$ modes will interfere destructively at $\theta = 0$ and constructively at $\theta = \pi$. When $s < s_l$ for every $l$ ($s < 1/3$), which corresponds to $\epsilon_1 \gtrsim -2\epsilon_2$, all $E_{\mathrm{scat},r,l}$ at $\theta = 0$ have the same sign and they interfere constructively to generate a strong signal. In this case the low-order modes that extend far from the sphere surface are strongly enhanced. Similarly, when $s > s_l$ for every $l$ ($s > 1/2$), which corresponds to $\epsilon_1 \lesssim -\epsilon_2$, all $E_{\mathrm{scat},r,l}$ at $\theta = 0$ interfere constructively and a strong signal is expected there. In this case the high-order modes that are associated with high spatial frequencies are strongly enhanced. When $s > s_l$ or $s < s_l$ for every $l$ the signs of $E_{\mathrm{scat},r,l}$ alternate at $\theta = \pi$ and a relatively weak signal is expected there.

## III. CALCULATING THE POINT CHARGE LOCATION FROM THE SPECTRAL CONTENT OF THE ELECTRIC FIELD

In the far field, a point in the object is mapped into a point in the image due to constructive interference, enabling 3D imaging. Near-field imaging exploits evanescent waves and achieves resolutions better than the diffraction limit. However, measuring an electric field in the near-field region produced by a point source that is not very close to the detector is usually difficult. This is since the modes decay exponentially with distance and since there can be orders of magnitude differences among electric-field intensities produced by point sources at different distances from the detector. When we are close to a resonance, the local physical field is enhanced and there is a significant field also due to point sources that are not very close to the detector (e.g., at the sphere surface). Thus, high-order components of the electric field can be detected. For a single point charge source, which we will treat as the object, the image field intensity will be maximal at an angular direction equal to that of the source and at the reflected direction with respect to the spherical surface (see Sec. II).

We start by calculating the field at the sphere surface and requiring full retrieval of an $l$ mode of the electric field. We expand $\psi_0$ inside the sphere, where there are no sources, using the unity operator. We then take the gradient of Eq. (2.14) to obtain the following expression for the electric field, which is valid inside the sphere:

$$\begin{aligned}\mathbf{E}_{\text{inside}} &= -\sum_{l,m=0}\left[\langle\psi_{lm}|\psi_0\rangle\nabla\psi_{lm}+\frac{s_l}{s-s_l}\langle\psi_{lm}|\psi_0\rangle\nabla\psi_{lm}\right]\\ &= -\sum_{l,m=0}\frac{s}{s-s_l}\langle\psi_{lm}|\psi_0\rangle\nabla\psi_{lm}. \end{aligned} \tag{3.1}$$

From this expression we calculate the electric field at $r=a^+$, i.e., just outside the sphere, using continuity conditions (note that the right-hand side is taken at $r=a^-$, not $r=a^+$)

$$\begin{aligned}&\mathbf{E}(r=a^+,\theta)\\ &\quad= -\sum_{l,m=0}\frac{s}{s-s_l}\langle\psi_{lm}|\psi_0\rangle\left(\frac{\epsilon_1}{\epsilon_2}\frac{\partial\psi_{lm}}{\partial r}\hat{\mathbf{r}}+\frac{1}{r}\frac{\partial\psi_{lm}}{\partial\theta}\hat{\boldsymbol{\theta}}\right)_{r=a^-}.\end{aligned} \tag{3.2}$$

We measure the field at the sphere surface and require that the magnitude of a given field component will be of the same order of magnitude as this field component in near-field imaging so that it can be detected. In near-field imaging the field of an object placed in a uniform medium is measured approximately at the object location. We therefore require that an $l$ component measured at the sphere surface and an $l$ component of $\mathbf{E}_0=-\nabla\psi_0$ measured at the point charge location (each field component is finite) will be approximately equal in magnitude. For a point charge in the presence of a sphere we define $\mathbf{r}_0=z_0\hat{\mathbf{z}}$ as the point charge location and $\mathbf{r}=a^+\hat{\mathbf{z}}$ as the measurement point. For near-field imaging we define the point charge location as $\mathbf{r}_{0\,\text{near field}}=a^+\hat{\mathbf{z}}$ and the measurement point also at $\mathbf{r}=a^+\hat{\mathbf{z}}$ and write

$$\begin{aligned}&\frac{E_{r,l,\,\text{sphere setup}}(\mathbf{r}=a^+\hat{\mathbf{z}},\mathbf{r}_0=z_0\hat{\mathbf{z}})}{E_{r,l,\,\text{uniform medium}}(\mathbf{r}=a^+\hat{\mathbf{z}},\mathbf{r}_{0\,\text{near field}}=a^+\hat{\mathbf{z}})}\\ &\quad=\frac{\frac{\epsilon_2}{\epsilon_1}\frac{ss_l}{s-s_l}\psi_{lm}(\mathbf{r}_0=z_0\hat{\mathbf{z}})\frac{\partial\psi_{lm}}{\partial r}\Big|_{\mathbf{r}=a^-\hat{\mathbf{z}}}}{s_l\psi_{lm}(\mathbf{r}=a^+\hat{\mathbf{z}})\frac{\partial\psi_{lm}}{\partial r}\Big|_{\mathbf{r}=a^-\hat{\mathbf{z}}}}\\ &\quad=\frac{\epsilon_2}{\epsilon_1}\frac{s}{s-s_l}(a/z_0)^{l+1}\simeq 1,\end{aligned} \tag{3.3}$$

where we have used $E_{r,l}(\mathbf{r}=a^-\hat{\mathbf{z}})=E_{r,l}(\mathbf{r}=a^+\hat{\mathbf{z}})$ for a point charge in a uniform medium. Assuming $s\simeq 1/2$ and $s_l-s\simeq 0.0025$ we obtain

$$(a/z_0)^{l+1}\simeq 2(s_l-s)\simeq 0.005,$$

and for $l=10$ we get

$$z_0/a\simeq 1.62.$$

This means that if we assume $\epsilon_1\simeq-\epsilon_2$, $s-s_l\simeq(\epsilon_1-\epsilon_{1l})/4\epsilon_2$ and for $\epsilon_2=1.5$, $\epsilon_1-\epsilon_{1l}\simeq 0.015$, and $z_0/a\lesssim 1.62$, the $l=10$ mode magnitude is equal to or higher than its magnitude when measuring $\mathbf{E}_0$ at the point charge location. The angular half-width of this mode near $\theta=\pi$ calculated using the $l=10$ Legendre polynomial is 0.14 rad, which translates to 4 nm for a sphere with a radius of 30 nm.

We now calculate the point charge location using the spectral content of the electric field on the sphere surface. Our motivation for calculating the source location without knowing its magnitude $q$ is, for example, fluorescence in which the emission strength of the source can be unknown. The electric field at the sphere surface is composed of modes with magnitudes that depend on the point charge location. Thus, the spectral information of the electric field is affected by the point charge location. If $s\approxeq s_l$, the electric field is dominated by this $l$ mode. Alternatively, if the radial component of the electric field on the sphere surface can be measured then by using a spherical harmonics transform defined by

$$F(l,m)=\int E_r Y^*_{lm}d\Omega, \tag{3.4}$$

we can obtain the spectral content of an $l,m$ mode in the expansion of the physical electric field. Note that this transform gives the spectral content since $\int Y_{l'm'}Y^*_{lm}d\Omega=\delta_{ll'}\delta_{mm'}$ and $E_{r,lm}$ has a $Y_{l,m}$ associated with it. To perform the transform we need to choose the coordinate system so that $\theta=0$ points to the point charge location. Since the maximal intensity is always at $\theta=0,\pi$ we must choose between them to define $\theta=0$ according to the $s$ value (see discussion above) or by knowing in which half space the point charge is located. The ratio between the magnitudes of the $l_1$ and $l_2$ components of the electric field of a point charge located at $\mathbf{r}_0=z_0\hat{\mathbf{z}}$ is

$$\frac{F(l_1,m=0)}{F(l_2,m=0)}=\frac{l_1+1}{l_2+1}\frac{l_2}{l_1}\frac{s_{l_1}}{s_{l_2}}\frac{s-s_{l_2}}{s-s_{l_1}}a^{l_1-l_2}z_0^{l_2-l_1}. \tag{3.5}$$

Thus, from this ratio we can calculate the point charge location $z_0$ without knowing its magnitude. Now using $z_0$, it is straightforward to calculate $q$ from any $F(l,m)$ component. In order for the $l$ mode fields of two point charges $q_1$ and $q_2$ located at $z_{01}\hat{\mathbf{z}}$ and $z_{02}\hat{\mathbf{z}}$, respectively, to be comparable in magnitude we can require $0.1\lesssim(q_1/q_2)(z_{02}/z_{01})^{l+1}\lesssim 10$. For example, for the $l=10$ mode assuming $q_1=q_2$ we obtain that for comparable field intensities we must have $0.9\lesssim z_{01}/z_{02}\lesssim 1.11$. Thus, objects in a range of 3 nm along $r$ for a sphere with a radius of 30 nm produce comparable field intensities at the sphere surface.

It should be noted that measuring the electric field on the whole sphere is possible only if the detector has a negligible effect on the incoming field at all the measurement points. When the detector is situated on the half sphere that is closer to the source it will be on the path of the incoming field and may interfere with the field. When $s\approx(s_l+s_{l+1})/2$ the field will peak at $\theta=\pi$ and the object location can be approximated using the field magnitude at the half sphere that is further away from the source. Also, measuring the field on the sphere surface necessitates 3D sampling (scanning the field with a detector in three axes), which is more challenging. This concept of transforming a field on a surface to the spectral plane may be adjusted to setups in which the required measurements are more suited for current experimental techniques. For example, in a setup of a flat slab and a source in a host medium [14,17], measuring the electric field at the slab surface that is further away from the source is both two dimensional and has a negligible effect on the measured field. In such a setup the

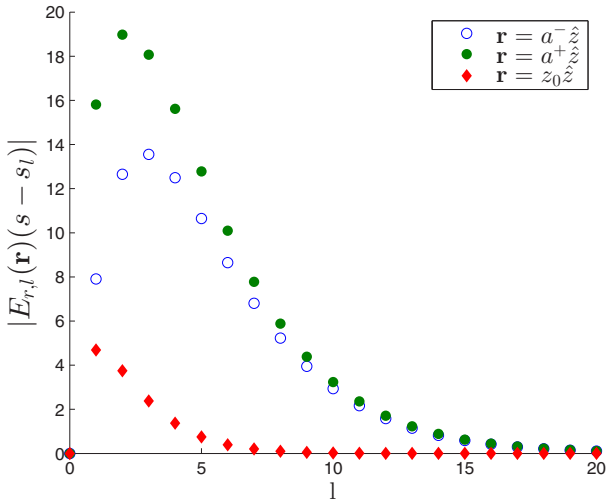


FIG. 1. Plot of $|E_{r,l}(\mathbf{r})(s - s_l)|$ at $\mathbf{r} = a^-\hat{\mathbf{z}}$ and $\mathbf{r} = a^+\hat{\mathbf{z}}$, i.e., just inside and just outside the sphere, and at $\mathbf{r} = z_0\hat{\mathbf{z}}$ as a function of $l$ for $\epsilon_2 = 1$, $z_0 = 1.5a$, and $a = 30$ nm.

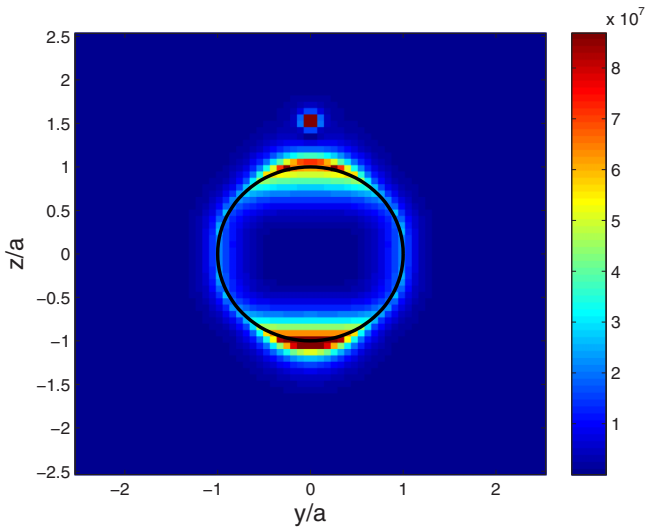


FIG. 2. Plot of $|\mathbf{E}|^2$ for a point charge at $z_0 = 1.5a$, $a = 30$ nm, $s = 0.43$, $\epsilon_2 = 1$, and $\epsilon_1 = -1.3256$.

perpendicular field component at the surface may be Hankel transformed [20] in order to retrieve the source location.

## IV. RESULTS

We first considered $\epsilon_2 = 1$ and a point charge located at $z_0 = 1.5a$, where $a = 30$ nm. In order to exclude the effect of the choice of physical $s$ on the results we decomposed each term in the sum in Eq. (2.14) into $(-4\pi q/\epsilon_2)s_l^2\psi^*_{lm}(\mathbf{r}_0)\nabla\psi_{lm}(\mathbf{r})$, which does not depend on the choice of $s$, and $1/(s - s_l)$. The size of the last factor is determined by the difference between the physical $s$ and the eigenvalue $s_l$. We calculated

$$|E_{r,l}(\mathbf{r})(s - s_l)| = \left|\frac{4\pi q}{\epsilon_2}s_l^2\psi^*_{l,m=0}(\mathbf{r}_0)\frac{\partial\psi_{l,m=0}(\mathbf{r})}{\partial r}\right| \quad (4.1)$$

at $\mathbf{r} = a^-\hat{\mathbf{z}}$, i.e., just inside the sphere, up to $l = 20$. Note that the spectral components of $\mathbf{E}_0 = -\nabla\psi_0$ can be included in the calculation of $E_{r,l}(\mathbf{r})$ both inside the sphere and at the sphere surface. We found that the $l = 3$ mode with $s_l = 0.4286$ and $\epsilon_{1,l=3} = -4/3$ is the most dominant one. In Fig. 1 we present the results as a function of $l$.

We then chose $\epsilon_1 = -1.3256$ and $s = 0.43$, which are close to the $l = 3$ mode resonance. We calculated the electric field for these $s$ and $\epsilon_1$ values. The calculation of the electric field was performed analytically using Eq. (2.15). In Fig. 2 we present the intensity of the electric field.

It can be seen that the electric field is significantly enhanced with maximal intensity at the interface between the sphere and the host medium at $\theta = 0,\pi$.

We also calculated $|E_{r,l}(\mathbf{r})(s - s_l)|$ at $\mathbf{r} = a^+\hat{\mathbf{z}}$, i.e., just outside the sphere, and at the point charge location $\mathbf{r} = 1.5a\hat{\mathbf{z}}$ (see Fig. 1). The field intensity at the point charge location is relevant for phenomena such as enhancement of spontaneous emission of a molecule by an antenna and Raman spectroscopy, which become more dominant as the intensity at the molecule increases. The most dominant modes at $\mathbf{r} = a^+\hat{\mathbf{z}}$ and at the point charge location $\mathbf{r} = 1.5a\hat{\mathbf{z}}$ are $l = 2$ and $l = 1$, respectively. The contributions to the electric field inside and outside the sphere do not need to have the same $l$ dependence since continuity of $D_r$ for each mode is satisfied for the eigenvalue $\epsilon_{1l}$ but not for $\epsilon_1$.

We then calculated $|E_{r,l}(\mathbf{r})(s - s_l)|$ for $z_0 = 2a$. The most dominant modes of the electric field at $\mathbf{r} = a^-\hat{\mathbf{z}}$ and $\mathbf{r} = a^+\hat{\mathbf{z}}$ and at the point charge location $\mathbf{r} = 2a\hat{\mathbf{z}}$ were found to be $l = 2$, 1, and 1, respectively.

Then, for a point charge located at $\mathbf{r}_0 = 1.15a\hat{\mathbf{z}}$ we calculated $|E_{r,l}(\mathbf{r})(s - s_l)|$ at both $\mathbf{r} = a^-\hat{\mathbf{z}}$ and $\mathbf{r} = a^+\hat{\mathbf{z}}$ and at the point charge location $\mathbf{r} = 1.15a\hat{\mathbf{z}}$, and the most dominant modes were found to be $l = 8$, 7, and 3, respectively (see Fig. 3). Thus, as the point charge approaches the sphere interface the most dominant modes are of higher order, including for a measurement at the point charge location. These calculations necessitated 50 modes in the expansion. Here we were interested to excite high-order modes and compromise on intensity, which is high anyway. We therefore chose $s = 0.487$,

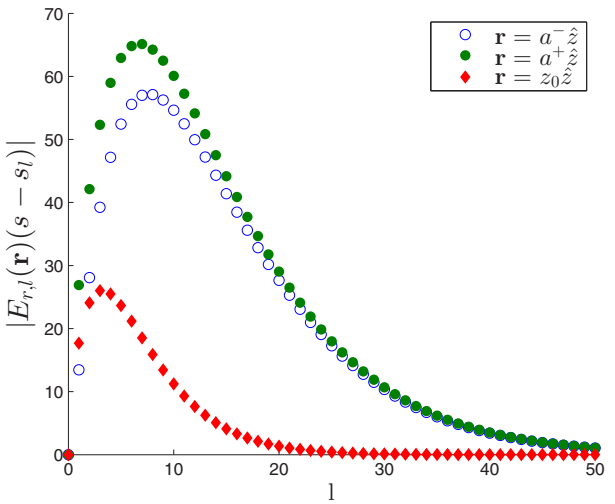


FIG. 3. Plot of $|E_{r,l}(\mathbf{r})(s - s_l)|$ at $\mathbf{r} = a\hat{\mathbf{z}}$ inside and outside the sphere and at $\mathbf{r} = z_0\hat{\mathbf{z}}$ as a function of $l$ for $\epsilon_2 = 1$, a point charge located at $z_0 = 1.15a$, and $a = 30$ nm.

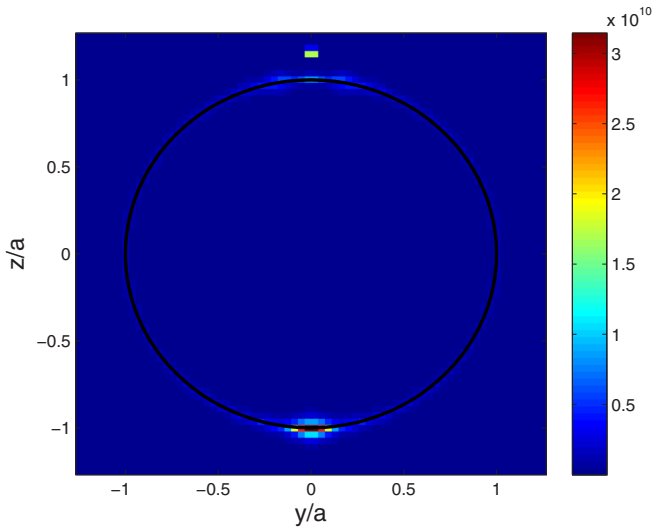


FIG. 4. Plot of $|\mathbf{E}|^2$ for a point charge at $z_0 = 1.15a$, $a = 30$ nm, $s = 0.487$, $\epsilon_2 = 1$, and $\epsilon_1 = -1.0534$.

which corresponds to $\epsilon_1 = -1.0534$ and is in between the $s_{l=19} = 0.4872$ and $s_{l=18} = 0.4865$ resonances. In Fig. 4 we present the electric-field intensity. It can be seen that the field intensity is greatly enhanced. In addition, the field is highly localized at $\theta = \pi$ with $\exp(-1/2)$ of the maximal intensity at $\simeq$2 nm from the maximum.

We were then interested in considering a system that is close the $l = 1$ resonance. The electric field of the $l = 1$ mode extends far from the interface and does not vanish at the origin. A resonance of this mode occurs when the material parameters satisfy $\epsilon_2 \approx -\epsilon_1/2$ and with small and positive $\mathrm{Im}(\epsilon_1)$ and $\mathrm{Im}(\epsilon_2)$ we can approach this resonance. Note that a resonance occurs when $s = s_l$ and the effect of approaching the resonance can be computed by calculating $s_l^2/(s - s_l)$ (see the discussion in Sec. II). We chose $\epsilon_1 = -3.38 + 0.192i$ (silver at 380 nm) and $\epsilon_2 = 1.69 + 0.08i$ and placed a point charge at $\mathbf{r}_0 = 2a\hat{\mathbf{z}}$. In Fig. 5 we present $|\mathbf{E}|^2$ in space. It can be seen that

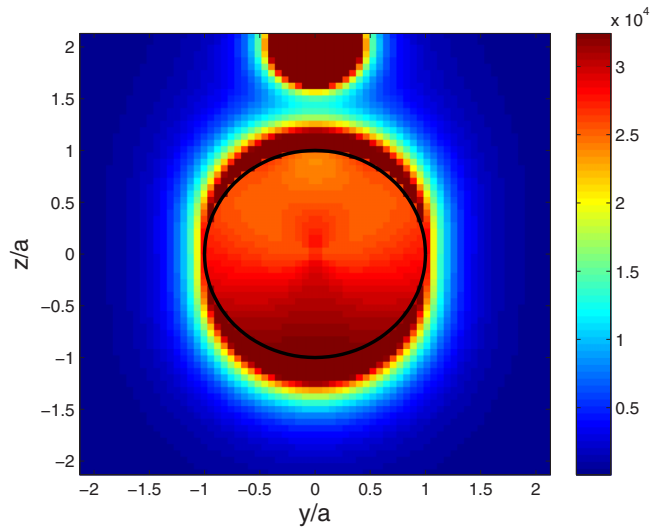


FIG. 5. Plot of $|\mathbf{E}|^2$ for a point charge at $z_0 = 2a$, $a = 30$ nm, $s = 1/3$, $\epsilon_2 = 1.69 + 0.08i$, and $\epsilon_1 = -3.38 + 0.192i$.

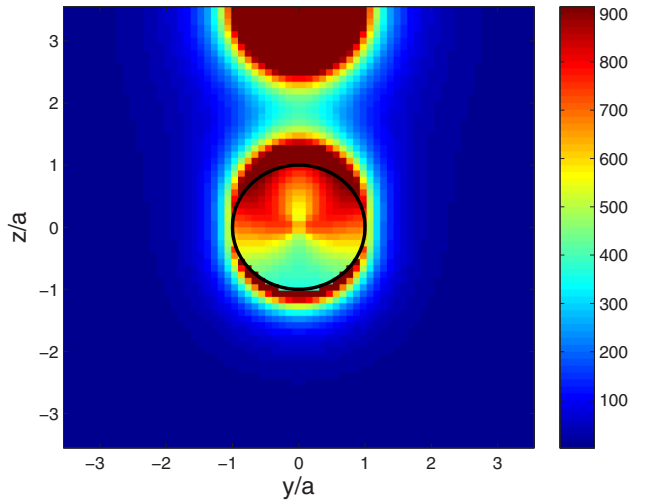


FIG. 6. Plot of $|\mathbf{E}|^2$ for a point charge at $z_0 = 3.5a$, $a = 30$ nm, $s = 0.3$, $\epsilon_2 = 1$, and $\epsilon_1 = -2.33$.

there is a strong electric field inside the sphere even though it is a conductor. Interestingly, water permittivity at 380 nm is $\epsilon_2 = 1.797 + 8.5 \times 10^{-9}$ and a strong electric field inside and outside the sphere is expected for a silver nanosphere immersed in water.

Finally, we calculated $|\mathbf{E}|^2$ for setups in which $s$ is smaller or larger than $s_l$ of all the dominant modes. In these setups the low- and high-order modes interfere constructively at $\theta = 0$. In Fig. 6 we present $|\mathbf{E}|^2$ for $z_0 = 3.5a$ and $s = 0.3$ ($\epsilon_2 = 1$ and $\epsilon_1 = -2.33$), which is smaller than all the eigenvalues $s_l$. It can be seen that the intensity is strong at $\theta = 0$ and that the electric field extends far from the sphere surface since $s$ is closer to $s_l$ of the low-order modes. In Fig. 7 we present $|\mathbf{E}|^2$ for $z_0 = 1.5a$ and $s = 0.492$ ($\epsilon_2 = 1$ and $\epsilon_1 = -1.0325$), which is larger than the eigenvalues $s_l$ of the dominant modes. The intensity is again strong at $\theta = 0$ and is spatially concentrated since $s$ is closer to $s_l$ of the high-order modes that are associated with high spatial frequencies.

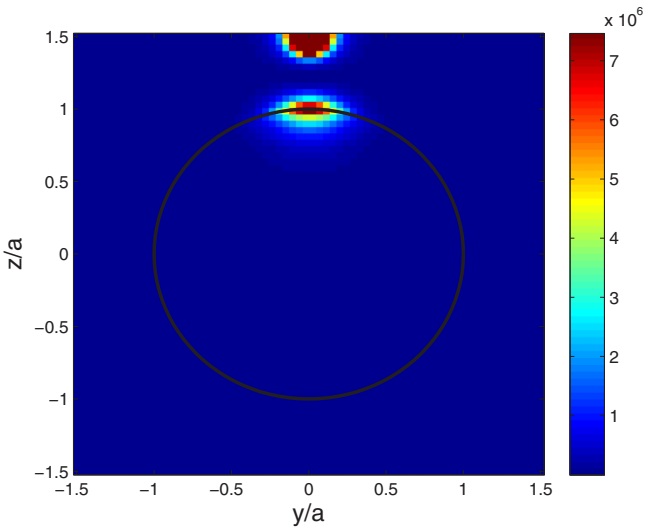


FIG. 7. Plot of $|\mathbf{E}|^2$ for a point charge at $z_0 = 1.5a$, $a = 30$ nm, $s = 0.492$, $\epsilon_2 = 1$, and $\epsilon_1 = -1.0325$.

To verify our results we checked the continuity of the physical $D_r$ at the interface. In the electric-field expansions $\mathbf{E}_0$ is continuous and all the eigenstates satisfy continuity of $D_r$ with their $\epsilon_{1l}$ eigenvalue. Thus, none of the terms in the expansion is expected to satisfy continuity of physical $D_r$ at the interface. Our calculations showed that the physical $D_r$ is continuous at the interface for various $s$ values to a high accuracy.

The calculations were performed using a grid of $70 \times 70$ on the $y$ and $z$ axes. In our calculations of the potential and the electric field in all space, the running times on a single core were $\sim$2, 3, and 8 s for $z_0 = 2a$, $1.5a$, and $1.15a$, respectively, which can be reduced by an order of magnitude with code optimization in MATLAB.

## V. DISCUSSION

We presented an analytic expansion of the potential and the electric field for a setup of an $\epsilon_1$ sphere embedded in an $\epsilon_2$ host medium, where the permittivity values of the sphere and the host medium can take any value. For a point charge on the $z$ axis at $z_0$ the expansion only includes the $m = 0$ terms and involves up to 20 terms when $z_0 \gtrsim 1.5a$. For a given charge location and measurement point a dominant mode can be readily identified and one can select a sphere permittivity value that is close to the mode resonance in order to obtain a significant enhancement of the electric field.

We placed a point charge at $z_0 = 1.5a$, $1.15a$, $2a$, and $3.5a$ and chose permittivity values that are close to a resonance. We observed very high enhancement of the electric field. Interestingly, a significant electric field can exist inside the sphere even if it is a conductor, when $\epsilon_1/\epsilon_2$ is close to $(\epsilon_1/\epsilon_2)_l$ of a dominant mode. The contribution of the high-order modes becomes non-negligible as the point charge approaches the sphere surface. The low-order modes decay more slowly and generate an electric field away from the surface. Very high resolution is obtained when a high-order mode is excited since high-order modes are associated with high spatial frequencies. When $s \approx (s_l + s_{l+1})/2$ the dominant $l$ and $l+1$ modes interfere constructively at $\theta = \pi$. When $\epsilon_1 \gtrsim -2\epsilon_2$, the radial field component of all the modes at $\theta = 0$ interfere constructively and generate a strong signal dominated by the low-order modes that extend far from the sphere surface. Similarly, when $\epsilon_1 \lesssim -\epsilon_2$ the radial field component of all the modes at $\theta = 0$ interfere constructively and a strong signal dominated by the high-order modes that are associated with high spatial frequencies is generated.

We showed that the spectral information at the sphere surface can be utilized to calculate the point charge location without knowing its magnitude. In addition, when the system is close to a resonance the high-order modes of the electric field can be retrieved. These may have relevance for near-field imaging of objects that are not at the surface. To assist in balancing the smaller magnitudes of evanescent waves from distant sources, the magnitude of the light sources can be larger for larger $r$, which can be achieved by back illumination. Gain can both enhance the incoming field and enable $s$ that is closer to the $s_l$ resonances that are real. Another possible mechanism to enable detection of high-order modes in the expansion of the electric field of a point charge that is not very close to the surface is to mediate them through resonant particles inside the medium that enhance them, similarly to the isolated sphere. Since we can calculate the point charge location for a single point charge, selectively exciting local points that radiate at different times may enable one to retrieve their locations too [21,22]. A similar analysis can be formulated for a setup of a flat slab in a host medium [14] where the spectrum of the eigenvalues is continuous.

Potential applications are enhancement of spontaneous emission of a molecule by an antenna [18], where the point charge and the sphere can model the molecule and the antenna, respectively, sensing, modeling a tip in proximity to a metallic nanosphere, near-field imaging, and Raman spectroscopy. Finally, since the expansion employs a small number of terms for a single point charge source, calculating the potential and the electric field in all space is very fast.


[1] J. D. Jackson, *Electrodynamics* (Wiley, New York, 1975).
[2] J. A. Stratton, *Electromagnetic Theory* (McGraw-Hill, New York, 1941).
[3] F. García-Moliner and F. Flores, *Introduction to the Theory of Solid Surfaces* (Cambridge University Press, Cambridge, 2009).
[4] B. van der Pol and H. Bremmer, Philos. Mag. **24**, 141 (1937).
[5] H. Chew, P. McNulty, and M. Kerker, Phys. Rev. A **13**, 396 (1976).
[6] J. Gersten and A. Nitzan, J. Chem. Phys. **95**, 686 (1991).
[7] N. A. Nicorovici, R. C. McPhedran, and G. W. Milton, Phys. Rev. B **49**, 8479 (1994).
[8] G. W. Milton, N.-A. P. Nicorovici, R. C. McPhedran, and V. A. Podolskiy, Proc. R. Soc. A **461**, 3999 (2005).
[9] G. W. Milton and N.-A. P. Nicorovici, Proc. R. Soc. A **462**, 3027 (2006).
[10] H. Kettunen, M. Lassas, and P. Ola, arXiv:1406.6224.
[11] D. J. Bergman, J. Phys. C **12**, 4947 (1979).
[12] D. J. Bergman, Phys. Rev. B **19**, 2359 (1979).
[13] D. J. Bergman, Phys. Rev. A **89**, 015801 (2014).
[14] A. Farhi and D. J. Bergman, Phys. Rev. A **90**, 013806 (2014).
[15] D. J. Bergman, in *Les Méthodes de l'Homogénéisation: Théorie et Applications en Physiques*, edited by R. Dautray (Editions Eyrolles, Paris, 1985), pp. 1–128.
[16] D. J. Bergman and D. Stroud, Phys. Rev. B **22**, 3527 (1980).
[17] A. Farhi and D. J. Bergman, Phys. Rev. A **93**, 063844 (2016).
[18] M. S. Eggleston, K. Messer, L. Zhang, E. Yablonovitch, and M. C. Wu, Proc. Natl. Acad. Sci. USA **112**, 1704 (2015).
[19] A. R. Edmonds, *Angular Momentum in Quantum Mechanics* (Princeton University Press, Princeton, 1957).
[20] R. N. Bracewell and R. N. Bracewell, *The Fourier Transform and its Applications* (McGraw-Hill, New York, 1986), Vol. 31999.
[21] J. Hanne, H. J. Falk, F. Görlitz, P. Hoyer, J. Engelhardt, S. J. Sahl, and S. W. Hell, Nat. Commun. **6**, 7127 (2015).
[22] M. Fernández-Suárez and A. Y. Ting, Nat. Rev. Mol. Cell Biol. **9**, 929 (2008).

# 3 Discussion

The PhD thesis consists of four projects. In the first project, we expanded the quasistatic electric field for a setup of a slab in a host medium and a point source using the structure eigenstates. In this expansion the permittivities of the two constituents $\epsilon_1$ and $\epsilon_2$ can take any complex values. We analyzed Veselago lens imaging for permittivity values satisfying $\epsilon_1 \approx -\epsilon_2$ and revealed that the optimal imaging is at the interface between the slab and the host medium. In the second project we expanded the electrodynamic field for the same structure with an oscillating dipole source. In this project the treatment of volume current sources was introduced to the eigenpermittivity formalism. In the third project, based on the relation between phased arrays and plane waves, we introduced the spherical analog of a phased array, which generates a vector spherical harmonic, and showed that it can be used to generate a focal spot eight times smaller in volume compared with the one generated by conventional lenses. Our fourth project was an eigenstate expansion of the quasistatic field for a spherical inclusion structure and a point charge source. In this project the treatment of charge density was introduced to the eigenpermittivity formalism. It was shown that a strong electric field can exist inside a sphere even though it is a conductor. In addition, a procedure to calculate the point charge location without knowing the charge magnitude was developed.

Our first result that the optimal imaging for Veselago-lens imaging in the near field is at the interface between the slab and the medium was surprising [16, 17]. Veselago lens imaging in the near field had been analyzed previously using geometric optics, with image locations derived accordingly. It was thus believed that since evanescent waves, which carry high spatial frequencies, are employed in the imaging, the imaging is both subwavelength and three dimensional (3D). We showed that this imaging can in fact have subwavelength resolution, but that the images are formed at the interface between the slab and the medium, rendering this imaging technique 2D, similarly to near field imaging. Evanescent waves, do not propagate according to geometric optics and do not accumulate phase in their propagation direction. They thus form an image in every plane perpendicular to the direction in which they decay, with a better resolution as higher spatial frequency modes are involved. Therefore, dominant evanescent modes result in enhanced resolution and 2D imaging while dominant propagating modes result in diffraction-limited resolution and 3D imaging. The slab setup with $\epsilon_1 \approx -\epsilon_2$ or $n_1 \approx -n_2$ is interesting in near field imaging since the slab amplifies evanescent waves and when the object is close to the slab surface very high spatial resolutions can be obtained, even exceeding the conventional near-field imaging resolutions. A procedure to perform 3D near-field imaging of a single source with an unknown magnitude was also developed [18].

The second result is the incorporation of charge and current volume sources into the eigenpermittivity formalism [17, 18]. Since a current can model a molecule and medium polarization, this extension is very important and enables analyzing many physical phenomena such as Purcell effect and nonlinear optics. Using the eigenpermittivity formalism analytic expansions of the elec-

tric field for a slab, sphere, and cylindrical inclusion in a host medium can be derived. Incorporating current sources thus results in analytic calculations for these setups with localized or volume sources. The fields of a localized source in the electrodynamic regime and volume sources in two-constituent media had not been previously derived analytically and this result can enable us to gain new insights in physical phenomena such as enhancement of spontaneous emission close to an antenna and nonlinear response of an inclusion. This result has already been applied in the calculation of the field generated by a current source for an inclusion with a general geometry using numerical COMSOL implementation [15]. These developments position the eigenpermittivity formalism as a state-of-the-art method for performing such calculations. This result can also be applied in setups of multiple inclusions, which are important for field localization [23] and designing metamaterials.

The third result is the spherical analog of a phased array, which generates a vector spherical harmonic field in space [24]. This points to a general relation - a current source modulated by a uniform medium eigenstate in a plane generates the same eigenstate in all space. The $l = 1$ TM vector spherical harmonics have a small focal spot at the origin and can be used in 3D imaging as the illumination source. Since the focal spot is small it can enable to image with better spatial resolution compared to conventional lenses. Moreover, since a VSH distribution is a prescription for the current distribution in a spherical volume or a spherical layer volume, which generates the VSH field in space, sources which generate VSH fields may be engineered. Interestingly, a source that consists of a complete set of incoherent TE multipoles with the order $l$ results in isotropic radiation and such radiation pattern may be designed. In addition, since a spherical layer or a sphere polarized according to a VSH generates a VSH field in space, it explains the coupling between such structures - they transfer the VSH field components back and fourth.

The fourth result is that when a source is in proximity to a spherical conductor embedded in a host medium, the electric field inside the conductor can be strongly enhanced even though it is in the quasistatic regime [18]. We showed that this effect indeed occurs for realistic materials at high-visible frequencies [18]. This is counterintuitive since in the static treatment the field is totally screened by the surface charges, which had enough time to equilibrate. While it is known that an electric field can penetrate inside conductors and that it can be enhanced at the metal surface at some frequencies, here the field is strongly enhanced throughout all the conductor volume, which is the opposite of the field screening effect usually encountered in metals.

The fifth result is that using the spectral content at the sphere or slab surface we can retrieve the point charge location without knowing the charge magnitude [18]. This may form a basis for 3D near field imaging of dilute emitters, whose emission magnitude is unknown. Clearly, near field imaging has the advantage of high spatial resolution, which in combinations with detecting the object distance can be attractive for imaging small objects. The requirement for small objects arises from the fact that the field can only be retrieved from objects at a distance of the order of the slab or sphere size.

In summary, the PhD research extended the eigenpermittivity formalism to treat charge and current volume sources, which enables advantageous numerical calculations and new analytic calculations of the electric field in various two-constituent setups. Several new understandings in Veselago lens and near field imaging have been developed. A new class of current sources has been pointed out, together with implications for far-field imaging and coupling between spherical current sources, spherical layers, and spheres. Finally, it has been shown that at the center of a metal sphere there can sometimes be a very strong electric field.

# 4 References


[1] J David Jackson. *Electrodynamics*. Wiley Online Library, 1975.

[2] David J Bergman. The dielectric constant of a simple cubic array of identical spheres. *Journal of physics C: Solid state physics*, 12(22):4947, 1979.

[3] David J Bergman. Dielectric constant of a two-component granular composite: A practical scheme for calculating the pole spectrum. *Physical Review B*, 19(4):2359, 1979.

[4] David J Bergman and D Stroud. Theory of resonances in the electromagnetic scattering by macroscopic bodies. *Physical Review B*, 22(8):3527, 1980.

[5] Christophe Sauvan, Jean-Paul Hugonin, IS Maksymov, and Philippe Lalanne. Theory of the spontaneous optical emission of nanosize photonic and plasmon resonators. *Physical Review Letters*, 110(23):237401, 2013.

[6] Chandrasekhara Venkata Raman and Kariamanikkam Srinivasa Krishnan. A new type of secondary radiation. *Nature*, 121(3048):501–502, 1928.

[7] Gr Landsberg and L Mandelstam. Über die lichtzerstreuung in kristallen. *Zeitschrift für Physik A Hadrons and Nuclei*, 50(11):769–780, 1928.

[8] Michael S Eggleston, Kevin Messer, Liming Zhang, Eli Yablonovitch, and Ming C Wu. Optical antenna enhanced spontaneous emission. *Proceedings of the National Academy of Sciences*, 112(6):1704–1709, 2015.

[9] Erik J Sánchez, Lukas Novotny, and X Sunney Xie. Near-field fluorescence microscopy based on two-photon excitation with metal tips. *Physical Review Letters*, 82(20):4014, 1999.

[10] Th Förster. Zwischenmolekulare energiewanderung und fluoreszenz. *Annalen der physik*, 437(1-2):55–75, 1948.

[11] Federico García-Moliner and Fernando Flores. Introduction to the theory of solid surfaces. *Introduction to the Theory of Solid Surfaces, by Federico Garcia-Moliner, Fernando Flores, Cambridge, UK: Cambridge University Press, 2009*, 2009.

[12] Julius Adams Stratton. *Electromagnetic theory*. Mcgraw-Hill, 1941.

[13] HPJM Chew, PJ McNulty, and M Kerker. Model for raman and fluorescent scattering by molecules embedded in small particles. *Physical Review A*, 13(1):396, 1976.

[14] DF Sievenpiper, ME Sickmiller, and E Yablonovitch. 3d wire mesh photonic crystals. *Phys. Rev. Lett.*, 76(14):2480, 1996.

[15] Parry Y Chen, David J Bergman, and Yonatan Sivan. Generalizing normal mode expansion of electromagnetic green's tensor to lossy resonators in open systems. *arXiv preprint arXiv:1711.00335*, 2017.

[16] Asaf Farhi and David J Bergman. Analysis of a veselago lens in the quasistatic regime. *Phys. Rev. A*, 90:013806, 2014.

[17] Asaf Farhi and David J Bergman. Electromagnetic eigenstates and the field of an oscillating point electric dipole in a flat-slab composite structure. *Physical Review A*, 93(6):063844, 2016.

[18] Asaf Farhi and David J Bergman. Eigenstate expansion of the quasistatic electric field of a point charge in a spherical inclusion structure. *Physical Review A*, 96(4):043806, 2017.

[19] David J Bergman. Electromagnetic eigenstates of finite cylinders and their possible exploitation for calculating the macroscopic response of an array of such cylinders. In *Proc. of SPIE Vol*, volume 6641, pages 66411F–1, 2007.

[20] Andrea Alù, Mário G Silveirinha, Alessandro Salandrino, and Nader Engheta. Epsilon-near-zero metamaterials and electromagnetic sources: Tailoring the radiation phase pattern. *Physical Review B*, 75(15):155410, 2007.

[21] VG Veselago. Electrodinamics of materials both permittivity and permeability being negative. *Uspekhi Fizicheskikh Nauk (in Russian)*, 92(7):517–526, 1967.

[22] John Brian Pendry. Negative refraction makes a perfect lens. *Phys. Rev. Lett.*, 85(18):3966, 2000.

[23] Kuiru Li, Mark I Stockman, and David J Bergman. Self-similar chain of metal nanospheres as an efficient nanolens. *Physical review letters*, 91(22):227402, 2003.

[24] Asaf Farhi and David J Bergman. Generating an electromagnetic multipole by oscillating currents. *Physical Review A*, 96(2):023857, 2017.

[25] David J Bergman and Asaf Farhi. Spectral method for the static electric potential of a charge density in a composite medium. *submitted*, 2017.

[26] David J Bergman. Perfect imaging of a point charge in the quasistatic regime. *Phys. Rev. A*, 89(1):015801, 2014.

[27] Nicholas Fang, Hyesog Lee, Cheng Sun, and Xiang Zhang. Sub–diffraction-limited optical imaging with a silver superlens. *Science*, 308(5721):534–537, 2005.

[28] Parry Y Chen, David J Bergman, and Yonatan Sivan. Spectral decomposition of the lippmann-schwinger equation applied to cylinders. *arXiv preprint arXiv:1705.01747*, 2017.

# תקציר

פונקציות עצמיות של משוואות מקסוול הן שדות או פוטנציאלים שיכולים להתקיים במערכת ללא מקור. פונקציות אלו יכולות להיות מוגדרות עבור תווך הומוגני ותווך המורכב משני חומרים, שבהם הפרמטר שמאפשר את קיומן הוא הערך העצמי. החשיבות של פונקציות אלו כפולה: כאשר מתקרבים עם פרמטר פיזיקלי לערך העצמי שלהן תגובת המערכת חזקה והן יכולות לשמש לפריסה של השדה החשמלי הנוצר כתוצאה מהפעלת שדה חיצוני. ניתן להשתמש בפונקציות אלו גם בפיסיקה קלאסית וגם בפיסיקה קוונטית כאשר המקורות והאינטראקציות מטופלים באופן קוונטי.

הוצע לפני זמן רב לפרוס את השדה החשמלי בתווך המורכב משני חומרים בתגובה לשדה חיצוני בעזרת פונקציות עצמיות של משוואות מקסוול. מטרות הדוקטורט הן להכליל את הפורמליזם לטיפול במקורות חיצוניים ובהתבסס על הערכים העצמיים לנתח תופעות פיזיקליות כגון דימות ואפקט פרסל.

במהלך הדוקטורט, השדה החשמלי של מקור במערכת של לוחית בתוך תווך הומוגני נפרס בעזרת הפונקציות העצמיות של משוואות מקסוול בקירוב הקווזיסטטי ושל משוואות מקסוול המלאות. בעזרת מערכת זו נותח דימות עדשת ווסלגו. בדימות זה לעדשה השטוחה אינדקס שבירה בסימן הפוך לזה של התווך ההומוגני וניתן להגיע לרזולוציות מעבר לגבול הדיפרקציה. הוראה שמיקום הדימות האופטימלי הוא בתווך ההומוגני בצמוד לעדשה. בנוסף, השדה של מקור במערכת של כדור בתווך הומוגני נפרס בעזרת הפונקציות העצמיות של משוואות מקסוול בקירוב הקווזיסטטי. מערכת זו יכולה לשמש לניתוח תופעות פיזיקליות כגון הגברה של פליטה ספונטנית של מולקולה בסמוך לאנטנה, דימות שדה קרוב וחדירה של שדות חשמליים לתוך מוליכים. הוראה ששדה של מקור נקודתי יכול להיות מוגבר בתוך כל התווך של הכדור המוליך עבור ערכי דיאלקטריים מציאותיים למרות שנמצאים בקירוב הקווזיסטטי. לבסוף, האנלוג הכדורי של מערך מופע (phased array) הוצג בעקבות הבנת תכונות של פונקציות עצמיות בתווך הומוגני. מערך מופע כדורי יכול ליצור אור ממוקד בעל נפח קטן פי שמונה מזה המושג בעדשות קונבנציונליות ושילוב של מערכי מופע כדוריים יכול ליצור קרינה איזוטרופית.

School of Physics and Astronomy
The Raymond and Beverly Sackler
Faculty of Exact Sciences
Tel Aviv University

בית הספר לפיזיקה ולאסטרונומיה
הפקולטה למדעים מדויקים
ע"ש ריימונד ובברלי סאקלר
אוניברסיטת תל אביב

# פונקציות עצמיות של משוואות מקסוול והיישומים שלהן

## חיבור לשם קבלת התואר "דוקטור לפילוסופיה"

אסף פרחי

עבודה זו נעשתה בהדרכת
פרופ' דוד ברגמן
ופרופ' יעקב קנטור

הוגש לסנאט של אוניברסיטת תל אביב

בית הספר לפיזיקה ואסטרונומיה,
אוניברסיטת תל אביב

פברואר 2018